

The Cosmic Shoreline Revisited: A Metric for Atmospheric Retention Informed by Hydrodynamic Escape

XUAN JI(纪璇) ¹, RICHARD D CHATTERJEE ², BRANDON PARK COY ¹ AND EDWIN KITE ¹

¹*Department of the Geophysical Sciences, University of Chicago, Chicago, IL 60637 USA*

²*Department of Atmospheric, Oceanic and Planetary Physics, University of Oxford*

ABSTRACT

The “cosmic shoreline”, a semi-empirical relation that separates airless worlds from worlds with atmospheres as proposed by Zahnle & Catling (2017), is now guiding large-scale JWST surveys aimed at detecting rocky exoplanet atmospheres. We expand upon this framework by revisiting the shorelines using existing hydrodynamic escape models applied to Earth-like, Venus-like, and steam atmospheres for rocky exoplanets, and we estimate energy-limited escape rates for CH₄ atmospheres. We determine the critical instellation required for atmospheric retention by calculating time-integrated atmospheric mass loss. Our analysis introduces a new metric for target selection in the Rocky Worlds DDT and refines expectations for rocky planet atmosphere searches in Cycle 4. Exploring initial volatile inventory ranging from 0.01% to 1% of planetary mass, we find that its variation prevents the definition of a unique clear-cut shoreline, though non-linear escape physics can reduce this sensitivity to initial conditions. Additionally, uncertain distributions of high-energy stellar evolution and planet age further blur the critical instillations for atmospheric retention, yielding broad shorelines. Hydrodynamic escape models find atmospheric retention is markedly more favorable for higher-mass planets orbiting higher-mass stars, with carbon-rich atmospheres remaining plausible for 55 Cancri e despite its extreme instellation. Dedicated modeling efforts are needed to better constrain the escape dynamics of secondary atmospheres, such as the role of atomic line cooling, especially for Earth-sized planets. Finally, we illustrate how density measurements can be used to statistically test the existence of the cosmic shorelines, emphasizing the need for more precise mass and radius measurements.

(This manuscript has been submitted to ApJ and has not yet undergone peer review.)

1. INTRODUCTION

Using 500 hours of James Webb Space Telescope (JWST) time and 240 orbits of the Hubble Space Telescope (HST), the Rocky Worlds³ Director’s Discretionary Time (DDT) program (Redfield et al. 2024) aims to find atmospheres on rocky exoplanets. An essential first step is identifying the most promising targets.

1.1. The Cosmic Shoreline and Atmospheric Escape

The Rocky Worlds DDT Targets Under Consideration (TUCs)⁴ are currently organized using a priority metric based on the energy-limited “cosmic shoreline” proposed by Zahnle & Catling (2017), a semi-empirical boundary that separates Solar System bodies with atmospheres from those without. The shoreline depends on the relative cumulative XUV irradiation experienced by the body and its escape velocity. The cumulative XUV irradiation expected from planets around other stars was reconstructed using a scaling law with bolometric flux and stellar mass, following Eq. 27 in Zahnle & Catling (2017).

Stellar X-ray (< 100 Å) and EUV (100–1000 Å) photons (XUV) heat the upper atmospheres of planets, directly driving expansion out of the gravitational well to space in a hydrodynamic wind (e.g., Watson et al. 1981). Young pre-main-sequence stars emit higher XUV flux, and M dwarfs, due to their slow evolution, sustain high XUV emission over much longer timescales compared to Solar-mass stars (Preibisch & Feigelson 2005). As a result, the lower the mass of the stellar host, the greater atmospheric escape experienced at the same bolometric instellation (Tian 2015a;

³ <https://rockyworlds.stsci.edu/>

⁴ <https://outerspace.stsci.edu/pages/viewpage.action?pageId=257035126>

Tian & Ida 2015). Recently, Pass et al. (2025) revised the estimated cumulative XUV flux for mid-to-late M-dwarfs and included corrections for both the pre-main-sequence phase and energetic flaring events, which roughly triples the cumulative XUV flux compared to the canonical estimate from Zahnle & Catling (2017), placing the cosmic shoreline farther from the host star.

Apart from the physics of escape being much richer than the energy limit suggests and the variation of XUV evolution with stellar mass, the traditional “cosmic shoreline” does not account for variations that are expected in volatile content or composition. With a larger initial volatile content, an atmosphere can be retained longer at the same escape rate (Owen 2019). It is not known what controls initial volatile abundance on rocky planets. The volatiles of Solar System terrestrial bodies are thought to derive from chondritic material (e.g., Marty & Zimmermann 1999; Halliday 2013; Fischer-Gödde & Kleine 2017) through planetesimal accretion (e.g., Bond et al. 2010; Rubie et al. 2015) or pebble accretion (e.g., Johansen et al. 2023), modified by metal-silicate differentiation and by impacts at all scales (e.g., Lichtenberg et al. 2019, 2021b; Hirschmann et al. 2021; Liu et al. 2022; Malamud et al. 2024). During accretion, atmospheres are temporarily puffy and may boil off (Owen & Wu 2016). The volatiles available to build planetary atmospheres are further influenced by magma ocean degassing, atmospheric thermal loss, among other processes (e.g., Sossi 2021; Sakuraba et al. 2021; Chen & Jacobson 2022; Gu et al. 2024; Adibekyan et al. 2024; Hasegawa & Swain 2024).

These uncertainties suggest significant spread in volatile content for exoplanets. Theory suggests that rocky planets can form with substantial water inventories (Raymond et al. 2004; Kite & Schaefer 2021; Wordsworth & Kreidberg 2022). The discovery of less-dense, highly irradiated, and potentially volatile-rich small planets (e.g., Brinkman et al. 2023; Hu et al. 2024) has motivated theoretical studies of low-density lava worlds (Piette et al. 2023) and carbon-rich puffy exo-Venuses (Peng & Valencia 2024). Theory suggests worlds forming between the soot line and water ice line could be C-rich (up to 1 wt% carbon) (Bergin et al. 2015, 2023), and worlds that are water-rich should be C-rich as well (Reynard & Sotin 2023).

Realistic estimates of escape rates are crucial for locating the cosmic shoreline, and constraining it requires sophisticated modeling efforts. Stellar photons and stellar wind drive atmospheric escape processes (reviewed by Catling & Kasting 2017; Tian 2015b; Gronoff et al. 2020). A commonly used approximation is the energy-limited escape formulation (e.g. Watson et al. 1981; Lopez et al. 2012): the absorbed high-energy flux balances the work done to escape the gravitational potential of the planet, with an efficiency parameter (ϵ) accounting for uncertainties of energy-gain and loss processes. ϵ is not well constrained and varies significantly across different atmospheric compositions. For H_2 -rich atmospheres, Lopez et al. (2012) assumes $\epsilon = 0.1^{+0.1}_{-0.05}$, while Erkaev et al. (2013) uses $\epsilon = 0.15 - 0.6$ in their model. Observations of Helium outflows from Mini-Neptunes suggest typical mass loss efficiencies around $\epsilon \sim 0.2$ (Caldiroli et al. 2022; Zhang et al. 2022b,a, 2023). For Na/K-rich atmospheres, Ito & Ikoma (2021) show that $\epsilon \sim 10^{-4} - 10^{-3}$ due to strong atomic line cooling. Constraining ϵ requires comprehensive hydrodynamic modeling including heating efficiency, ionization, radiative cooling, and a wealth of other processes.

However, only a few studies have modeled secondary atmospheres loss at a high XUV flux for rocky planets. Models are generally of two forms: hydrodynamic thermospheres and transonic outflow. The former allow adiabatic expansion through a subsonic radial velocity profile but are limited to a Jeans escape formula adjusted by the bulk motion velocity as upper boundary condition at exobase (e.g. Tian et al. 2008b, 2009; Tian 2009; Nakayama et al. 2022). Hydrodynamic thermospheres are thought to correctly model the transition to a transonic wind (Tian et al. 2008a; Tian 2009) though this has not been well tested. Transonic outflow has been modelled with 1D first-principles time-stepping solutions of the hydrodynamic equations (Johnstone et al. 2019; Johnstone 2020) and with analytic approximations (Chatterjee & Pierrehumbert 2024).

Over the years, atmospheric escape models have incorporated more detailed heating and cooling processes. For CO_2 , the model used in Tian (2009) and Tian et al. (2009) includes both neutral and ion species, accounts for heating from collisions, chemical reactions, photoelectrons, and radiative line heating. For cooling, the model considers adiabatic cooling, thermal conduction, and radiative line cooling, including molecular and atomic-oxygen $63 \mu\text{m}$ cooling. The H_2O -atmosphere model used in Johnstone (2020) adds ~ 500 chemical reactions, including 56 photoreactions. However, both models consider atomic line cooling only from Lyman- α and a specific O ($63 \mu\text{m}$) line. Nakayama et al. (2022) expands upon these by including chemical reactions involving internal excitation and ionization, along with a comprehensive list of atomic line cooling processes. Their results show that, for an Earth-like N_2/O_2 atmosphere exposed to the young Sun’s radiation, atomic line cooling can suppress escape rates by around $10^4\times$ compared to

models that omit these processes (Johnstone et al. 2019). It highlights the need for more realistic reassessments of CO_2 and H_2O and CH_4 atmospheres.

Chatterjee & Pierrehumbert (2024) developed an analytical framework to describe atmospheric escape, capturing the transition from hydrostatic (Jeans) to hydrodynamic escape while considering atomic line cooling and ion-electron interactions. They find that, for hydrodynamic escape, escape rates scale linearly with XUV flux only when the flux is relatively weak and the atmosphere is weakly ionized. In contrast to earlier studies that showed a continuous increase in escape rates with increasing XUV flux (Tian 2009; Tian et al. 2009; Johnstone 2020), their model predicts that, at higher flux levels with the upper atmosphere strongly ionized, a collisional-radiative thermostat dominates. This thermostat, driven by strong atomic line cooling, limits the escape rate to a constant value, independent of further increases in XUV flux, which is shown by the results Nakayama et al. (2022). This process could enhance atmosphere retention during the saturated X-ray phase.

In summary, studies on atmospheric hydrodynamic escape of high-mean-molecular-weight atmospheres lack consensus because key physical processes—such as atomic line cooling—are often omitted, as noted in later studies. Despite these uncertainties, identifying the broad trends in atmospheric retention as a function of fundamental planetary properties—i.e., the cosmic shoreline—is increasingly urgent to help prioritize promising targets for atmosphere searches, and maximize the scientific return of observations.

Solar wind-driven escape from rocky planets (Dong et al. 2018) and impact erosion (Zahnle & Catling 2017; Sinclair et al. 2020; Krasnopolsky et al. 2004; Schlichting & Mukhopadhyay 2018; Denman et al. 2020; Wyatt et al. 2020) also play a role in shaping cosmic shoreline. Volcanic outgassing or volatile replenishment from impacts, both time-dependent, can compete with atmospheric escape (Kite et al. 2009; Kral et al. 2018; Kite & Barnett 2020).

Few studies have considered the time-integrated atmospheric loss to determine the cosmic shoreline, and they have either focused on specific targets (Ribas et al. 2016), assumed energy-limited loss (Zahnle & Catling 2017), or considered only hydrostatic “Jeans” escape (Looveren et al. 2025). Here, we calculate the atmospheric mass lost over a rocky planet’s lifespan via thermal hydrodynamic escape driven by evolving stellar XUV. By assuming an initial volatile mass available for escape and modifying this initial parameter, we determine the parameter space where a planet can retain its atmosphere and then predict the cosmic shoreline.

1.2. Statistical Test

We suggest that in addition to resource intensive JWST searches, the existence of the cosmic shoreline(s) can be tested through population-level statistical analysis of planet density. The shorelines define the distribution of bare rocky planets versus those with secondary atmospheres across parameter space. Density measurements can be used to distinguish these two populations (Luque & Pallé 2022) and then evaluate whether their distribution follows the cosmic shorelines predictions.

Similar to the radius boosting effect of H_2/He -rich atmosphere for sub-Neptunes (Lopez et al. 2012; Lopez & Fortney 2014), recent studies on Puffy Venus scenarios suggest that a sufficiently thick, high-mean-molecular-weight atmosphere on hot rocky exoplanets can inflate planetary radii, lowering density (Peng & Valencia 2024). By normalizing observed planetary densities against Earth-like composition models, planets with extended atmospheres can potentially be distinguished from bare rocky planets.

Atmospheric height increases with temperature and decreases with gravity, making radius boosting more pronounced for smaller, highly irradiated planets (Peng & Valencia 2024). Without volatile loss, normalized density is expected to decrease with increasing instellation and increase with planetary mass. However, stronger atmospheric escape on highly irradiated, low-mass planets leads to preferential atmospheric survival on larger, less-irradiated planets. Thus, analyzing whether normalized density increases or decreases with instellation and gravity provides a potential test for the existence of the cosmic shorelines.

1.3. Structure

In this study, we combine a stellar evolution model, X-ray parameterization, EUV extrapolation, and atmospheric loss rate prescriptions (Sec. 2). In Sec. 3, we present our method for estimating the cosmic shorelines. Sec. 4 presents our revised cosmic shorelines and the re-ranking of target exoplanets. We introduce the density trend test for the cosmic shorelines in Sec. 5. Finally, we discuss limitations of this work in Sec. 6.

2. MODEL

2.1. Assumptions and Initial Conditions

We adopt the mass-radius relation for Earth-like composition from Fig. 1 of Zeng et al. (2019) (Fig. C10) to determine the planetary radius (R_p). Here, R_p refers to the radius at the solid surface, excluding the atmosphere. We consider atmospheric compositions that are CO₂-dominated, CH₄-dominated, H₂O-dominated, or N₂-dominated.

The volatile inventory available for escape is defined as the total volatile content in the molten silicate and atmosphere after the planet forms. Our reasoning is as follows: accretional energy melts the silicate, distributing volatiles between the magma ocean and the atmosphere. The sequestration of volatiles into the solid mantle during the solidification of the primary magma ocean is small relative to their exsolution to the atmosphere (Elkins-Tanton 2008) (and Appendix A). For hot rocky lava worlds, as atmosphere escapes, the greenhouse effect weakens, leading to surface cooling and magma ocean freezing. This process sequesters even less volatiles into the mantle than Appendix A, since volatile concentration in the magma decreases as the atmosphere depletes. Therefore, our assumption of small sequestration and small volcanic revival is robust. Thus almost all initial volatiles are available to escape. We assume no subduction nor carbon cycle, focusing on planets too hot for surface liquid water.

For CO₂- and CH₄-dominated atmospheres, we assume an initial carbon mass and calculate the carbon loss rate. For N₂-dominated and H₂O-dominated atmospheres, we assume an initial nitrogen mass and calculate the nitrogen loss rate. H₂O is very soluble in magma and has non-negligible solubility in solid silicate (Kite & Schaefer 2021). As a result, the actual initial H₂O concentration in the bulk silicate portion of the planet is likely higher than the values presented here.

To quantify volatile loss, we prescribe atmospheric escape loss rate using hydrodynamic models. (CO₂: Tian et al. (2009); Tian (2009); N₂-dominated: Nakayama et al. (2022); Chatterjee & Pierrehumbert (2024); and H₂O: Johnstone (2020)). We consider stellar masses (M_*) ranging from 0.1 to 1 M_\odot . Starting at a certain stellar age, the total volatile losses integrated over the lifetime of the planet are compared to the initial volatile content to assess if the atmosphere is retained.

Solar wind-driven escape from rocky planets and impact erosion are not included in this initial investigation. Volatile replenishment from impacts are assumed to be small relative to the initial volatile inventory. We also assume a fixed semi-major axis throughout the planet’s lifespan and do not consider the planetary migration.

2.2. Stellar XUV evolution

All atmospheric escape mechanisms are influenced by upper atmosphere temperature. The primary source of heating in the thermospheres of planets is XUV flux. To calculate the total atmospheric loss a planet may experience, it is essential to account for the evolution of XUV flux over time. To do this, we adopt bolometric luminosity evolution models and scale the X-ray and EUV components accordingly.

2.2.1. Stellar evolution

We use the bolometric luminosity and stellar radius evolution from (Baraffe et al. 2015) (Fig. C1). We neglect this uncertainty as it is significantly smaller than the uncertainties introduced by the X-ray models and EUV extrapolation. We adopt an stellar age distribution from Berger et al. (2020), and apply an upper age cutoff that scales with stellar mass according to the stellar lifetime relation: $\tau_{max}(M_*) = 10^{10}/(M_*/M_\odot)^{2.5}$ yr. We also tested the influence stellar age distributions by combining the distribution from Swastik et al. (2023) for FGK stars and Gaidos et al. (2023) for M dwarfs. Although Gaidos et al. (2023) provides a distribution skewed toward younger stars, the resulting cosmic shorelines closely overlap with those from our default case based on Berger et al. (2020).

2.2.2. X-ray

Stellar X-ray luminosities decrease over time as magnetic braking slows stellar rotation. For young stars, stellar X-ray emission is “saturated” with a constant ratio X-ray luminosity to bolometric luminosity, L_X/L_{bol} (e.g., Vilhu 1984). After this phase, L_X/L_{bol} declines exponentially with time, following a power-law decay characterized by a decline index $L_X/L_{bol} \propto t^{-\alpha}$. To determine $L_X/L_{bol}(t)$, we use two approaches. The first method (S07) follows the results of Fig. 5 of (Selsis et al. 2007), which is based on ROSAT observations, assuming a constant $L_X/L_{bol} = 10^{-3.2}$ during saturation, followed by a power-law decline with fixed index α . The duration of the saturation phase varies as a function of stellar mass for $0.1 < M_\odot < 1$, with lower-mass stars staying saturated for longer. This method provides a simplified yet widely used prescription for estimating cumulative XUV exposure across different stellar masses. The

second (J12+G16) combines parameterizations from (Jackson et al. 2012) for stellar masses above $0.5 M_{\odot}$, based on ROSAT, Chandra, and XMM–Newton data, and from (Guinan et al. 2016) for stellar masses below $0.5 M_{\odot}$, derived from HST and Chandra observations. Notably, in J12+G16, the saturated X-ray-to-bolometric flux ratio and decline index (α) vary with stellar mass, while they remain relatively constant in S07. In our Monte Carlo simulations (Sec. 3), we randomly select between the two models with equal probability.

2.2.3. EUV

High-energy solar corona observations suggest that solar EUV emission remains relatively strong even as X-ray surface flux decreases on a timescale of hours, which suggests that EUV may decline more slowly over time compared to X-rays, though the timescale here is in Gyrs (Chadney et al. 2015; King et al. 2018; Johnstone et al. 2021). However, EUV fluxes for most stars are difficult to measure due to strong interstellar absorption in this waveband.

To estimate EUV flux based on X-ray flux, we use the scaling relation from King & Wheatley (2020) (their Eq. 3 & Fig. 2):

$$\frac{L_{EUV}}{L_{bol}} = \beta \left(\frac{L_{bol}}{A} \right)^{\gamma} \left(\frac{L_X}{L_{bol}} \right)^{\gamma+1} \quad (1)$$

where A is the stellar surface area, calculated using the stellar radius from Baraffe et al. (2015). The parameters vary for different EUV bands. King et al. (2018) provide parameters for different EUV bands, with lower bounds ranging from 51 to 124 Å and the upper bound fixed at 912 Å. King & Wheatley (2020) refines the parameters, determining that for wavelengths 100–360 Å, $\gamma_{\text{hard}} = -0.35_{-0.15}^{+0.07}$ and $\beta_{\text{hard}} = 116 \text{ (erg s}^{-1} \text{ cm}^{-2})^{\gamma_{\text{hard}}}$, while for wavelengths 360–920 Å, $\gamma_{\text{soft}} = -0.76_{-0.04}^{+0.16}$ and $\beta_{\text{soft}} = 3040 \text{ (erg s}^{-1} \text{ cm}^{-2})^{\gamma_{\text{soft}}}$, where the uncertainties cover the variations by different bands introduced in King et al. (2018). We adopt these values as input (Fig. C3).

Models uncertainties include: (1) different X-ray models, (2) uncertain EUV extrapolation parameters.

2.3. Atmospheric Escape Rate

Several studies modeled the transition to hydrodynamic escape for high mean-molecular-weight atmospheres. In this study, we adopt atmospheric loss rates as a function of XUV flux for atmospheres with different compositions from previous studies (CO₂: Tian et al. (2009); Tian (2009); N₂-dominated: Nakayama et al. (2022); Chatterjee & Pierrehumbert (2024); and H₂O: Johnstone (2020)).

2.3.1. CO₂

For a CO₂-dominated atmosphere, we obtain escape rates (kg/s) from Fig. 6 of Tian (2009) by converting the escape flux per unit surface area (kg/s/m²) (at the solid surface with radius of R_p) into the total atmospheric loss rate. We also extract escape rates from Fig. 4 of Tian et al. (2009), converting the time axis into XUV flux using their assumption that $F_{XUV} = 29.7 \cdot t^{-1.23} \text{ erg cm}^{-2} \text{ s}^{-1}$, where t is the stellar age in billions of years. We then interpolate the data to obtain a continuous function for the escape rate as a function of XUV flux. Beyond the XUV flux limits ($F_{XUV} \gtrsim 1000 \times \text{Present-Day Earth Value}$), we extrapolate the loss rates linearly on a logarithmic scale of F_{XUV} . Tian et al. (2009) provides output for a Mars-sized planet, while Tian (2009) presents results for planets with $5.9 \times$, $7.5 \times$, and $10 \times$ Earth masses, and there is no experiment conducted for Earth-sized planets. Consequently, the atmospheric escape rate for an Earth-sized planet is highly sensitive to the interpolation approach used. We illustrate various approaches in Fig. C4 and adopt the maximum and minimum values for a given XUV flux as the uncertainty range.

2.3.2. H₂O

For steam (H₂O) atmospheres, we use the results from Johnstone (2020)’s Kompot Code. We interpolate the escape rate as a function of $F_X + F_{EUV}$, using data from their Table 1. Notably, their F_{EUV}/F_X ratio is $10 \times$ higher than ours (Fig. C3). If we instead interpolate the escape rate using X-ray flux alone, the resulting escape flux would increase by a factor of 3. However, we also acknowledge that a subsequent study by the same author, Johnstone et al. (2021), reports a F_{EUV}/F_X ratio more consistent with our adopted scaling law (Fig. C3).

2.3.3. N₂

For an N₂-dominated atmosphere, we consider two studies with differing conclusions. We firstly consider the results from Nakayama et al. (2022) (Hereafter N2022, 79.58% N₂, 20.40% O₂, 0.02% CO₂, and 6×10^{-6} H₂O as lower boundary

condition). We convert the erosion timescale from their Fig. 8 into flux by dividing the mass of a 1-bar atmosphere by the timescale. Nakayama et al. (2022) find that an N_2 -dominated atmosphere is protected by atomic line cooling up to $> 1000\times$ Present-Day Earth’s F_{XUV} . Their model includes the process in Johnstone et al. (2018), and a more comprehensive treatment of atomic line cooling from nitrogen (N) and oxygen (O) (ionized and neutral). They only explore the Jeans escape as their results show the atomic line cooling is strong enough to prohibit the onset of hydrodynamic escape.

We also use results from Chatterjee & Pierrehumbert (2024) (hereafter CP2024) to determine the escape rate for an N_2 -dominated atmosphere across various planet masses, considering atomic line cooling from nitrogen. In their simulations, oxygen cooling is considered for Mars and Earth-sized planets but not for super-Earths. CP2024 considers a threshold in XUV flux to drive transonic outflow onset in collisionality for Mars-to-Earth sized planets (when advective cooling dominates) and an onset for Super-Earths based on the collisional radiative thermostat (when line cooling dominates).

In CP2024, the escape rate as a function of XUV flux is divided into three regimes: 1. Weak XUV flux: escape is negligible; 2. Intermediate XUV flux: the escape rate per unit surface area is energy-limited and increases proportionally with XUV flux (energy-limited regime, hereafter); 3. High XUV flux: due to the “thermostat” effect of strong atomic line cooling and the restricted penetration of XUV radiation, the escape rate are assumed to be approximated as reaching a maximum value independent of further XUV increases. We refer to this regime as “high-XUV plateau” hereafter. In summary, our implementation of CP2024 will serve to illustrate the result of energy-limited behavior restricted to a range of XUV fluxes. The inclusion of a threshold and plateau for hydrodynamic escape also depends on planet mass - the XUV range of energy-limited regime and the effective efficiency decreases for more massive planets with larger escape velocities (Fig. C6).

The bottom two rows of Table 1 show the range of XUV flux in which one can apply the energy-limited approximation. In this regime, the loss rate follows the scaling relation $\dot{C}/\dot{C}_* = F_{XUV}/F_{XUV,*}$. For XUV fluxes exceeding this range, the loss rate remains constant at its highest value within this regime. For fluxes below the energy-limited regime, we arbitrarily set the loss rate per surface area to a very low value of 10^{-17} kg/s/m². To generalize the loss rate for any planetary mass, we perform a 2D interpolation for the energy-limited escape rate per surface area. Additionally, we use lower and upper limits to estimate the escape rate, as listed in the bottom two rows of Table 1, and vary the rate randomly within this range in our simulations (see Fig. C7).

$M_{p,*} (M_{\oplus})$	0.11	1.00	1.76	5.90
$F_{xuv,*} (F_{xuv,\oplus})$	50	400	1000	2000
Loss Rate, \dot{C}_* (kg/s)	3×10^5	10^6	2.2×10^5	3.4×10^5
Loss Rate per Surface Area (kg/m ² /s)	2.3×10^{-9}	2.0×10^{-9}	3.1×10^{-10}	2.6×10^{-10}
Energy Limited Range of $F_{xuv} (F_{xuv,\oplus})$	5 – 500	126.5 – 1264.9	501.2 – 1995.2	1954.5 – 2046.6
	5 – 5000	126.5 – 12649.1	501.2 – 19952.6	1954.5 – 20465.8

Table 1. Adjusted escape rates from Chatterjee & Pierrehumbert (2024) for constraining an approximately energy limited regime of an N_2 -dominated atmosphere. Atmospheric escape rate as a function of XUV flux follows three regimes: negligible at low flux, energy-limited and proportional at intermediate flux (energy limited regime), and plateau at high flux due to atomic cooling. $F_{xuv,*}$ (in units of Earth’s present-day XUV flux, $F_{xuv,\oplus}$) and \dot{C}_* represent a reference point within the energy-limited regime. For F_{xuv} within the energy limited regime, the escape rate scales linearly: $\dot{C} = \dot{C}_* \cdot (F_{xuv}/F_{xuv,*})$. The last two rows indicate the upper and lower limits of where the energy-limited regime transitions to the saturation regime, which corresponds to an uncertainty of a factor of 10.

2.3.4. CH_4 atmospheres

We also consider pure CH_4 atmospheres. In the absence of detailed hydrodynamic escape modeling specifically for CH_4 , we use an energy-limited loss rate estimation (e.g. Watson et al. 1981; Lopez et al. 2012)

$$\dot{C}_{CH_4} = \epsilon \frac{\pi F_{XUV} R_p^3}{GM_p} \quad (2)$$

where G is the gravitational constant, and M_p and R_p are the planetary mass and radius. The efficiency ϵ , which measures the cooling effect and other uncertain factors, is not well constrained as discussed in Sec. 1. Here, we adopt

Table 2. Model input parameters used for the Monte Carlo simulations.

Parameter	Distribution / Choices	Description
S/S_0	$10^{\mathcal{U}(-2,5)}$	Bolometric instellation scaled to Earth's value.
τ_*	Histogram from Fig.1 in Berger et al. (2020)	Stellar age distribution.
τ_0	$10^{\mathcal{U}(6,8)}$ yr	Planet formation time ^a .
<code>xray_model</code>	{"Selsis", "Jackson"}	Choice of X-ray flux evolution model (Sec. 2.2.2).
γ_{hard}	$\mathcal{U}(-0.5, -0.28)$	Power-law index for EUV extrapolation (Eq. 1).
γ_{soft}	$\mathcal{U}(-0.8, -0.6)$	Power-law index for EUV extrapolation (Eq. 1).
<code>CO2_method</code>	{"linear", "log", "GP"}	CO ₂ escape rate interpolation method (Sec. 2.3).
ϵ	$5 \times 10^{\mathcal{U}(-2, -1)}$	Escape efficiency for energy-limited CH ₄ escape.

^a[Righter & O'Brien \(2011\)](#)

a uniform distribution for the logarithm of efficiency, $\epsilon \sim 5 \times 10^{\mathcal{U}(-2, -1)}$. For very low XUV flux, H will escape leaving C behind (e.g. Titan), but we do not model this.

The escape of CH₄ is also constrained by photodissociation driven by Lyman-alpha radiation ($\text{CH}_4 + h\nu$ (1216 Å) \rightarrow products) ([Krasnopolsky et al. 2004](#); [Wordsworth et al. 2017](#)). Using Earth's mean Lyman-alpha photon flux ($I_{\text{Ly}\alpha} = 3.7 \times 10^{11}$ photons cm⁻² s⁻¹) ([Woods et al. 1996](#)), the maximum carbon mass loss rate can be estimated as $I_{\text{Ly}\alpha} \cdot m_C \cdot \pi R_{\oplus}^2 \sim 10^4$ kg s⁻¹. This estimate is one order of magnitude higher than the energy-limited escape rate with an efficiency $\epsilon = 0.1$ and present-day Earth's XUV flux of 0.00464 W/m². Thus, as long as Lyman-alpha scales with the total XUV flux, methane photolysis does not further limit the escape rate, which remains energy-limited.

Eq. 2 assumes the XUV absorption radius $R_{\text{XUV}} = R_p$, at which the atmosphere becomes optically thick to XUV photons, following [Ito & Ikoma \(2021\)](#); [Stafne & Becker \(2024\)](#), though R_{XUV} can be computed by integrating the XUV absorption cross-section ([Murray-Clay et al. 2009](#); [Lopez et al. 2012](#); [Owen & Schlichting 2024](#); [Yoshida et al. 2022](#)). The tidal enhancement factor K_{tide} , which accounts for the reduced energy required for atmospheric escape within the planet's Roche lobe ([Erkaev et al. 2016](#)), is also not explicitly computed. For R_{XUV} smaller than twice Hill radius, $K_{\text{tide}} < 2$. In this study, the effects of varying R_{XUV} and K_{tide} are incorporated into the uncertainty range of ϵ .

2.3.5. Summary

Hydrodynamic simulations for heavy mean-molecular-weight atmospheres remain limited, preventing meaningful inter-model comparisons. This paper serves as an initial analysis to investigate how the cosmic shorelines can be determined using more realistic atmospheric escape rates derived from hydrodynamic simulations. We emphasize the need for more modeling work.

By combining the escape rate prescription with the stellar model described above, the atmospheric escape rate as a function of time for a planet orbiting a specific type of star at a given semi-major axis can be determined. Instead of providing a single value, we show a range of atmospheric escape rates for a planet with a given mass and orbital distance, incorporating all previously discussed uncertainties. The contributions of each uncertainty component are illustrated in Fig. C5, using CO₂ as an example. The key assumptions and the sources of uncertainties in the escape models are listed in Table B1.

For CO₂, CH₄, and N₂-dominated (CP2024) atmospheres, the results apply to planets with masses ranging from 0.5 to 10 M_{\oplus} . However, for H₂O, and N₂-dominated (N2022) atmospheres, hydrodynamic simulations are only available for planet with $1M_{\oplus}$.

3. STATISTICAL METHOD

Given the many uncertainties of our model assumptions (e.g., stellar XUV flux, interpolation methods, evolutionary timescales), we use a Monte Carlo approach to statistically evaluate the cosmic shorelines. Here, the cosmic shoreline is defined as the critical bolometric instellation (S_{bol}^*) below which a planet has more than a 90% probability of retaining its atmosphere, given an initial volatile inventory $M_{0,v}$. We explore how the cosmic shoreline depends on stellar mass and planetary mass, among other parameters that are harder to measure precisely (e.g., stellar age and formation time). Each uncertain parameter is drawn from an assumed probability distribution (Table 2), and for each draw, we calculate the total atmospheric loss (M_{loss}) over the planet's lifetime. For Monte Carlo simulations at fixed M_p and

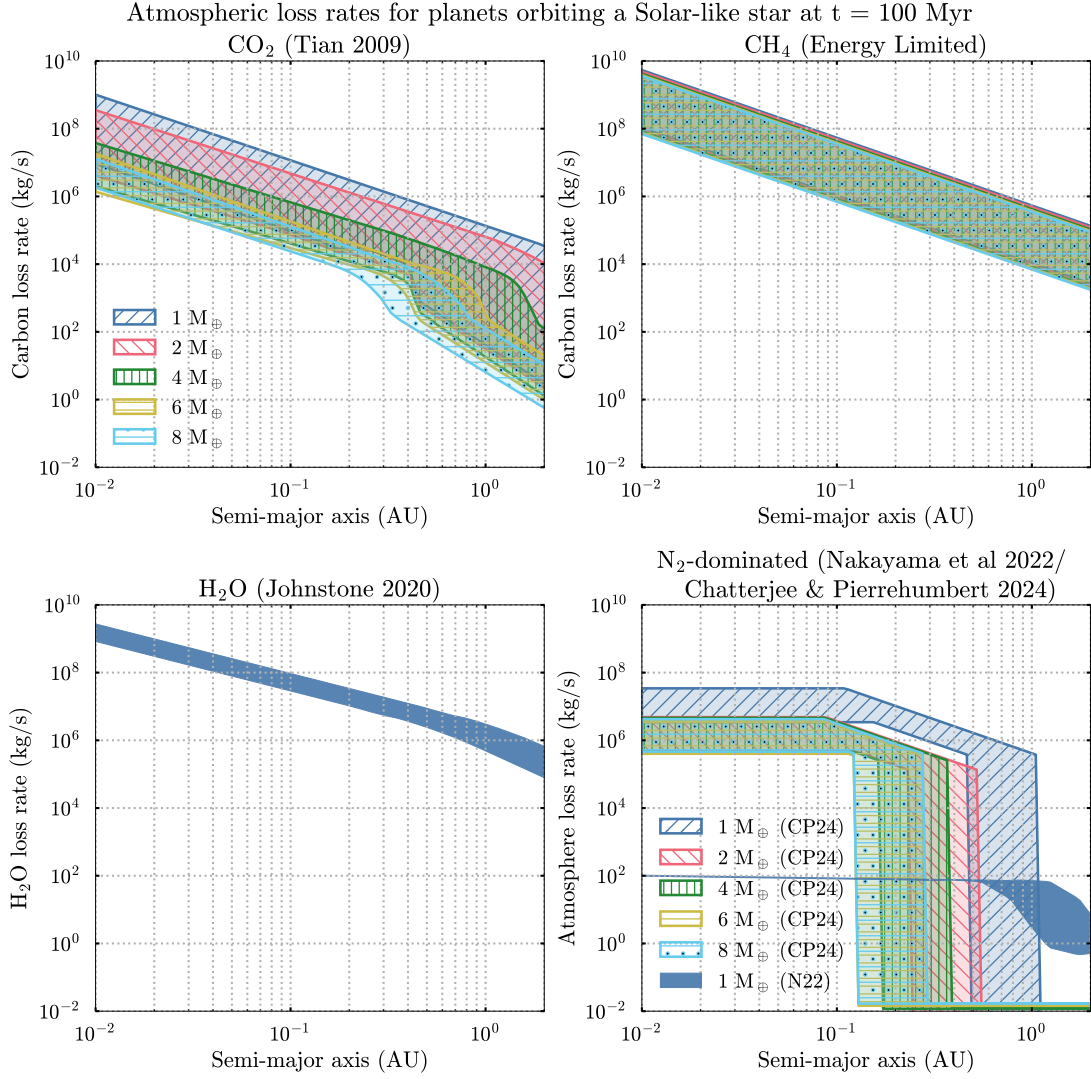


Figure 1. Atmospheric loss rates for planets orbiting a Sun-like star at $t = 100$ Myr. For CO₂-dominated, and CH₄-dominated, the escape rates for varying M_p are color-coded, as indicated in the legend. For N₂-dominated atmospheres, we use results from two different studies. CP2024 refers to the analytical framework developed by Chatterjee & Pierrehumbert (2024) which provides rates for varying M_p , while N2022 is an 1D numerical model from Nakayama et al. (2022), which only applies to Earth-mass planets. The shaded regions represent the range of atmospheric loss rates, including uncertainties in XUV flux. Additional uncertainties are included for specific atmospheres, such as CO₂ interpolation methods, the F_X/F_{EUV} ratio (H₂O atmosphere), and efficiency (ϵ) (CH₄ atmosphere) (Table 2). For CH₄ atmospheres, the loss rate weakly depends on M_p , whereas CO₂ loss is strongly mass-dependent. For N₂-dominated atmospheres, the only two studies that considers atomic line cooling, show the escape rates stay constant at higher XUV flux, but the values differ significantly: Nakayama et al. (2022) suggests that N₂-dominated atmospheres escape very slowly, whereas Chatterjee & Pierrehumbert (2024) predicts high escape rates at high XUV flux.

M_* , we conduct 10^4 trials, labeling each outcome i according to whether the planet retains its atmosphere:

$$Y_i = \begin{cases} 1, & \text{if } M_{\text{loss}} \geq M_{0,v}, \\ 0, & \text{if } M_{\text{loss}} < M_{0,v}. \end{cases} \quad (3)$$

Thus, $Y_i = 1$ indicates that the initial atmosphere is totally lost, whereas $Y_i = 0$ indicates it is retained.

We then employ logistic regression to estimate the relationship between the logarithm of bolometric instellation $\log S_i$ and the probability of losing the atmosphere. Concretely, we model

$$P(Y_i = 1 | S_i) = \frac{p_{max}}{1 + \exp(-(\alpha + \beta \log S_i))} \quad (4)$$

where α and β are parameters fit to our Monte Carlo dataset $\{(S_i, Y_i)\}$. The p_{max} is a free parameter for CP2024 N₂-dominated simulations but is forced to be 1 for other cases (see Fig. C8). With averaging $\hat{\alpha}$ and $\hat{\beta}$ are obtained, we solve for the critical instellation S_{bol}^* that yields a chosen probability p_0 of complete atmospheric loss:

$$p_0 = P(Y_i = 1 | S_{bol}^*) = \frac{p_{max}}{1 + \exp(-(\hat{\alpha} + \hat{\beta} \log S_{bol}^*))}, \quad (5)$$

which implies

$$\log S_{bol}^* = \frac{\ln\left(\frac{p_0}{p_0 - p_{max}}\right) - \hat{\alpha}}{\hat{\beta}}. \quad (6)$$

We then obtain the critical instellation (S_{bol}^*) with a given loss probability p_0 . We adopt $p_0 = 10\%$ as the central definition of the cosmic shoreline, meaning that below S_{bol}^* , there is a 90% probability that the atmosphere is retained. We also show the range corresponding to $p_0 = 50\%$ and $p_0 = 1\%$, representing 50% and 99% retention probabilities, respectively.

From our 10,000-point Monte Carlo sample for a given planetary mass and stellar mass, we then employ a bootstrap approach to obtain a robust estimate of the S_{bol}^* for a chosen probability level p_0 . Specifically, we randomly draw 5,000 data points from the original set and we refit the logistic model to this bootstrap sample to obtain parameters and compute the corresponding S_{bol}^* . We repeat it for 50 times and then average the 50 resulting S_{bol}^* values to get the final cosmic shoreline. Fig. C8 illustrates example logistic fits. By repeating this procedure for various stellar and planetary masses while incorporating the uncertainties in formation time, age, and other factors, we trace out the cosmic shoreline in parameter space.

4. COSMIC SHORELINES

The cosmic shoreline in this study is defined as the critical bolometric instellation (S_{bol}^*) below which a planet is highly likely ($> 90\%$) to retain its atmosphere, given the mass of volatiles available for loss. We focus on thermal escape driven by stellar XUV flux. S_{bol}^* depends on M_* , as the cumulative XUV flux varies with stellar type, and on M_p , which affects gravitational binding energy and escape physics.

Additionally, S_{bol}^* depends on the initial volatile mass. For CO₂- and CH₄-dominated atmospheres, we assume an initial C mass ranging from $10^{-4} \times$, which is roughly carbon mass ratios in the atmosphere and silicate of Earth and Venus, to $10^{-2} \times$ planetary mass. For N₂-dominated atmospheres, we assume a fixed available N mass ranging from $10^{-4} \times$ to $10^{-2} \times$ planetary mass. which may not fully capture reality, as such atmospheres may not originate from the initial volatile partitioning during planet formation, but could be replenished later through a water loss redox pump mechanism which is time-dependent and outgassing flux-limited (Wordsworth 2016; Schaefer et al. 2016; Wordsworth et al. 2018; Kite & Schaefer 2021). To reflect this uncertainty, we use a dashed line to represent the cosmic shoreline for N₂-dominated atmospheres with a fixed initial nitrogen mass fraction. For H₂O atmospheres, we consider an initial water mass between 10^{-4} and 10^{-2} of the planetary mass. If these volatiles remain in the atmosphere, this corresponds to surface pressures of approximately 10^2 and 10^4 bar.

Note that differences in the cosmic shorelines across atmospheric compositions may partially reflect real physical processes, but they also depend strongly on model assumptions. For example, if future models for CO₂ atmospheres incorporate atomic line cooling, the corresponding shoreline would likely shift closer to the star.

4.1. Instellation vs Stellar Mass

Fig. 2 shows various cosmic shorelines for for $1 M_\oplus$ planets as a function of stellar mass. The blue lines represent an initial volatile fraction of $\sim 10^{-4} M_p$ in planetary mass. Exoplanets located below blue lines for CO₂ or CH₄ atmosphere could retain an corresponding atmosphere if they possessed Earth-like carbon inventories or more. The red line corresponds to an initial volatile fraction of 10^{-2} , a possible upper limit for volatile mass. Exoplanets lying above this red shaded region have low $< 50\%$ probability of retaining an atmosphere, even under highly volatile-rich conditions.

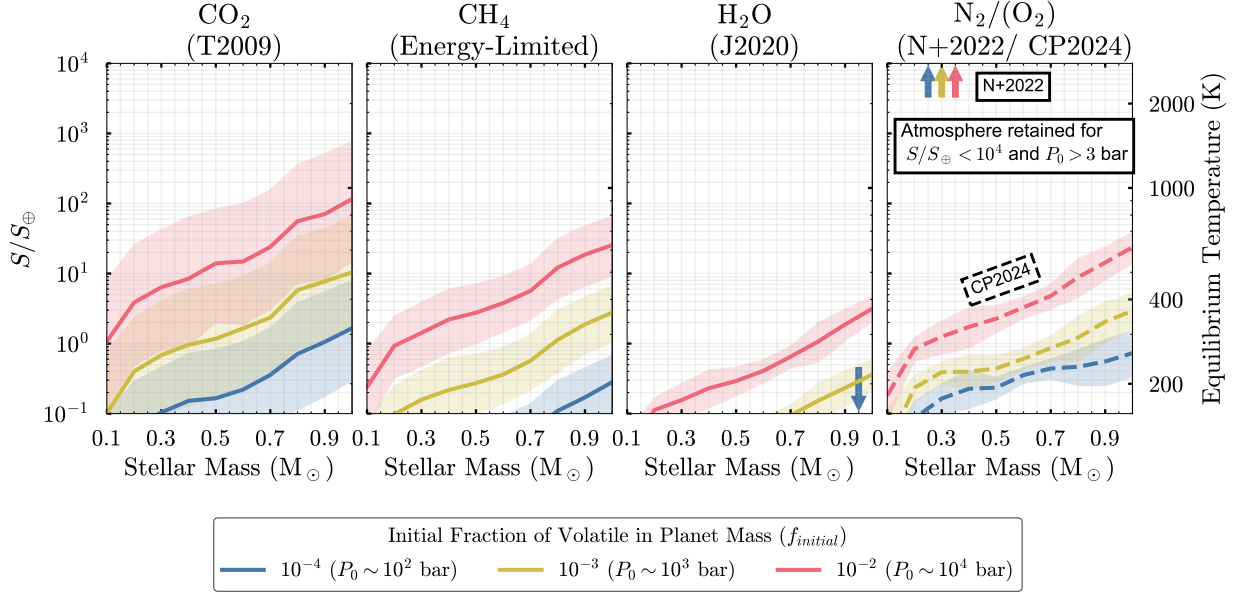


Figure 2. Cosmic shorelines for $1 M_{\oplus}$ planets depicted as the critical bolometric instellation (S_{bol}^*)—normalized to Earth’s insolation—plotted against stellar mass for various atmospheric compositions. The right y-axis also shows the corresponding equilibrium temperature (T_{eq}), assuming no albedo and perfect redistribution. Blue, yellow, and red lines correspond to initial volatile fractions of 10^{-4} , 10^{-3} , and 10^{-2} in planetary mass, respectively. The shaded regions represent a 50–99% probability range of atmospheric retention output by our model, and the solid curves represent 90% probability of atmospheric retention. For H_2O atmospheres, the blue line lies below $1 S_{\oplus}$. For an N_2 -dominated atmosphere, predictions from Nakayama et al. (2022) (N2022) suggest that all three cosmic shorelines exceed $10^4 S_{\oplus}$, indicating extreme resilience to atmospheric escape. In contrast, Chatterjee & Pierrehumbert (2024) (CP2024) predicts a less permissive cosmic shorelines.

The critical instellation is lower for lower mass stars because of their extended pre-main-sequence phase of saturated XUV emission and proportionally higher XUV fluxes for the same instellation. For the escape of CH_4 atmospheres with the energy-limited estimate, this shift reflects the greater cumulative XUV received by planets orbiting lower-mass stars, while for escaping CO_2 and N_2 -dominated atmospheres, the nonlinear dependence of escape rates on XUV flux means that not only the cumulative flux, but also the time evolution of the stellar XUV luminosity, influences cumulative atmospheric loss.

The broader shaded regions for CO_2 -dominated atmospheres compared to other cases are due mostly to the uncertain CO_2 interpolation method for CO_2 -dominated atmospheres, emphasizing the needs for future modeling for Earth-sized planets.

For H_2O atmospheres, the escape rate is around one order of magnitude higher than CH_4 at relative low XUV flux. Only for $M_* > 0.7 M_{\odot}$ can a planet at around Earth’s instellation retain its atmosphere, and only if the initial H_2O mass is 1% of the planetary mass. Note that H_2O has a non-negligible solubility in solid silicate compared to carbon, implying that even if the atmosphere is completely stripped, a substantial amount of water may still be retained in the mantle. The difference between the CH_4 and H_2O can be explained by the hydrodynamic simulations of Johnstone (2020) finding a much higher effective efficiency. However, if the line cooling effect explored in (Yoshida et al. 2022) was included, the shorelines may get closer to the star.

A higher H_2O content, for example 30% of planetary mass, (Raymond et al. 2004; Luque & Pallé 2022; Moore et al. 2024) can push the cosmic shorelines to higher instellations. However, such water-rich atmospheres may be unstable due to the boil-off effect described by Owen & Wu (2016). A more realistic shoreline should account for this instability. Our results indicate that Earth would have lost an equivalent of 200 bars of H_2O if fully evaporated, which contradicts Earth’s history. This discrepancy could be attributed to the assumption of a pure H_2O atmosphere in Johnstone (2020); in reality, the presence of a background atmosphere could enable cold trap from condensation, which could limit the escape rate and protect surface liquid water on habitable planets.

Additionally, as water escapes from water-rich worlds and the XUV flux decreases over time, O_2 may accumulate in the atmosphere (Luger & Barnes 2015; Schaefer et al. 2016; Johnstone et al. 2018; Johnstone 2020; Kite & Schaefer 2021), our shorelines did not take this into account.

For N_2 -dominated atmospheres, predictions vary significantly between reference studies. The estimates based on Nakayama et al. (2022) suggest that a planet with an initial atmospheric mass of $10^{-4}M_p$ can retain its atmosphere even at instellations of 10,000 times Earth’s insolation. In contrast, predictions derived from Chatterjee & Pierrehumbert (2024) indicate that atmospheric stripping could occur at much lower instellations (dashed curves in the lower right corner of Fig. 2). The discrepancy can be partially explained through oxygen line cooling but also the forced-hydrostatic equilibrium assumed in Nakayama et al. (2022). Resolving this discrepancy requires further work on full-set atomic line cooling and ionization effects, to provide a more reliable constraint on N_2 -dominated atmospheric escape.

The CP2024 shorelines are pinched relatively close together, especially for the late M-dwarfs, due to the non-linear behavior of the threshold XUV flux for rapid escape. For late M-dwarfs, the XUV saturation phase is long enough and the XUV decline thereafter gradual enough that only a doubling of instellation is required to evaporate 1000 bars rather than 100 bars, or 10000 bars rather than 1000 bars. So, for the two orders of magnitude range in volatile mass $10^{-4}M_p$ and $10^{-2}M_p$, the critical instellations vary by less than an order of magnitude.

4.2. Instellation vs Escape Velocity

Fig. 3 shows the cosmic shorelines for CO_2 , CH_4 , and N_2 atmospheres (using CP2024) as a function of planetary escape velocity (v_{esc}) for a variety of stellar mass ranges. We exclude H_2O atmospheres as hydrodynamic simulations for steam atmospheres do not provide results for varying M_p . The loss rates from hydrodynamic simulations are functions of M_p , and we calculate v_{esc} for each M_p assuming an Earth-like composition (Zeng et al. 2019).

The thick gray curve represents the traditional cosmic shoreline of Zahnle & Catling (2017) for reference, adopting their cumulative XUV scaling $S = F_{XUV}(L_*/L_\odot)^{0.6}$ (their Eq. 27). The red line corresponds to an initial volatile mass of $10^{-2} \times$ planetary mass as an upper limit, while the blue line represents 10^{-4} planetary mass as a lower limit.

Our results, combined with recent atmospheric detection observations, suggest that the cosmic shoreline is not a sharp dividing line but rather a transition zone—where planets shift from likely retaining atmospheres to losing them. The width of this zone is influenced by the initial volatile fraction, atmospheric composition, and potentially variations in stellar activity, which warrant further investigation in future studies (Pass et al. 2025).

The overall pattern of ratio’d density reveals that blue and green dots, representing less-dense planets, tend to cluster at the atmosphere-retaining side of cosmic shorelines compared to red and orange dots, suggesting that planets with lower scaled densities are less susceptible to atmospheric loss according to our shorelines. Further implications of this trend will be explored in detail in Sec. 5.

The cosmic shorelines moves to lower instellation for low M_* , and most Rocky Worlds DDT TUCs orbit M-dwarfs. Many of these planets fall within the red shaded region, indicating a potential to detect atmospheres around them if their initial volatile content exceeds 1 wt% of their planetary mass. In contrast, planets in the hashed zone have a probability of less than 0.5 of retaining an atmosphere, even with an initial volatile content of 1 wt%. These planets are therefore unlikely to be suitable candidates for atmospheric retention.

The cosmic shorelines for both CO_2 and CH_4 atmospheres shift inward with increasing planetary escape velocity, indicating that more massive planets are better at retaining their atmospheres against hydrodynamic escape. For CH_4 , the energy-limited escape rate is given by $\dot{C} \text{ (kg} \cdot \text{s}^{-1}) \sim F_{XUV} \cdot R_p^3/M_p$. The mass–radius relationship is approximately $M_p \sim R_p^{3.7}$ (Zeng et al. 2019). It leads to $\dot{C} \text{ (kg} \cdot \text{s}^{-1}) \sim F_{XUV} \cdot R_p^{-0.7}$, which varies by at most a factor of two across the rocky planet ranging $0.5R_\oplus \lesssim R_p \lesssim 1.6R_\oplus$. Therefore, the increase in the critical instellation for more massive planets is primarily due to their larger volatile reservoirs, as we assume a fixed initial volatile mass fraction: ($C_{total} = f_{initial} \cdot M_p \sim R_p^{3.7}$). In contrast, for CO_2 , the critical instellation rises a lot for more massive planets. This stronger gravity requires higher upper-atmosphere temperatures for efficient thermal escape to occur, which continues until adiabatic cooling effects become dominant and suppress further escape.

The slope of the cosmic shorelines determined using energy-limited estimates for CH_4 closely resembles the traditional cosmic shoreline of Zahnle & Catling (2017). However, the shoreline derived from hydrodynamic simulations for CO_2 atmospheres shifts closer to the star for more massive planets, becoming generally more favorable for atmosphere retention at all stellar masses.

The shape of the cosmic shorelines for N_2 -dominated atmospheres varies wildly with initial volatile content. When the initial nitrogen and oxygen mass is $\leq 10^{-3}M_p$, the shape of the cosmic shorelines largely follows the traditional

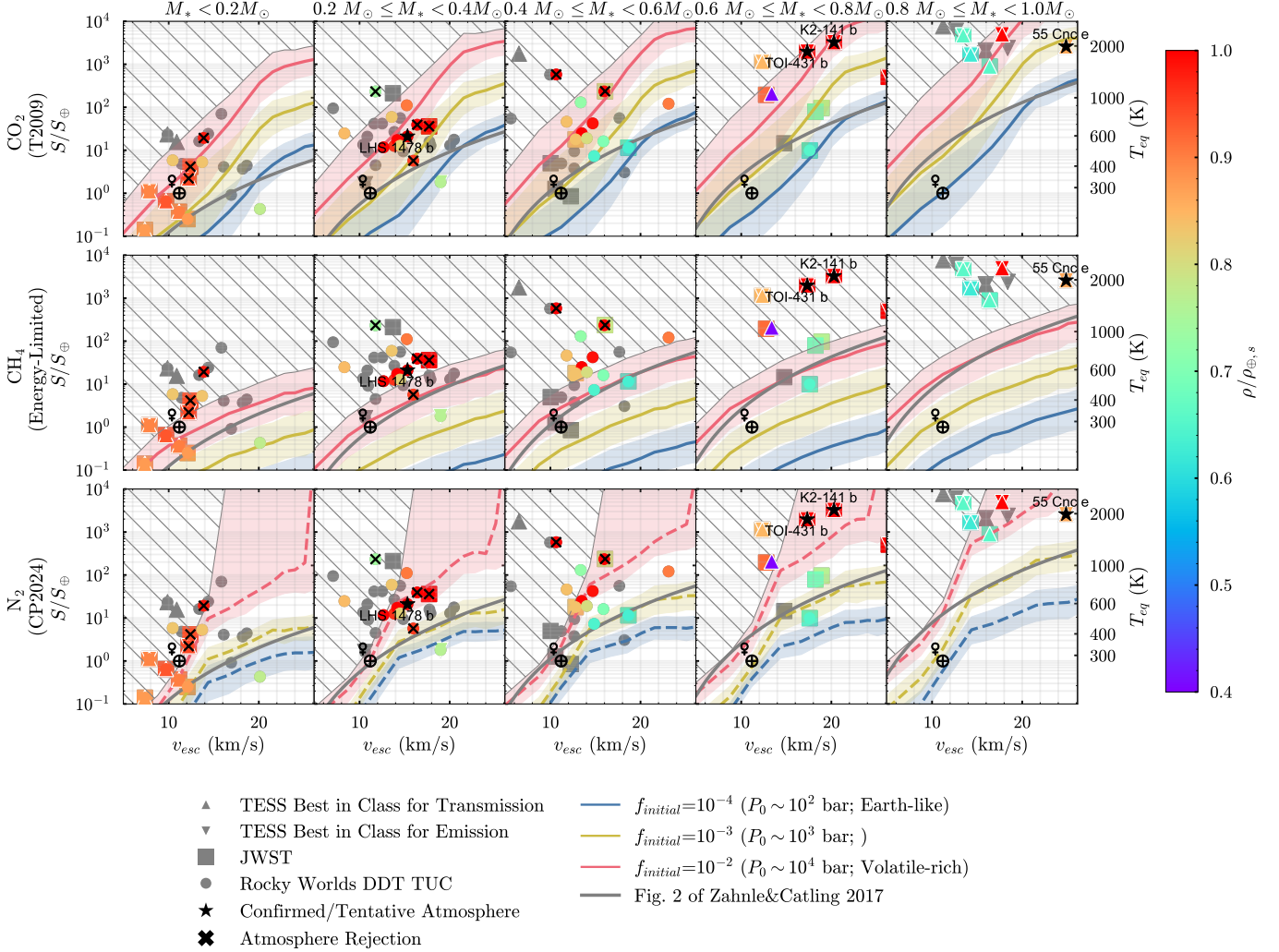


Figure 3. Cosmic shorelines displayed as the critical bolometric instellation (S_{bol}^*)—normalized to Earth’s insolation—versus planetary escape velocity. The right y-axis also shows the corresponding equilibrium temperature (T_{eq}), assuming zero albedo and full heat redistribution. The top row shows results for CO_2 -dominated atmospheres, the middle row shows CH_4 -dominated atmosphere, and the bottom row shows N_2 -dominated atmosphere. Each column corresponds to a specific range of host stellar masses. Blue, yellow and red lines indicate a 90% probability of atmosphere retention with initial volatile fractions of 10^{-4} , 10^{-3} and 10^{-2} of the planetary mass, respectively. The shaded regions in blue, yellow and red represent a 50–99% probability of atmosphere retention. The hatched region above the 50% red line represents conditions where planets are unlikely to retain an atmospheres even if volatile-rich. For comparison, the thick gray line represents the cosmic shoreline defined by XUV flux from Fig. 2 of Zahnle & Catling (2017), converted into bolometric flux using the relation $S = F_{\text{XUV}}(L_*/L_\odot)^{0.6}$ (their Eq. 27). Venus (♀), Earth (♂) are plotted for reference. The symbols mark exoplanet targets from four different samples (Sec. 4.3.1). For planets with both radius and mass measurements, the density—scaled to that of a planet with Earth-like composition ($\rho_{\oplus,s}(R_p)$)—is color-coded. Lower densities may suggest thicker atmospheres or higher volatile content. Planets with confirmed (55 Cnc e) and tentative (TOI-431 b, LHS 1478 b) atmosphere detections are labeled. Crosses denote planets with thick atmosphere ruled out: TRAPPIST-1 c, b, GJ 1132 b, GJ 1252 b, LTT 1445 A b, GJ 486 b, TOI-1468 b, GJ 367 b and TOI-1685 b (left to right). See Table 3 and Sec. 4.3.2 for planet-by-planet details.

energy-limited estimate; however, the slope differs between super-Earths and Earth-sized planets due to varying role of line cooling. For the volatile-rich case with $f_{\text{initial}} = 10^{-2}$, the 50%-probability upper boundary initially follows the energy-limited curvature but rises steeply beyond a certain planetary mass. This behavior reflects the plateau regime, where the escape rate becomes independent of XUV flux (see Sec. 2.3.3 and Fig. 4). Since our sample spans a broad range of stellar ages, planets at the same orbital distance may either retain or lose their atmospheres depending on how long atmospheric loss has been occurring (see Fig. C8). For more massive planets with larger initial volatile

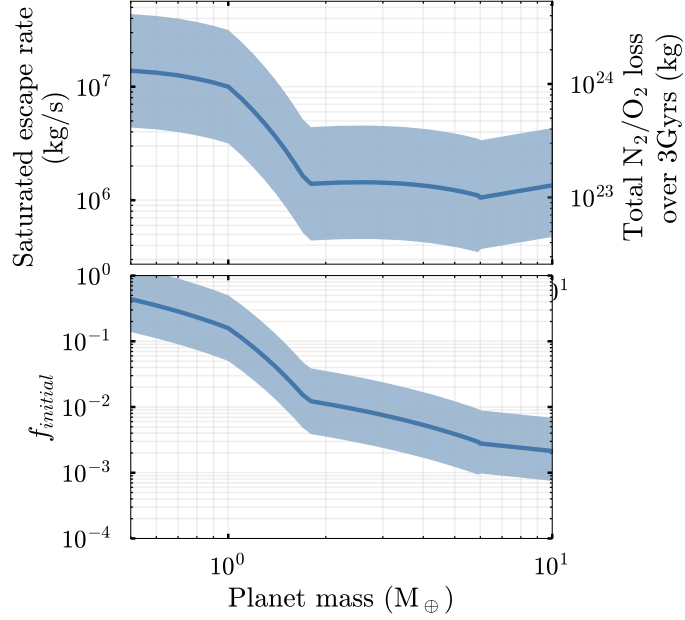


Figure 4. Upper Panel: Escape rate at high-XUV plateau of N_2 -dominated atmospheres as a function of planetary mass, based on Chatterjee & Pierrehumbert (2024). The right y-axis represents the total atmospheric loss over 3 Gyrs, which also defines the critical initial volatile content required for atmospheric retention over this timescale—planets with an initial volatile mass above this threshold can retain their atmosphere regardless of past XUV flux intensity. Lower panel: The critical initial volatile fraction (relative to planetary mass) (f_{initial}^*) sufficient to sustain an atmosphere over 3 Gyrs, independent of historical XUV flux intensity, shown as a function of planetary mass. The shaded region represents uncertainty in the critical flux at which the escape rate plateaus (see Table 1).

inventories, the probability of retention exceeds 50% regardless of XUV flux, i.e. the instellation or orbital distance. For low-mass stars with prolonged X-ray saturation phases, atmospheric loss is more dependent on stellar age. In contrast, for more massive stars with shorter saturation phases, the total loss is less strongly age-dependent, reducing uncertainties.

The high-XUV plateau explored in this study, motivated by the collisional-radiative thermostat from Chatterjee & Pierrehumbert (2024), can limit the total atmospheric loss, regardless of the historical XUV exposure. The maximum atmospheric loss can be estimated by multiplying the plateaued escape rate by the planet’s age. In Fig. 4, we show the atmospheric escape rate at plateau and the maximum atmospheric loss over 3 Gyrs (upper panel) along with the corresponding critical initial volatile fraction (f_{initial}) (lower panel), which represents the minimum volatile inventory required to make atmospheric retention over this timescale independent of historical XUV flux. As shown in Fig. 4, for planets with $M_p > 1.5M_{\oplus}$, $f_{\text{initial},*} < 10^{-2}$, confirming that the upper-limit case can always retain its atmosphere, even at extremely close orbital distances.

4.3. Best Planets for Atmospheric Retention

4.3.1. Rocky Planets Sample

We select rocky planets from the confirmed exoplanet catalog on the NASA Exoplanet Archive (NASA Exoplanet Archive 2019), using the following criteria: (1) for planets orbiting FGK stars ($M_* \geq 0.6M_{\odot}$), we select those with radii below the radius gap, defined by $\log_{10}(R_p/R_{\oplus}) = 0.11 \log_{10}(P/\text{days}) + 0.37$ (Eq. 4 of Ho & Van Eylen (2023)); (2) for M dwarfs, we include planets with scaled densities greater than 0.6 (measured density divided by the theoretical density assuming an Earth-like composition) following Luque & Pallé (2022). For those without mass measurements, we include planets with $R_p < 1.6R_{\oplus}$ a possible dividing line between ‘rocky’ and volatile-rich worlds (Rogers 2015; Cloutier & Menou 2020; Parviainen et al. 2023).

Planetary parameters were obtained via the NASA Exoplanet Archive processed using the NASA ExoArchive Aggregator⁵. We checked for and removed mass values for planets that only have maximum or minimum reported masses.

For planets without mass data and $R_p < 1.6R_\oplus$, properties were estimated assuming an Earth-like composition using the mass-radius relation from Zeng et al. (2019). For planets with both radius and mass measurements, densities were calculated and scaled relative to an Earth-like composition at the same radius, defined as ratio'd density ($\rho_{\oplus,s}(R_p)$). A low density may indicate a thick atmosphere, higher volatile content, or measurement uncertainty.

In Figure. 3, we compare our newly-derived cosmic shorelines to potentially rocky planets from three sources: a subset of TESS Best in Class for transmission and emission spectroscopy with JWST, as updated by Tom Evans-Soma (private communication) (Kempton et al. 2018; Hord et al. 2024), selected JWST targets⁶, and JWST Rocky Worlds DDT Targets Under Consideration⁷.

4.3.2. Updated Priority Metric and Targets

The initial priority metric for Rocky Worlds DDT TUCs was calculated from the tangential distance between the star and the traditional cosmic shoreline. Given the changing curvature of our cosmic shorelines, we propose refining the priority metric to measure the vertical distance—specifically, the difference in the base-10 logarithm of instellation between the planet and the cosmic shorelines for a 1 wt% volatile mass fraction at a given planetary mass. Although Fig. 3 shows only five panels corresponding to different stellar mass bins, we computed shorelines for stellar masses ranging from $0.1 M_\odot$ to $1 M_\odot$ in increments of $0.01 M_\odot$, which is roughly the highest level of precision for reported stellar masses (see Fig. C9). A priority score of zero implies that the planet is 90% likely to retain a CO₂-dominated atmosphere in our model framework assuming an initial volatile content of 1% M_p . While this is likely an over-optimistic assumption for most rocky planets, changing the initial volatile content leads to relatively similar ordering in priority score. The updated priority scores are presented in Table 3, where the first three columns list scores separately for CO₂, CH₄, and N₂ atmospheres, sorted by CO₂ priority score. Here, we focus on planets with CO₂ priority scores greater than zero whereas those less than zero are included in Appendix Table B1.

Several of these planets have low ratio'd densities that suggest highly-extended atmospheres or volatile-rich layers and thus may not be considered ‘rocky’ in the traditional Solar System sense and comprise much of the sample most likely to retain atmospheres (e.g., LHS 1140 b, TOI 1452 b, TOI-776 b, TOI-260 b). Therefore, we highlight planets with high observability metrics that are likely “rocky”—those with a radius below $1.6 R_\oplus$ and a normalized density above $0.8 \rho_{\oplus,s}$ —that have a CO₂ priority metric greater than zero. We consider planets with an emission spectroscopy metric (ESM, Kempton et al. 2018) above that of TRAPPIST-1 c (ESM=1.7, amenable to atmospheric reconnaissance with MIRI F1500W) or a transmission spectroscopy metric (TSM) greater than 10 (the threshold for atmospheric characterization suggested by Kempton et al. 2018). This list includes, in order of decreasing CO₂ priority score: TOI-4559 b, TOI-711 b, LTT 1445 A b, TOI-1693 b, TRAPPIST-1 g, TOI-1468 b, TRAPPIST-1 f, GJ 486 b, LHS 1140 c, LHS 1478 b, Gliese 12 b, GJ 3929 b, K2-141 b, TRAPPIST-1 h, HD 260655 b, LHS 1815 b, TRAPPIST-1 e, LTT 1445 A c, and TRAPPIST-1 c. Several of these planets have been observed in emission, suggesting a lack of thick atmospheres [LTT 1445 A b (Wachiraphan et al. 2024), TOI-1468 b (Valdés et al. 2025), GJ 486 b (Mansfield et al. 2024), and TRAPPIST-1 c (Zieba et al. 2023)]. Thus, if rocky planets generally form with similar volatile inventories, which is uncertain, we can consider LTT 1445 A b as a loose lower bound of where rocky planet atmospheres might be retained. Indeed, LTT 1445 A b's CO₂ priority score drops to 0.0 given a more conservative initial volatile fraction of 0.1wt%. TOI-4559 b and TOI-771 b stand out as potentially rocky planets with high observability metrics above this threshold. In particular, TOI-4559 b orbits an earlier-type M dwarf (\sim M2V) and may not be subject to the extended pre-main sequence mass loss for planets around mid-to-late M dwarfs proposed by Pass et al. (2025). However, both planets currently lack published mass values and thus it is uncertain whether they are truly ‘rocky’, highlighting the need for radial velocity characterization.

While several additional potentially ‘rocky’ planets exist above this threshold, including TOI-198 b, TOI-1680 b, TOI-237 b, LP 890-9 c, TOI-700 d, and Kepler-167 d, their low observability metrics means that atmospheric detection while likely take a very large time investment with JWST. For example, LP 980-9 c will be observed over 18 transits in Cycle 4 (PID: 7073, PIs: Lustig-Yaeger and Stevenson). In addition, some of these planets’ temperate equilibrium temperatures mean that thin (\lesssim 1 bar) atmospheres may be subject to atmospheric collapse if they are tidally locked (Wordsworth 2015). Whether these planets are, in fact, tidally locked is unknown, but planets around low-mass stars experience much higher tidal forces that promote efficient tidal locking (e.g., Barnes 2017).

⁵ <https://github.com/lkreidberg/TSM>

⁶ <https://www.stsci.edu/~nnikolov/TrExoLiSTS/JWST/trexolists.html>

⁷ <https://outerspace.stsci.edu/pages/viewpage.action?pageId=257035126>

Given that the vast majority of our planet sample falls below LTT 1445 A b in priority score, it is likely that many rocky planets that will be observed in JWST Cycles 1-4 will be bona fide ‘bare rocks’ lacking thick atmospheres. However, bare rock observations remain useful in constraining the escape environments of different star types while providing population-level upper bounds on volatile inventories for rocky planets. In addition, eclipse observations are particularly powerful for providing useful geological information for planets without atmospheres (e.g., Coy et al. 2024; Paragas et al. 2025).

Table 3. Atmospheric Retention Targets Ranked by Priority Metric for CO₂-Dominated Atmospheres

Planet	Priority Metric			R_p (R_\oplus)	M_p (M_\oplus)	v_{esc} (km/s)	ρ^8 ($\rho_{\oplus,s}$)	M_* (M_\odot)	T_{eq} (K)	K -mag	$(R_p/R_s)^2$ (ppm)	ESM	TSM
	[CO ₂]	[CH ₄]	[N ₂]										
LHS 1140 b	3.13	1.14	2.30	1.73	5.60	20.1	0.77	0.18	225	8.8	5397	0.1	67
TOI-1452 b	2.38	0.59	1.63	1.67	4.82	19.0	0.77	0.25	322	9.7	3107	0.6	39
TOI-198 b	2.33	0.65	1.74	1.44	3.82 [†]	18.2 [†]	1 [†]	0.47	368	7.9	896	0.6	5 [†]
TOI-776 b	1.89	0.15	1.31	1.80	5.00	18.7	0.63	0.54	512	7.6	908	2.7	50
TOI-260 b	1.79	0.26	1.35	1.71	4.23	17.6	0.65	0.62	493	6.6	667	2.6	67
TOI-1680 b	1.73	0.00	1.00	1.47	4.08 [†]	18.7 [†]	1 [†]	0.18	403	10.8	4073	1.3	6 [†]
TOI-237 b	1.69	0.04	1.01	1.44	3.82 [†]	18.2 [†]	1 [†]	0.18	386	10.9	3915	1.0	6 [†]
LP 890-9 c	1.67	0.27	1.22	1.37	3.13 [†]	16.9 [†]	1 [†]	0.12	271	11.3	6487	0.2	6 [†]
TOI-1634 b	1.59	-0.64	0.90	1.77	7.57	23.1	0.90	0.45	922	8.6	1305	14.0	54
TOI-4559 b	1.36	-0.24	0.81	1.42	3.56 [†]	17.7 [†]	1 [†]	0.39	554	8.6	1203	3.1	8 [†]
TOI-1075 b	1.34	-0.89	1.15	1.79	9.95	26.4	1.06	0.60	1321	9.1	799	12.0	29
TOI-700 d	1.33	0.57	0.81	1.07	1.29 [†]	12.3 [†]	1 [†]	0.41	267	8.6	546	<0.1	3 [†]
Kepler-167 d	1.28	0.22	1.46	1.24	2.16 [†]	14.8 [†]	1 [†]	0.78	542	11.8	230	0.1	1 [†]
55 Cnc e	1.25	-0.97	0.96	1.86	9.38	25.1	0.92	0.91	1958	4.0	326	67.7	211
TOI-178 c	1.20	-0.62	0.61	1.67	4.77	18.9	0.76	0.65	873	8.7	552	3.9	34
TOI-771 b	1.18	-0.42	0.58	1.42	3.63 [†]	17.9 [†]	1 [†]	0.22	526	9.7	2902	4.5	11[†]
TOI-836 b	1.15	-0.52	0.62	1.70	4.53	18.2	0.69	0.68	828	6.8	552	7.5	79
WASP-47 e	1.13	-1.11	0.66	1.83	9.00	24.8	0.93	1.06	2325	10.2	211	3.1	11
LTT 1445 A b*	1.08	-0.15	0.77	1.34	2.73	16.0	0.95	0.26	430	6.5	2055	6.0	34
TOI-244 b	0.99	-0.08	0.85	1.52	2.68	14.9	0.64	0.43	457	8.0	1070	2.0	71
TOI-1693 b	0.94	-0.62	0.48	1.41	3.51 [†]	17.7 [†]	1 [†]	0.49	764	8.3	790	6.1	8 [†]
TRAPPIST-1 g	0.93	0.14	0.35	1.13	1.32	12.1	0.88	0.09	197	10.3	7540	<0.1	15
HD 260655 c	0.91	-0.31	0.67	1.53	3.09	15.9	0.70	0.44	557	5.9	1025	8.9	196
TOI-1468 b*	0.89	-0.66	0.36	1.28	3.21	17.7	1.24	0.34	681	8.5	1164	6.1	10
TOI-700 e	0.82	0.18	-0.03	0.95	0.85 [†]	10.6 [†]	1 [†]	0.41	295	8.6	431	0.1	4 [†]
LP 890-9 b	0.78	-0.47	0.48	1.32	2.74 [†]	16.1 [†]	1 [†]	0.12	395	11.3	6049	1.6	9 [†]
K2-239 d	0.73	-0.08	0.30	1.10	1.41 [†]	12.6 [†]	1 [†]	0.40	399	10.0	785	0.3	4 [†]
TRAPPIST-1 f	0.57	-0.15	-0.25	1.04	1.04	11.2	0.90	0.09	217	10.3	6460	0.1	17
TOI-2096 b	0.54	-0.52	0.37	1.24	2.19 [†]	14.8 [†]	1 [†]	0.23	487	11.0	2352	1.4	6 [†]
GJ 486 b*	0.46	-0.84	0.07	1.29	2.77	16.4	1.09	0.31	696	6.4	1328	21.1	35
L 98-59 c	0.45	-0.54	0.37	1.34	2.25	14.5	0.82	0.31	526	7.1	1550	7.3	28
K2-129 b	0.38	-0.28	-0.21	1.04	1.15 [†]	11.8 [†]	1 [†]	0.36	405	8.9	701	0.5	7 [†]
GJ 357 b	0.38	-0.56	0.19	1.20	1.84	13.9	0.96	0.34	524	6.5	1066	6.3	28
LHS 1140 c	0.35	-0.51	0.19	1.27	1.91	13.7	0.83	0.18	422	8.8	2917	3.0	22
K2-239 b	0.33	-0.48	-0.10	1.10	1.41 [†]	12.6 [†]	1 [†]	0.40	502	10.0	785	0.8	5 [†]
LHS 1478 b	0.32	-0.79	0.11	1.24	2.33	15.3	1.05	0.24	595	8.8	2142	7.0	18

⁸ the density scaled to that of a planet with Earth-like composition

TOI-406 c	0.32	-0.63	0.25	1.32	2.08	14.0	0.80	0.41	580	8.9	871	2.5	8
K2-239 c	0.29	-0.34	-0.45	1.00	1.01 [†]	11.2 [†]	1 [†]	0.40	427	10.0	649	0.4	4 [†]
Gliese 12 b	0.27	-0.32	-0.60	0.90	0.69 [†]	9.8 [†]	1 [†]	0.24	313	7.8	941	0.3	16[†]
GJ 3929 b	0.25	-0.71	0.15	1.09	1.75	14.2	1.23	0.31	567	7.9	975	4.1	14
Kepler-1107 b	0.23	-1.50	-0.22	1.45	3.92 [†]	18.4 [†]	1 [†]	0.86	1943	12.2	291	1.4	1 [†]
K2-141 b	0.21	-1.88	-0.53	1.51	4.97	20.3	1.06	0.71	2101	8.4	413	14.9	60
TRAPPIST-1 h	0.20	-0.35	-0.82	0.76	0.33	7.4	0.88	0.09	171	10.3	3372	<0.1	16
HD 260655 b	0.18	-0.82	0.11	1.24	2.14	14.7	0.99	0.44	709	5.9	671	11.8	29
LHS 1815 b	0.17	-0.70	-0.01	1.09	1.58	13.5	1.14	0.50	617	8.0	396	1.9	7
TOI-700 b	0.13	-0.49	-0.77	0.91	0.73 [†]	10.0 [†]	1 [†]	0.41	415	8.6	396	0.4	6 [†]
TOI-270 b	0.09	-0.74	-0.31	1.21	1.58	12.8	0.83	0.40	581	8.3	847	3.2	13
TRAPPIST-1 e	0.07	-0.58	-0.92	0.92	0.69	9.7	0.93	0.09	249	10.3	5007	0.2	20
LTT 1445 A c	0.02	-0.79	-0.43	1.07	1.37	12.7	1.06	0.26	514	6.5	1310	7.6	41
TRAPPIST-1 c*	0.01	-0.79	-0.54	1.10	1.31	12.2	0.95	0.09	339	10.3	7119	1.7	25

Table 3. The scores for each atmospheric composition represent the difference in the base-10 logarithm of instellation between the planet and the cosmic shorelines for a 1 wt% volatile mass fraction at a given planetary mass. More negative values are more atmosphere-favorable. [†]These planets lack a measured mass value and we assume an Earth-like composition for these calculations. *These planets have been suggested to have no thick atmosphere based on thermal emission observations. We do not take the individual constrained stellar age into account, and the score is obtained by assuming an stellar age distribution from Berger et al. (2020).

4.3.3. Comparison to Planets with Atmospheric Detection/Rejection

Emission observations have begun to provide tentative detections for atmospheres around rocky planets, including LHS 1478 b (August et al. 2025), TOI-431 b (Monaghan et al. 2025), 55 Cnc e (Demory et al. 2016; Hu et al. 2024), and K2-141 b (Zieba et al. 2022). 3 of 4 of these planets lie beyond the temperature threshold for forming thin silicate vapor atmospheres from vapor pressure equilibrium with a dayside magma pool (e.g., Kite et al. 2016) and thus may not fall under the traditional ‘cosmic shoreline’ framework of initial atmosphere retention. However, the tentative detection of a carbon-rich atmosphere on 55 Cnc e (Hu et al. 2024) may imply that these atmospheres are not only sustained by vapor pressure equilibrium, but rather formed with a significant fraction of volatiles. We discuss these planets and several ‘bare rock’ detections in context of our shorelines below.

55 Cnc e, which likely has an atmosphere despite its very high insolation (Hu et al. 2024), lies well below the cosmic shorelines for $f_{\text{initial}} = 10^{-2}$ for CO₂ and N₂-dominated atmospheres (thick pink line of Fig. 3), while it is beyond the energy-limited estimate in the CH₄ case. TOI-431 b, another hot rocky super-Earth with low dayside emission—implying a *tentative* atmospheric detection (Monaghan et al. 2025)—falls within the upper boundary of the shaded region for $f_{\text{initial}} = 10^{-2}$ (the upper bound implies 50% chance of atmosphere retention). Notably, both planets are massive super-Earths orbiting more massive stars, and our shorelines favor atmospheric retention in such cases.

LHS 1478 b, which has a *tentatively* detected atmosphere (August et al. 2025)—suggested by a possible shallow eclipse depth—falls near the 90% cosmic shorelines for $f_{\text{initial}} = 10^{-2}$ for both CO₂ and N₂-dominated atmospheres. GJ 486 b, located near LHS 1478 b in parameter space, likely lacks a thick atmosphere (Mansfield et al. 2024). This atmosphere rejection can help constrain GJ 486 b’s initial volatile inventory: if there is a carbon-dominated oxidized environment, the total carbon mass is likely to be less than 0.01 M_p ; if it initially possessed a N₂-dominated atmosphere, its mass is likely to be below 0.01 M_p , within our model framework. GJ 1132 b, another likely bare rock (Xue et al. 2024), lies above all our shorelines but very close to the CO₂ red line, suggesting that its initial carbon fraction was less likely to be more than 0.01 M_p if carbon-dominated oxidized environment.

For the TRAPPIST-1 system, both TRAPPIST-1 b and c lie on or beyond the $f_{\text{initial}} = 10^{-2}$ boundary for all three atmospheric compositions. This means that even if these planets formed super volatile-rich that they are probably unable to retain atmospheres. Notably, their host star has an extremely low mass ($M_* = 0.089M_\odot$), at the lower edge

of the stellar mass range considered in the panel, where shorelines are derived by randomly sampling stellar masses within that range. As a result, the actual shoreline for TRAPPIST planets is even farther from the star than shown in Fig. 3. Conversely, TOI-431 b orbits a star with mass $0.78 M_{\odot}$ at the high end of the panel, meaning its more accurate shoreline would lie closer to the star than shown. To address this, we reduced the stellar mass bin size to $0.01 M_{\odot}$ when generating Table 3. We also do not account for the age dependence of the cosmic shorelines. While escape is largely dominated by the early saturated phase, TRAPPIST-1 is relatively old and lies at relative high-end tail of our stellar age distribution, meaning its planets are even more likely to have lost their atmospheres than suggested by our average predictions.

Earth and Venus straddle the $f_{\text{initial}} = 10^{-4}$ shoreline, which may suggest that they began with a slightly higher volatile inventory. A higher volatile content could also lead to significant sequestration of volatiles in the mantle, allowing for gradual outgassing over time. This prolonged supply could result in a supply-limited escape, which is not considered in this study.

5. TREND OF RATIO'D DENSITY

Since planetary mass (M_p) can be measured through radial velocity or Transit-timing variation (TTV) observations, planet density can be calculated using the measured transit radius: $\rho = M_p / (4/3\pi R_{\text{transit}}^3)$. The transit radius R_{transit} corresponds to the altitude where the atmosphere becomes sufficiently opaque in a slant viewing geometry, for $\sim (e - 1)/e$ starlight will be blocked. If opaque clouds or hazes are present, transit radius then corresponds to the altitude of the cloud tops (Lopez et al. 2012; Gao et al. 2020; Gao & Powell 2021). Because the transit radius includes the atmospheric contribution, the measured density (ρ) can be lower than the density of the solid portion of the planet alone. By comparing the observed density with theoretical density estimates for rocky planets, we can distinguish planets with substantial atmospheres from bare rocky worlds (Rogers 2015; Jontof-Hutter 2019; Luque & Pallé 2022).

As the cosmic shorelines separate bare rocky planets from those with significant atmospheres in planetary-mass-instellation space, we expect statistical trends in the observed densities of exoplanets. Specifically, density should increase with instellation and decrease with planetary mass because planets that experience weaker XUV flux and have higher gravity are more likely to retain their atmospheres and have lower densities. This trend provides a new observational test for the cosmic shorelines hypothesis.

We build a model, with several simplifying assumptions, intended to demonstrate the concept rather than provide precise predictions. For this study, we focus on CO_2 atmospheres as a representative case, given that the Mid-Infrared Instrument (MIRI) on JWST is most sensitive to CO_2 detection at $15 \mu\text{m}$, and given the importance of CO_2 for solar-system rocky planets.

5.1. Vertical Thermal Structure

To see how atmosphere boosts planetary radius, we construct a one-dimensional vertical structure model that considers the thermal structure of the atmosphere and the underlying magma ocean, if present. Using this, we estimate the transit radius of a planet with a given volatile content by accounting for radiative and convective layers of atmosphere, volatile partitioning between the atmosphere and magma, and the effect of hydrostatic equilibrium on atmospheric extent. We then derive the density ratio'd to an Earth-like composition and perform statistical analysis to investigate how the cosmic shorelines influences the trend of the ratio'd density.

We first consider a two-layer atmospheric structure, as illustrated in panel (1) of Fig. 5: 1. a radiative upper atmosphere, where the temperature is isothermal above the radiative-convective boundary (RCB), and 2. a convective lower atmosphere, where the temperature profile follows an adiabatic gradient. RCB temperature is determined by radiative equilibrium, assuming an albedo of 0.3:

$$T_{\text{RCB}} = \left(\frac{(1 - 0.3)S}{4\sigma} \right)^{1/4} \quad (7)$$

where S is the instellation, and σ is the Stefan-Boltzmann constant. This formulation assumes that heat is efficiently redistributed across the planet by a thick atmosphere, leading to a uniform temperature distribution. The RCB pressure is fixed as $p_{\text{RCB}} = 0.25\text{bar}$, which can correctly predict the surface temperature of Venus. Below the RCB, the surface temperature (T_{surf}) is obtained by integrating a dry adiabatic profile down to the surface. In the convective region, where pressure and temperature vary significantly, the heat capacity ratio (γ) is not constant but instead depends

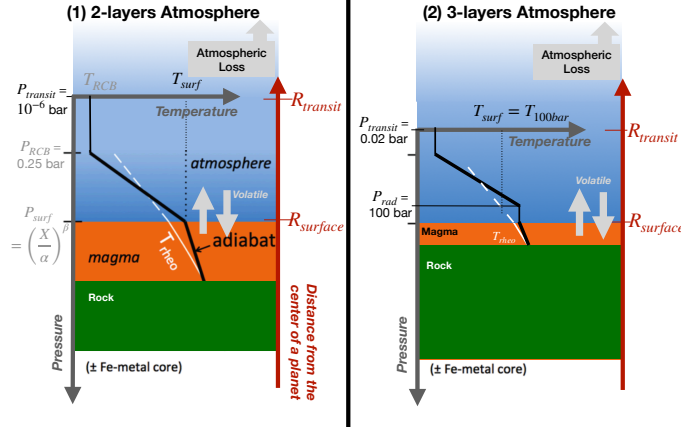


Figure 5. Planetary Thermal Structure and Two End-Member Estimates for Transit Radius. The thin black line denotes an isothermal atmosphere in the radiative layer, while the thick black line represents an adiabatic profile in the convective layer. The adiabatic index γ varies with temperature and pressure, as shown in Fig. C11. The radiative-convective boundary (RCB) temperature is set by energy balance with an albedo of 0.3: $T_{RCB} = ((1 - 0.3)S/\sigma)^{1/4}$. The surface temperature (T_{surf}) is calculated by extending the dry adiabatic profile from the RCB to the surface (a), or to the top of the radiative layer near the surface (b). The white line corresponds to the rheological transition ($\sim 40\%$ melt fraction) P-T relation for rock, with dashed white sections indicating depths where no rock is present. If $T_{surf} > T_{rheo}(P = P_{surf})$, the surface is a low-viscosity magma ocean. The intersection of the thick black line with the white line marks the depth at which magma crystallizes, defining the extent of the magma layer. Volatiles are assumed to be partitioned between the magma and atmosphere, with surface pressure governed by the solubility law as a function of the volatile concentration in the magma (X): ($P_{surf} = (X/\alpha)^\beta$), where α and β are obtained from Lichtenberg et al. (2021a). The pressure level probed during a transit ($P_{transit}$) is set to a constant value, with the corresponding altitude determined under hydrostatic balance. Gravity (g) changes with altitude in our calculation. The transit radius ($R_{transit}$), measured radius via the transit method, is the distance from this altitude to the planetary center. (1) Upper-limit estimate of atmospheric height: Assumes the entire atmosphere below the RCB is fully convective, following a dry adiabatic profile. $P_{transit} = 10^{-6}$ bar. (2) Lower-limit estimate of atmospheric height: Assumes a radiative layer extends from the surface up to $P = 100$ bar. $P_{transit} = 0.02$ bar.

on both temperature and pressure. We account for this variation by expressing γ as a function of these parameters, computed using NASA’s Chemical Equilibrium with Applications (CEA) tool⁹ (Gordon & McBride 1994), as shown in Fig. C11.

For thick CO_2 -dominated atmospheres, however, the convective zone may not extend all the way to the surface. Instead, a radiative, isothermal layer might develop near the surface due to strong absorption of stellar radiation and internal heating (Selsis et al. 2023; Peng & Valencia 2024). Since a full radiative transfer calculation is beyond the scope of this model, we adopt a simplified assumption: in the lower-limit estimate of transit radius (panel (2) of Fig. 5), we assume the convective-radiative transition in the deep atmosphere starts from 100 bar. This assumption allows us to explore the potential range of atmospheric extent while acknowledging uncertainties in radiative transfer.

The extent of a possible magma ocean is constrained by the rheological transition temperature (T_{rheo}) at a given pressure, corresponding to $\sim 40\%$ melt fraction for silicate rock (following the method of Kite & Barnett (2020), which is based on Andrault et al. (2011)). If $T_{surf} > T_{rheo}(P = P_{surf})$, the surface remains molten, and volatiles can continue to exchange between the atmosphere and magma ocean. The partitioning of volatiles is governed by a solubility law that relates surface pressure to the volatile concentration in the magma (X_{magma}):

$$P_{surf} = (X_{magma}/\alpha)^\beta \quad (8)$$

where $\alpha = 1.94 \times 10^{-3}$ and $\beta = 0.714$ are empirical parameters for CO_2 obtained from Lichtenberg et al. (2021a). We acknowledge that solubility depends on both temperature and pressure; our model considers only pressure.

⁹ <https://cearun.grc.nasa.gov/>

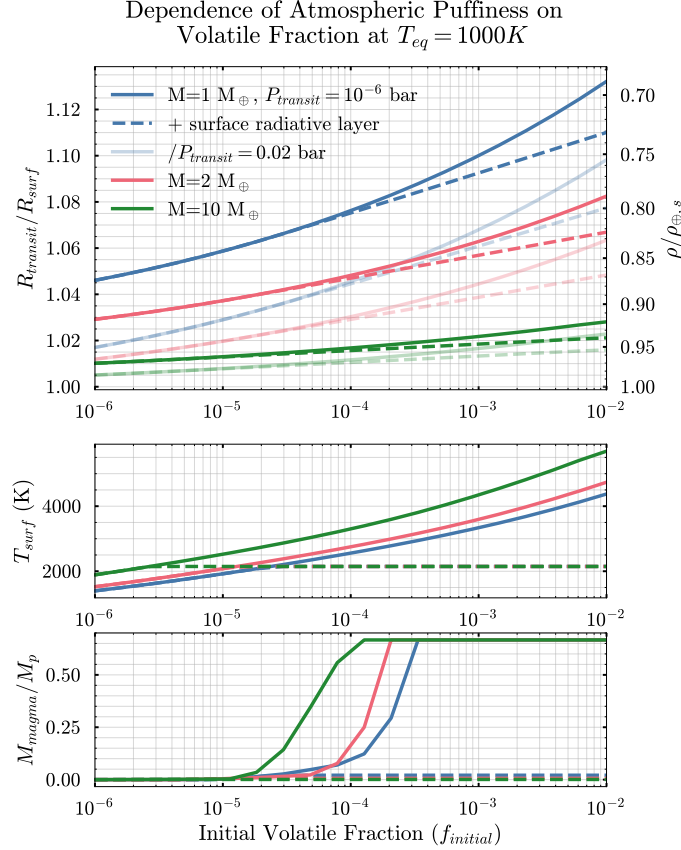


Figure 6. Atmospheric Radius Boosting effect. Top: The ratio of the transit radius to the radius of the solid surface (including the magma layer if present) as a function of the initial volatile fraction (f_{initial}). The right y-axis shows the corresponding ratio'd density. Solid lines correspond to the two-layer model (Scenario (1) in Fig. 5) with $P_{\text{transit}} = 10^{-6}$ bar, where the atmosphere consists of a convective lower layer and an isothermal upper layer beyond the radiative-convective boundary (RCB). Dashed lines represent the three-layer model (Scenario (2) in Fig. 5 but with adjusted P_{transit}), which includes an additional radiative layer near the surface. The lighter-colored lines indicate the same atmospheric conditions, but the transit radius is measured at $P_{\text{transit}} = 0.02$ bar. Middle: Surface temperature for the different atmospheric scenarios described above. At $T \gtrsim 10^4$ K, the silicate and Fe will expand (Lock & Stewart 2017), which is not considered in our model. Bottom: Magma ocean mass fraction for different atmospheric structures. The layered structure of the atmosphere influences the transit radius only when f_{initial} is sufficiently high for the surface pressure to exceed 100 bar. The choice of P_{transit} has a much greater impact on the derived transit radius than the atmospheric structure alone.

To link this atmospheric model to transit observations, we assume P_{transit} as a constant value obtained from previous studies. The altitude at this level is derived by assuming hydrostatic balance. Two end-member scenarios are considered for estimating the atmospheric height:

1. Upper-limit estimate: The atmosphere below the RCB is assumed to be fully convective, following a dry adiabatic profile. The transit pressure is set to $P_{\text{transit}} = 10^{-6}$ bar, which is set by cloud top (Gao et al. 2020).
2. Lower-limit estimate: A radiative layer is assumed to develop near the surface, limiting atmospheric expansion. The transit pressure is set to $P_{\text{transit}} = 0.02$ bar (Lopez et al. 2012), obtained by integrating molecular gas opacity without clouds.

By applying this model, we can investigate how instellation and volatile content influence the transit radius R_{transit} , which accounts for both the solid body (including magma layer) and the atmospheric thickness at P_{transit} (Fig. 6). We do not account for the potential puffiness of the magma layer relative to the solid mantle.

Since planetary mass (M_p) can often be constrained through radial velocity measurements or TTVs, we can get planet density using the transit radius: $\rho = M_p / (\frac{4}{3}\pi R_{\text{transit}}^3)$. Because the transit radius includes the atmospheric

Table 3. Model input parameters used for Monte Carlo simulations of density changes driven by atmospheric loss.

Parameter	Distribution / Range	Description
M_*	$\mathcal{U}(0.1, 1)$	Stellar mass.
M_p	$\mathcal{U}(0.5, 1)$	Planetary mass.
S/S_0	$10^{\mathcal{U}(1,4)}$	Bolometric instellation scaled to Earth value.
f_{initial}	$10^{\mathcal{U}(-4,-2)}$	Initial volatile fraction.
R_p	(a) $R_{\oplus,s}(M_p)$	Planetary radius
	(b) $\mathcal{N}(R_{\oplus,s}(M_p), \sigma_b); \sigma_b = (R_{\text{silicate},s}(M_p) - R_{\oplus,s}(M_p))/3$	
	(c) $\mathcal{N}(R_{\oplus,s}(M_p), \sigma_c); \sigma_c = (R_{\text{silicate},s}(M_p) - R_{\oplus,s}(M_p))$	

contribution, the measured density (ρ) will always be lower than the density of the solid portion of the planet alone for worlds with thick atmosphere. Comparing the observed density to theoretical models of rocky planets can help distinguish planets with substantial atmospheres from bare rocky worlds.

5.2. Monte Carlo Simulations

We use a Monte Carlo approach similar to the one described in Sec. 2, but with additional variables, incorporating the final atmospheric height after loss and the corresponding planetary density. The newly introduced variables and their distributions are listed in Table 3.

To quantify the variation in the bulk density of the solid portion of the planet (Xu & Bonsor 2021), we generate three samples under different assumptions about the distribution of planetary radii. Given a planetary mass (M_p), the radius is assigned according to the following distributions::

- (a) No Compositional Variance.: Fixed Earth-like Composition: The radius is set to $R_{\oplus,s}(M_p)$, assuming a composition of 32.5% Fe + 67.5% MgSiO₃.
- (b) Narrow Gaussian distribution: The radius is drawn from a Gaussian distribution centered at $R_{\oplus,s}(M_p)$, with a standard deviation equal to one-third of the difference between $R_{\oplus,s}(M_p)$ and $R_{\text{silicate},s}(M_p)$, where $R_{\text{silicate},s}(M_p)$ corresponds to a pure MgSiO₃ composition.
- (c) Wide Gaussian distribution: The radius is drawn from a Gaussian distribution centered at $R_{\oplus,s}(M_p)$, with a standard deviation of the difference between $R_{\oplus,s}(M_p)$ and $R_{\text{silicate},s}(M_p)$.

All calculations are based on the mass-radius relations provided by Zeng et al. (2019). Since the maximum volatile fraction in our simulations is limited to 1% of the planetary mass, we neglect any contribution of atmospheric mass to M_p . The mass-radius diagram for the solid-body of planets, showing these compositional variations, is presented in Fig. C13. The symmetric sampling of radii introduces a bias, leading to a fat tail of low-density planets. Among the tested scenarios, scenario (b) is the most realistic.

For each assumption regarding solid-body density variation, we generate 10^4 data points and compute their time-integrated atmospheric loss. Using the remaining atmosphere, we then determine the corresponding transit radius using both upper- and lower-limit estimates and density. The density is then normalized by a theoretical model of an Earth-like composition ($\rho/\rho_{\oplus,s}$) (Zeng et al. 2019).

5.3. Predictions with Cosmic Shoreline

We present the results of Monte Carlo simulations under assumptions (a) and (b) in Fig. 7. The two middle panels show planetary mass against equilibrium temperature, an alternative representation of the traditional cosmic shoreline format, as escape velocity scales with planetary mass, and equilibrium temperature is derived from instellation.

In panel b., where all planets are assumed to have an Earth-like composition, the ratio'd density $\rho/\rho_{\oplus,s}$ does not exceed 1. The light yellow dots, representing planets with a ratio'd density of 1, correspond to bare rocky planets that have completely lost their atmospheres. These planets are adjacent to the black dots, which exhibit the lowest ratio'd density due to a substantial atmospheric contribution and a more pronounced radius-boosting effect. The transition zone from yellow to black dots follows the shape of the cosmic shoreline, as shown in Fig. 3. This boundary is not

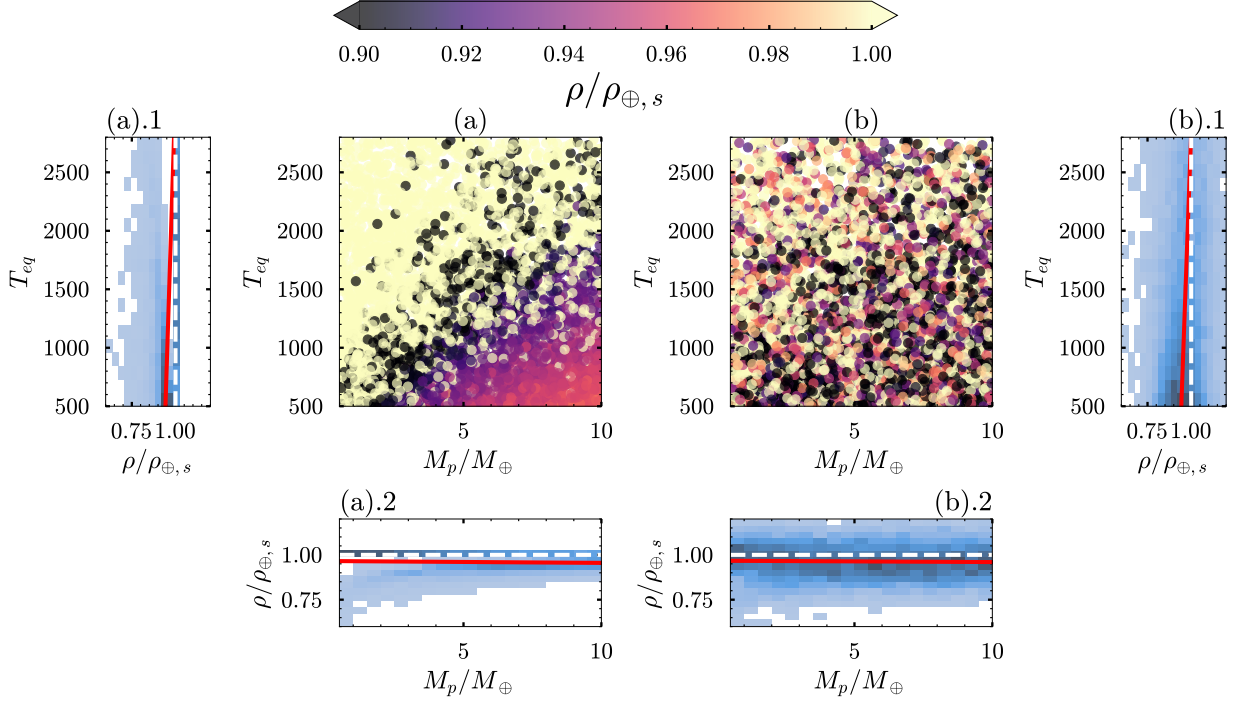


Figure 7. How the cosmic shoreline shapes the trend of ratio'd density ($\rho/\rho_{\oplus,s}$) for Different Assumptions of Solid-Body Density Distribution (Scenario (a) and (b) as seen in Table 3). Panels (a) and (b) present scatter plots of a subset of 10^3 planets, plotted as planetary mass (M_p) against equilibrium temperature (T_{eq})—an alternative representation of the traditional cosmic shoreline format, since v_{esc} scales with M_p , and T_{eq} is derived from instellation (S/S_0). The dots are color-coded by the ratio'd density with the upper-limit estimate, where atmosphere has two layers and $P_{transit} = 10^{-6}$ bar. In (a), the cosmic shoreline shapes the boundary between yellow dots (bare rocks without atmosphere) and black dots (planets where the radius-boosting effect of an atmosphere is most distinguishable). In (b), where solid-body density varies, the transition is less distinct, but a visual trend remains, with more yellow points clustered in the upper-left region (high-temperature, low-mass planets), indicating that atmospheric loss is more severe in this regime. For better visualization, the color scale is limited between 0.9 and 1.0, although actual density values can extend beyond this range. Panels (a).1 and (b).1: A bivariate histogram is computed and visualized as a heatmap, where darker colors indicate higher number density. Linear regression of $\rho/\rho_{\oplus,s}$ as a function of equilibrium temperature (T_{eq}) for the full 10,000-planet sample. A decreasing trend is observed, as planets at high T_{eq} are more likely to be bare rocks with higher densities. Panels (a).2 and (b).2: Linear regression of $\rho/\rho_{\oplus,s}$ as a function of planetary mass (M_p), also showing a decreasing trend. This is because lower-mass planets are more likely to be stripped of their atmospheres, leading to a larger fraction of high-density bare rocky planets at lower masses.

a strict cutoff but rather a transition zone influenced by factors such as initial volatile content and other parameters listed in Table 2.

Starting from the transition zone, for planets with $\rho/\rho_{\oplus,s} < 1$, the ratio'd density increases toward the lower right (higher mass, lower irradiation planets). Two key factors contribute to this effect: 1. Atmospheric survival constraint: Retaining an atmosphere requires that the initial volatile content exceeds the cumulative atmospheric mass loss over time. For planets that retain their atmospheres and lie near the cosmic shoreline corresponding to a given $f_{initial}$, their volatile inventories must surpass this threshold. The mass of the remaining atmosphere is therefore expected to be of the same order, or greater. Otherwise, the planet would have become a bare rock. From the upper left to the lower right, among the planets with atmosphere retained, planets with thinner atmospheres increasingly dominate over those with thick atmospheres. 2. Atmospheric radius-boosting effect: At higher T_{eq} , atmospheric scale heights are larger due to increased thermal expansion. This amplifies the difference in transit radius between atmosphere-bearing and stripped planets, making the contrast in ratio'd density more prominent even if the absolute atmospheric mass is similar. For smaller planets, the radius-boosting effect leads to a lower ratio'd density compared to more massive planets with the same volatile fraction (Fig. 6).

A similar but less pronounced trend appears in panel (a)-2, where the ratio'd density increases with planetary mass. This is driven by the same mechanisms: higher-mass planets have stronger gravity and stronger cooling effect, making

atmospheric retention easier, while also experiencing a less pronounced radius-boosting effect from a given atmospheric mass.

We show bivariate histograms and perform linear regression for ratio'd density as a function of T_{eq} in panel (a)-1 and as a function of planetary mass (M_p) in panel (a)-2. The horizontal line at $\rho/\rho_{\oplus,s} = 1$ consists of planets that have completely lost their atmospheres. Along this line, the color transitions from dark to light as M_p increases and T_{eq} decreases, indicating that fewer planets experience complete atmospheric loss, while more planets retain sufficient volatiles, resulting in $\rho/\rho_{\oplus,s} < 1$. Consequently, the linear regression exhibits a decreasing trend with decreasing T_{eq} .

In panel (a)-1, at high T_{eq} , a distinct gap appears between the atmosphere-bearing planets ($\rho/\rho_{\oplus,s} < 1$) and the completely stripped rocky cores ($\rho/\rho_{\oplus,s} = 1$). As T_{eq} decreases, the gap narrows, reflecting the reduced impact of atmospheric expansion and mass loss. This trend aligns with the color transition in the scatter plot.

For assumption (b) of narrow Gaussian distribution, the variation in the solid portion's density introduces scatter, making the distinct trends observed in (a) less visually apparent. The transition zone between atmosphere-bearing and stripped planets becomes more diffuse. Despite this, the linear regression still reveals a consistent decreasing trend in ratio'd density with decreasing T_{eq} and increasing M_p , similar to (a). This suggests that despite the uncertainty in solid-body density, the underlying effect of atmospheric retention and loss, as shaped by the cosmic shoreline, remains statistically significant. We do not present results for assumption (c), as it follows a similar pattern with even greater scatter while preserving the same overall statistical behavior.

The decreasing trend in ratio'd density is statistically significant for a sample of 10,000 planets, but it may not be reliably detected with smaller sample sizes. To estimate the minimum number of observed exoplanets required to confirm this trend, we conduct a 500-time bootstrap analysis with varying sample sizes.

We do not add measurement uncertainties nor observational bias. We draw sub-samples from our 10,000-planet sample without replacement. For each subsample of a given size, we perform a linear regression to obtain the slope of the ratio'd density trend. Repeating this process 500 times, we construct a distribution of slope values for each sub-sample size. The mean slope from the 500 bootstrap trials is shown as the solid line in Fig. 8, which remains approximately constant across sample sizes. The shaded region indicates the 90% confidence interval of the slope distribution at each sample size. Where the whole shaded region crosses the line slope=0 gives an estimate of the minimum number of observed exoplanets needed to confirm the expected density trend influenced by atmospheric loss and the cosmic shoreline, with a 90% confidence.

In Fig. 8, we present the results of our bootstrap analysis for both the lower- and upper-limit estimates of the transit radius. For assumption (a), where all planets have an Earth-like composition, there is no significant difference between the two estimates. However, for assumption (b), where the solid density follows a Gaussian distribution, the required sample size for detecting the trend in the lower-limit estimate is approximately twice as large as that for the upper-limit estimate.

For assumptions (a) and (b), the decreasing trend of $\rho/\rho_{\oplus,s}$ with T_{eq} could be constrained with a sample of ~ 100 exoplanets. However, constraining the trend with planetary mass (M_p) requires a larger sample size. If the variation in solid composition is as large as in assumption (c), the required sample size exceeds 1000, making it difficult to detect the trend with near-future exoplanet observations.

Here, we propose a novel approach to examine the cosmic shoreline, but it remains challenging to achieve with current exoplanet data. Transit and emission spectroscopy remain the most effective methods for constraining the shoreline.

5.3.1. Impact of Observational Uncertainties

To assess the impact of observational uncertainties on the detectability of the density trend, we incorporated simulated measurement errors into our Monte Carlo analysis. For each planet, we randomly perturbed its mass and radius using Gaussian noise (e.g. $M_{p,obs} = \mathcal{N}(M_p, \delta_{M_p})$). We vary relative uncertainties for mass and radius (δ_{M_p}/M_p and δ_{R_p}/R_p) to represent different levels of measurement precision. This approach allows us to quantify how increasing or decreasing measurement precision affects the minimum sample size needed to statistically detect the trend in ratio'd density driven by atmospheric loss. (Fig. 9)

The results, shown in Fig. 9, indicate that when there is no variation in solid density (panel a), or when the variance is reasonably small (panel b), improving the precision of both radius and mass measurements can reduce the required sample size to fewer than 100 planets to robustly detect the expected density trend. However, if the standard variance exceeds the difference between pure-silicate and Earth-like compositions (panel c), improving measurement precision

90% confidence interval to detect the trend

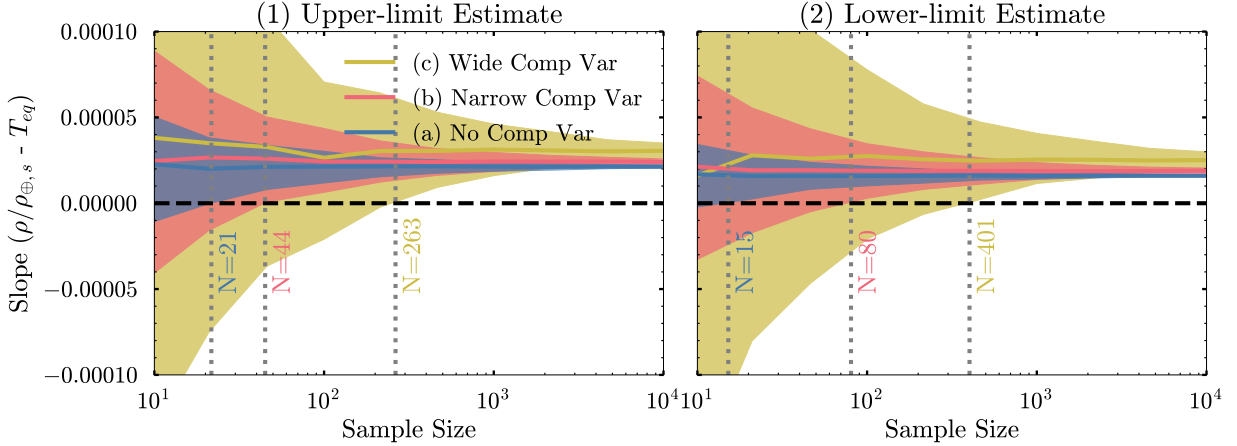


Figure 8. Constraining the slope of ratio'd density trends with varying sample sizes. The y-values corresponds to the slope of the scaled density ($\rho/\rho_{\oplus,s}$) as a function of planetary mass (M_p), which is negative when considering the full sample of 10^4 simulated planets. Panel (1) corresponds to the upper-limit estimate of the transit radius, where atmosphere has two layers and $P_{transit} = 10^{-6}$ bar, while panel (2) represents the lower-limit estimate, where atmosphere has three layers and $P_{transit} = 0.02$ bar. The solid lines indicate the median slope values derived from bootstrap resampling, while the shaded regions represent the 90% confidence intervals. Different colors represent assumptions for solid-body density: (a, blue) fixed Earth-like composition; (b, red) Gaussian scatter with $\sigma = 1/3$ the difference between pure-silicate and earth-like; (c, orange) wider Gaussian with $\sigma =$ full silicate–Earth difference. The results illustrate how increasing the sample size improves the precision of the slope estimation.

has barely no effect. In this case, the measurement uncertainty is smaller than the intrinsic variation introduced by the solid component, and the atmospheric contribution is too minor to be distinguished.

Although radius measurements are typically more precise than mass measurements today, further improving radius precision is more effective for detecting density trends. This is because, given the scaling relation $R_{\oplus,s} = M_{\text{obs}}^\alpha$, the scaled density can be calculated with the measured radius and mass as $\rho_{\oplus,s} = (M_{\text{obs}}^\alpha / R_{\text{obs}})^3$, and their fractional uncertainties propagate as

$$\frac{\sigma_{\rho_{\oplus,s}}}{\rho_{\oplus,s}} = \sqrt{\left(3\alpha \cdot \frac{\sigma_M}{M_{\text{obs}}}\right)^2 + \left(3 \cdot \frac{\sigma_R}{R_{\text{obs}}}\right)^2}. \quad (9)$$

For Earth-like compositions, $\alpha \sim 0.27$ (Zeng et al. 2019), meaning the uncertainty in $\rho_{\oplus,s}$ is more sensitive to uncertainties in radius than in mass. As a result, achieving a desired sample size for trend detection requires more accurate radius measurements than mass measurements.

6. DISCUSSION

The hydrodynamic simulations discussed in Sec. 2.3 have many uncertainties. These simulations provide atmospheric loss rates as a function of XUV flux; however, the XUV wavelength range varies across models. For example, Tian (2009) and Johnstone (2020) consider XUV wavelengths up to 1050 Å and 1000 Å, respectively, while Nakayama et al. (2022) restricts the range to 910 Å to exclude Lyman-α emission. Although the resulting impact is not explicitly included in our model, it is expected to fall within the uncertainties of our EUV extrapolation, as Ribas et al. (2005) shows that the flux ratio between 920–1180 Å and 1–920 Å is 0.03 for a 0.1 Gyr star and 0.2 for the Sun.

Additionally, Table 1 in Johnstone (2020) provides an X-ray-to-EUV relation that deviates from our EUV extrapolation, suggesting differences in spectral shapes between our model and their input, as well as potential differences from other hydrodynamic simulations. We do not know the cause of the difference. However, Johnstone et al. (2021) show a relation consistent with our model (Fig. C3).

Nakayama et al. (2022) show that atomic line cooling of C, N, and O can cool the upper atmosphere sufficiently to prevent hydrodynamic escape. The high efficiency of those metal emissions was earlier emphasised in Liu & Tian (2018). Lyman-α cooling (e.g., Murray-Clay et al. 2009; Zhang et al. 2022b) is prominent in H₂-rich atmospheres, along with molecular cooling (Yoshida et al. 2022, 2024) and a range of cooling lines in rock vapour atmospheres (Ito &

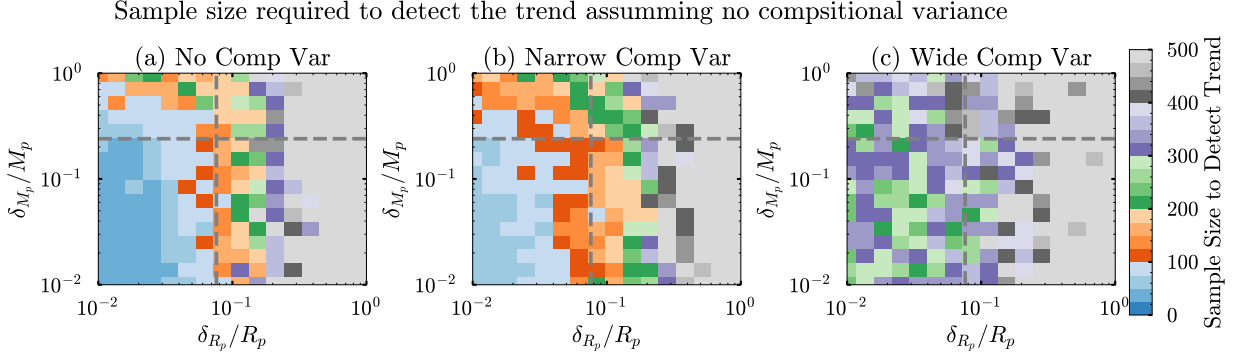


Figure 9. Sample size required to detect the trend as a function of relative measurement uncertainties in radius and mass, for three different assumptions of the variance of solid-portion’s density: (a) fixed Earth-like composition; (b) Gaussian scatter with $\sigma = 1/3$ the difference between pure-silicate and earth-like; (c) wider Gaussian with $\sigma =$ full silicate–Earth difference. The vertical and horizontal dashed lines indicate the average relative uncertainties in mass and radius for our rocky planet sample (see Sec. 4.3.1) for sample details.

Ikoma 2021). However, some inconsistencies exist between Nakayama et al. (2022) and other studies. Chatterjee & Pierrehumbert (2024) suggest that in the scenarios modeled by Nakayama et al. (2022), considering an ionized exobase would push the atmosphere into a hydrodynamic regime, enhancing escape. Furthermore, including ambipolar diffusion could increase the escape rate. More work is needed to understand these processes to interpret JWST data or provide predictions for JWST searches.

In this study, we argue that the solid mantle volatile content is much smaller than the volatile in magma and atmosphere. However, if the initial volatile inventory is high, even a small fraction trapped in the mantle could later form a detectable atmosphere via volcanism. Additionally, for N_2 -dominated atmospheres, revival through a water loss redox pump is more likely, which is time-dependent (Wordsworth 2016; Schaefer et al. 2016; Kite & Schaefer 2021). Thus models that incorporate escape-driven magma ocean solidification, chemical equilibrium, mantle outgassing, and atmospheric evolution along with stellar evolution are needed for future work (e.g., Kite & Barnett 2020; Krissansen-Totton 2023; Krissansen-Totton et al. 2024).

The EUV extrapolation in our model assumes that the solar spectrum is representative of other stars, which may overlook the diversity in stellar properties and activity levels. For X-ray flux, we adopt standard evolutionary models, though stellar behavior can vary among stars of the same mass (Penz et al. 2008), for example, differences in initial rotation rates can result in varying durations of the saturated phase (Tu et al. 2015; Johnstone et al. 2021). Additionally, our model does not account for contributions from energetic flares (do Amaral et al. 2022; Pass et al. 2025). While we incorporate a wide uncertainty range—varying by more than a factor of 20 (Fig. C3)—and statistically determine the cosmic shoreline to account for these variations, future work could explore these factors explicitly.

We tested a non-thermal ion escape rate for CO_2 -dominated atmospheres using the results from Chin et al. (2024); Dong et al. (2017); Wood et al. (2021), and find that is two orders of magnitude lower than thermal escape rates and therefore exclude them. Additionally, impact erosion can significantly strip atmospheres, particularly during the early stages of planetary formation (e.g., Schlichting & Mukhopadhyay 2018; Kegerreis et al. 2020; Wyatt et al. 2020). The influence of planetary magnetic fields, which can mitigate atmospheric escape Cohen et al. (2014), and the role of occasional but intense stellar activity cycles in modulating escape rates, also warrant further investigation (Wagner 1988; Chadney et al. 2015; Levine et al. 2024; Pass et al. 2025).

This study provides a first-step analysis of how density trends can be used to test the cosmic shoreline (Sec. 5), but it is based on simplified assumptions and considers only CO_2 -dominated atmospheres. Future work might expand to include atmospheres with varied compositions and incorporate a more realistic atmospheric structure, especially for the possible thermal inversion under high-pressure and high-temperature conditions (Selsis et al. 2023), and determine transit radii using detailed radiative transfer calculations.

In Sec. 5, we only considered density variations in the solid body while centering the composition around an Earth-like composition. We also did a sensitivity test with an alternative assumption where planetary radii are uniformly distributed between $R_{\text{silicate}}(M_p)$ and $R_{\text{iron}}(M_p)$. Under this assumption, the scaled density ρ/ρ_\oplus^* retains the same decreasing trend with decreasing equilibrium temperature. However, it exhibits an increasing trend with planetary

mass. This arises from the intrinsic mass-radius relation of the solid body alone (see Fig. C13), where more massive planets tend to have higher solid-body densities. This introduces a potential complication in interpreting the trend, as any dependence of solid-body composition on M_p and/or T_{eq} could contribute to or alter the pattern. Further investigation is needed to disentangle the influence of atmospheric retention from intrinsic density variations of the planetary core (Valencia et al. 2007; Rogers & Seager 2010).

Even if the density variations are centered around an Earth-like composition, our results indicate that achieving statistically significant conclusions with near-future datasets will be challenging, but improved observational uncertainties in the future might reduce the required sample size. Therefore, JWST transmission and emission spectroscopy remain the most effective methods for detecting atmospheres on rocky planets and testing the cosmic shoreline.

7. CONCLUSION

With the cosmic shoreline defined as the critical bolometric instellation (S_{bol}^*) above which a planet is highly unlikely to retain its atmosphere, given the mass of volatile available for loss, we use the results of previous hydrodynamic atmospheric models (Tian 2009; Tian et al. 2009; Johnstone 2020; Nakayama et al. 2022; Chatterjee & Pierrehumbert 2024) and stellar evolution models (Baraffe et al. 2015; Jackson et al. 2012; Selsis et al. 2023; King & Wheatley 2020) and find:

1. Most Rocky Worlds DDT targets fall on the unfavorable side of the original cosmic shoreline proposed by Zahnle & Catling (2017). However, our hydrodynamic escape-based shoreline models are more optimistic, showing tens of exoplanets may be capable of retaining atmospheres if they began with sufficient volatile inventories. 55 Cnc e, which has a confirmed atmosphere, lies beyond the traditional cosmic shoreline but remains within our revised CO_2 and N_2 shorelines assuming an initial volatile mass fraction of 1% of the planetary mass.
2. Cosmic shoreline as a transition zone: The location of the cosmic shoreline depends on atmospheric composition and initial volatile content. Instead of a sharp dividing line, we expect a gradual transition between airless worlds and planets retaining substantial atmospheres. Non-linearities in the relationship between escape rate and XUV flux can reduce the shoreline's variation with volatile abundance. Atmosphere non-detection can help constrain the maximum volatile content which may apply for other planets in the system.
3. Dependence on stellar mass: The cosmic shoreline shifts toward higher instellation with increasing stellar mass, due not only to the lower cumulative XUV output of higher-mass stars, but also to nonlinearities in the relationship between escape rate and XUV flux. As a result, planets orbiting Sun-like stars are more likely to retain their atmospheres compared to those around lower-mass stars.
4. Dependence on planetary mass: With hydrodynamic escape-based models, the scaling of the shoreline with escape velocity is non-uniform. Due to the effects of atomic line cooling, volatile-rich super-Earths may be highly resilient to catastrophic photoevaporation even on close-in orbits around low mass stars. Studies of the collisional-radiative nonequilibrium of super-Earth ionospheres under intense XUV irradiation are needed to constrain this regime.
5. New metric for atmosphere retention: We introduce a priority metric that quantifies the difference between a planet's instellation and the critical instellation required for atmospheric retention at a given planetary mass. A ranked list of select exoplanets based on this metric is provided in Table 3. Our results highlight TOI-4559 b and TOI-771 b as potentially rocky planets with high observability metrics that are likely to retain atmospheres.
6. Testing the cosmic shoreline with ratio'd density: Due to the radius-boosting effect of atmospheres, the ratio'd density (ρ/ρ_\oplus^*) provides an alternative way to test the cosmic shoreline. Since atmospheric retention becomes less likely at higher instellation, an increasing trend in scaled density with increasing instellation could be tested. Improving radius and mass measurement precision could reduce the required sample size to fewer than 100 exoplanets.

ACKNOWLEDGMENTS

This work was supported by NASA award No.80NSSC21K1718, which is part of the Habitable Worlds program. R.D.C also acknowledges support from the UK Science and Technology Facilities Council (STFC) and the Alfred P. Sloan Foundation under grant G202114194 (AETHeR). This research has made use of the NASA Exoplanet Archive, which is operated by the California Institute of Technology, under contract with the National Aeronautics and Space Administration under the Exoplanet Exploration Program. We thank Michael Zhang, Bowen Fan, David Catling, Ted Bergin, Dorian Abbot, RJ Graham, Robin Wordsworth, Jegug Ih, Madison Brady, Caroline Piaulet, Lily Zhao, Rafa Luque, Tim Lichtenberg, Ray Pierrehumbert and Oli Shorttle for insightful discussions.

Software: Numpy (Harris et al. 2020), Matplotlib (Hunter 2007), statsmodels.api (Seabold & Perktold 2010), Scipy (Virtanen et al. 2020), pandas (pandas development team 2020), SciencePlots (Garrett 2021)

REFERENCES

- Adibekyan, V., Deal, M., Dorn, C., et al. 2024, *Astronomy and Astrophysics*, 692, A67, doi: [10.1051/0004-6361/202452193](https://doi.org/10.1051/0004-6361/202452193)
- Andraut, D., Bolfan-Casanova, N., Nigro, G. L., et al. 2011, *Earth and Planetary Science Letters*, 304, 251, doi: [10.1016/j.epsl.2011.02.006](https://doi.org/10.1016/j.epsl.2011.02.006)
- August, P. C., Buchhave, L. A., Diamond-Lowe, H., et al. 2025, *Astronomy & Astrophysics*, 695, A171, doi: [10.1051/0004-6361/202452611](https://doi.org/10.1051/0004-6361/202452611)
- Baraffe, I., Homeier, D., Allard, F., & Chabrier, G. 2015, *Astronomy & Astrophysics*, 577, A42, doi: [10.1051/0004-6361/201425481](https://doi.org/10.1051/0004-6361/201425481)
- Barnes, R. 2017, *Celestial mechanics and dynamical astronomy*, 129, 509
- Berger, T. A., Huber, D., Gaidos, E., Van Saders, J. L., & Weiss, L. M. 2020, *The Astronomical Journal*, 160, 108, doi: [10.3847/1538-3881/aba18a](https://doi.org/10.3847/1538-3881/aba18a)
- Bergin, E. A., Blake, G. A., Ciesla, F., Hirschmann, M. M., & Li, J. 2015, *Proceedings of the National Academy of Sciences*, 112, 8965, doi: [10.1073/pnas.1500954112](https://doi.org/10.1073/pnas.1500954112)
- Bergin, E. A., Kempton, E. M.-R., Hirschmann, M., et al. 2023, *The Astrophysical Journal Letters*, 949, L17, doi: [10.3847/2041-8213/acd377](https://doi.org/10.3847/2041-8213/acd377)
- Blanchard, I., Rubie, D., Jennings, E., et al. 2022, *Earth and Planetary Science Letters*, 580, 117374, doi: [10.1016/j.epsl.2022.117374](https://doi.org/10.1016/j.epsl.2022.117374)
- Bond, J. C., Lauretta, D. S., & O'Brien, D. P. 2010, *Icarus*, 205, 321, doi: [10.1016/j.icarus.2009.07.037](https://doi.org/10.1016/j.icarus.2009.07.037)
- Brinkman, C. L., Weiss, L. M., Dai, F., et al. 2023, *The Astronomical Journal*, 165, 88
- Caldirolì, A., Haardt, F., Gallo, E., et al. 2022, *Astronomy & Astrophysics*, 663, A122, doi: [10.1051/0004-6361/202142763](https://doi.org/10.1051/0004-6361/202142763)
- Catling, D. C., & Kasting, J. F. 2017, *Atmospheric Evolution on Inhabited and Lifeless Worlds* (Cambridge University Press).
<https://ui.adsabs.harvard.edu/abs/2017aeil.book.....C>
- Chadney, J. M., Galand, M., Unruh, Y. C., Koskinen, T. T., & Sanz-Forcada, J. 2015, *Icarus*, 250, 357, doi: [10.1016/j.icarus.2014.12.012](https://doi.org/10.1016/j.icarus.2014.12.012)
- Chatterjee, R. D., & Pierrehumbert, R. T. 2024, *Novel Physics of Escaping Secondary Atmospheres May Shape the Cosmic Shoreline*, arXiv, doi: [10.48550/arXiv.2412.05188](https://doi.org/10.48550/arXiv.2412.05188)
- Chen, H., & Jacobson, S. A. 2022, *Earth and Planetary Science Letters*, 594, 117741, doi: [10.1016/j.epsl.2022.117741](https://doi.org/10.1016/j.epsl.2022.117741)
- Chin, L., Dong, C., & Lingam, M. 2024, *The Astrophysical Journal Letters*, 963, L20, doi: [10.3847/2041-8213/ad27d8](https://doi.org/10.3847/2041-8213/ad27d8)
- Cloutier, R., & Menou, K. 2020, *The Astronomical Journal*, 159, 211, doi: [10.3847/1538-3881/ab8237](https://doi.org/10.3847/1538-3881/ab8237)
- Cohen, O., Drake, J. J., Gloer, A., et al. 2014, *The Astrophysical Journal*, 790, 57, doi: [10.1088/0004-637X/790/1/57](https://doi.org/10.1088/0004-637X/790/1/57)
- Coy, B. P., Ih, J., Kite, E. S., et al. 2024, *Population-level Hypothesis Testing with Rocky Planet Emission Data: A Tentative Trend in the Brightness Temperatures of M-Earths*, arXiv, doi: [10.48550/arXiv.2412.06573](https://doi.org/10.48550/arXiv.2412.06573)
- Crossfield, I. J. M., Malik, M., Hill, M. L., et al. 2022, *The Astrophysical Journal Letters*, 937, L17, doi: [10.3847/2041-8213/ac886b](https://doi.org/10.3847/2041-8213/ac886b)
- Demory, B.-O., Gillon, M., De Wit, J., et al. 2016, *Nature*, 532, 207, doi: [10.1038/nature17169](https://doi.org/10.1038/nature17169)
- Denman, T. R., Leinhardt, Z. M., Carter, P. J., & Mordasini, C. 2020, *Monthly Notices of the Royal Astronomical Society*, 496, 1166, doi: [10.1093/mnras/staa1623](https://doi.org/10.1093/mnras/staa1623)

- do Amaral, L. N. R., Barnes, R., Segura, A., & Luger, R. 2022, *The Astrophysical Journal*, 928, 12, doi: [10.3847/1538-4357/ac53af](https://doi.org/10.3847/1538-4357/ac53af)
- Dong, C., Jin, M., Lingam, M., et al. 2018, *Proceedings of the National Academy of Sciences*, 115, 260, doi: [10.1073/pnas.1708010115](https://doi.org/10.1073/pnas.1708010115)
- Dong, C., Lingam, M., Ma, Y., & Cohen, O. 2017, *The Astrophysical Journal Letters*, 837, L26, doi: [10.3847/2041-8213/aa6438](https://doi.org/10.3847/2041-8213/aa6438)
- Elkins-Tanton, L. 2008, *Earth and Planetary Science Letters*, 271, 181, doi: [10.1016/j.epsl.2008.03.062](https://doi.org/10.1016/j.epsl.2008.03.062)
- Erkaev, N. V., Lammer, H., Odert, P., et al. 2016, *Monthly Notices of the Royal Astronomical Society*, 460, 1300, doi: [10.1093/mnras/stw935](https://doi.org/10.1093/mnras/stw935)
- . 2013, *Astrobiology*, 13, 1011, doi: [10.1089/ast.2012.0957](https://doi.org/10.1089/ast.2012.0957)
- Fischer-Gödde, M., & Kleine, T. 2017, *Nature*, 541, 525, doi: [10.1038/nature21045](https://doi.org/10.1038/nature21045)
- Gaidos, E., Claytor, Z., Dungee, R., Ali, A., & Feiden, G. A. 2023, *Monthly Notices of the Royal Astronomical Society*, 520, 5283, doi: [10.1093/mnras/stad343](https://doi.org/10.1093/mnras/stad343)
- Gao, P., & Powell, D. 2021, *The Astrophysical Journal Letters*, 918, L7, doi: [10.3847/2041-8213/ac139f](https://doi.org/10.3847/2041-8213/ac139f)
- Gao, P., Thorngren, D. P., Lee, E. K. H., et al. 2020, *Nature Astronomy*, 4, 951, doi: [10.1038/s41550-020-1114-3](https://doi.org/10.1038/s41550-020-1114-3)
- Garrett, J. D. 2021, doi: [10.5281/zenodo.4106649](https://doi.org/10.5281/zenodo.4106649)
- Gordon, S., & McBride, B. J. 1994, *Computer program for calculation of complex chemical equilibrium compositions and applications. Part 1: Analysis*, Tech. rep., NASA. <https://ntrs.nasa.gov/citations/19950013764>
- Greene, T. P., Bell, T. J., Ducrot, E., et al. 2023, *Nature*, 618, 39, doi: [10.1038/s41586-023-05951-7](https://doi.org/10.1038/s41586-023-05951-7)
- Gronoff, G., Arras, P., Baraka, S., et al. 2020, *Journal of Geophysical Research: Space Physics*, 125, e2019JA027639, doi: [10.1029/2019JA027639](https://doi.org/10.1029/2019JA027639)
- Gu, J. T., Peng, B., Ji, X., et al. 2024, *Earth and Planetary Science Letters*, 629, 118618, doi: [10.1016/j.epsl.2024.118618](https://doi.org/10.1016/j.epsl.2024.118618)
- Guinan, E. F., Engle, S. G., & Durbin, A. 2016, *The Astrophysical Journal*, 821, 81, doi: [10.3847/0004-637X/821/2/81](https://doi.org/10.3847/0004-637X/821/2/81)
- Halliday, A. N. 2013, *Geochimica et Cosmochimica Acta*, 105, 146, doi: [10.1016/j.gca.2012.11.015](https://doi.org/10.1016/j.gca.2012.11.015)
- Harris, C. R., Millman, K. J., van der Walt, S. J., et al. 2020, *Nature*, 585, 357, doi: [10.1038/s41586-020-2649-2](https://doi.org/10.1038/s41586-020-2649-2)
- Hasegawa, Y., & Swain, M. R. 2024, *The Astrophysical Journal Letters*, 973, L46, doi: [10.3847/2041-8213/ad7957](https://doi.org/10.3847/2041-8213/ad7957)
- Hier-Majumder, S., & Hirschmann, M. M. 2017, *Geochemistry, Geophysics, Geosystems*, 18, 3078, doi: [10.1002/2017GC006937](https://doi.org/10.1002/2017GC006937)
- Hirschmann, M. M., Bergin, E. A., Blake, G. A., Ciesla, F. J., & Li, J. 2021, *Proceedings of the National Academy of Sciences*, 118, e2026779118, doi: [10.1073/pnas.2026779118](https://doi.org/10.1073/pnas.2026779118)
- Ho, C. S. K., & Van Eylen, V. 2023, *Monthly Notices of the Royal Astronomical Society*, 519, 4056, doi: [10.1093/mnras/stac3802](https://doi.org/10.1093/mnras/stac3802)
- Hord, B. J., Kempton, E. M.-R., Evans-Soma, T. M., et al. 2024, *The Astronomical Journal*, 167, 233, doi: [10.3847/1538-3881/ad3068](https://doi.org/10.3847/1538-3881/ad3068)
- Hu, R., Bello-Arufe, A., Zhang, M., et al. 2024, *Nature*, 630, 609, doi: [10.1038/s41586-024-07432-x](https://doi.org/10.1038/s41586-024-07432-x)
- Hunter, J. D. 2007, *Computing in Science & Engineering*, 9, 90, doi: [10.1109/MCSE.2007.55](https://doi.org/10.1109/MCSE.2007.55)
- Ito, Y., & Ikoma, M. 2021, *Monthly Notices of the Royal Astronomical Society*, 502, 750, doi: [10.1093/mnras/staa3962](https://doi.org/10.1093/mnras/staa3962)
- Jackson, A. P., Davis, T. A., & Wheatley, P. J. 2012, *Monthly Notices of the Royal Astronomical Society*, 422, 2024, doi: [10.1111/j.1365-2966.2012.20657.x](https://doi.org/10.1111/j.1365-2966.2012.20657.x)
- Johansen, A., Ronnet, T., Schiller, M., Deng, Z., & Bizzarro, M. 2023, *Astronomy & Astrophysics*, 671, A76, doi: [10.1051/0004-6361/202142143](https://doi.org/10.1051/0004-6361/202142143)
- Johnstone, C. P. 2020, *The Astrophysical Journal*, 890, 79, doi: [10.3847/1538-4357/ab6224](https://doi.org/10.3847/1538-4357/ab6224)
- Johnstone, C. P., Bartel, M., & Güdel, M. 2021, *Astronomy & Astrophysics*, 649, A96, doi: [10.1051/0004-6361/202038407](https://doi.org/10.1051/0004-6361/202038407)
- Johnstone, C. P., Güdel, M., Lammer, H., & Kislyakova, K. G. 2018, *Astronomy & Astrophysics*, 617, A107, doi: [10.1051/0004-6361/201832776](https://doi.org/10.1051/0004-6361/201832776)
- Johnstone, C. P., Khodachenko, M. L., Lüftinger, T., et al. 2019, *Astronomy & Astrophysics*, 624, L10, doi: [10.1051/0004-6361/201935279](https://doi.org/10.1051/0004-6361/201935279)
- Jontof-Hutter, D. 2019, *Annual Review of Earth and Planetary Sciences*, 47, 141, doi: [10.1146/annurev-earth-053018-060352](https://doi.org/10.1146/annurev-earth-053018-060352)
- Kegerreis, J. A., Eke, V. R., Catling, D. C., et al. 2020, *The Astrophysical Journal*, 901, L31, doi: [10.3847/2041-8213/abb5fb](https://doi.org/10.3847/2041-8213/abb5fb)
- Kempton, E. M. R., Bean, J. L., Louie, D. R., et al. 2018, *Publications of the Astronomical Society of the Pacific*, 130, 114401, doi: [10.1088/1538-3873/aadf6f](https://doi.org/10.1088/1538-3873/aadf6f)
- King, G. W., & Wheatley, P. J. 2020, *Monthly Notices of the Royal Astronomical Society: Letters*, 501, L28, doi: [10.1093/mnrasl/slaa186](https://doi.org/10.1093/mnrasl/slaa186)
- King, G. W., Wheatley, P. J., Salz, M., et al. 2018, *Monthly Notices of the Royal Astronomical Society*, doi: [10.1093/mnras/sty1110](https://doi.org/10.1093/mnras/sty1110)

- Kite, E. S., & Barnett, M. N. 2020, *Proceedings of the National Academy of Sciences*, 117, 18264, doi: [10.1073/pnas.2006177117](https://doi.org/10.1073/pnas.2006177117)
- Kite, E. S., Fegley Jr, B., Schaefer, L., & Gaidos, E. 2016, *The Astrophysical Journal*, 828, 80
- Kite, E. S., Manga, M., & Gaidos, E. 2009, *The Astrophysical Journal*, 700, 1732, doi: [10.1088/0004-637X/700/2/1732](https://doi.org/10.1088/0004-637X/700/2/1732)
- Kite, E. S., & Schaefer, L. 2021, *The Astrophysical Journal Letters*, 909, L22, doi: [10.3847/2041-8213/abe7dc](https://doi.org/10.3847/2041-8213/abe7dc)
- Kral, Q., Wyatt, M. C., Triaud, A. H. M. J., et al. 2018, *Monthly Notices of the Royal Astronomical Society*, 479, 2649, doi: [10.1093/mnras/sty1677](https://doi.org/10.1093/mnras/sty1677)
- Krasnopolsky, V. A., Maillard, J. P., & Owen, T. C. 2004, *Icarus*, 172, 537, doi: [10.1016/j.icarus.2004.07.004](https://doi.org/10.1016/j.icarus.2004.07.004)
- Kreidberg, L., Koll, D. D. B., Morley, C., et al. 2019, *Nature*, 573, 87, doi: [10.1038/s41586-019-1497-4](https://doi.org/10.1038/s41586-019-1497-4)
- Krissansen-Totton, J. 2023, *The Astrophysical Journal Letters*, 951, L39, doi: [10.3847/2041-8213/acdc26](https://doi.org/10.3847/2041-8213/acdc26)
- Krissansen-Totton, J., Wogan, N., Thompson, M., & Fortney, J. J. 2024, *Nature Communications*, 15, 8374, doi: [10.1038/s41467-024-52642-6](https://doi.org/10.1038/s41467-024-52642-6)
- Levine, W. G., Vissapragada, S., Feinstein, A. D., et al. 2024, *The Astronomical Journal*, 168, 65, doi: [10.3847/1538-3881/ad5354](https://doi.org/10.3847/1538-3881/ad5354)
- Lichtenberg, T., Bower, D. J., Hammond, M., et al. 2021a, *Journal of Geophysical Research: Planets*, 126, e2020JE006711, doi: [10.1029/2020JE006711](https://doi.org/10.1029/2020JE006711)
- Lichtenberg, T., Drażkowska, J., Schönbächler, M., Golabek, G. J., & Hands, T. O. 2021b, *Science*, 371, 365, doi: [10.1126/science.abb3091](https://doi.org/10.1126/science.abb3091)
- Lichtenberg, T., Golabek, G. J., Burn, R., et al. 2019, *Nature Astronomy*, 3, 307, doi: [10.1038/s41550-018-0688-5](https://doi.org/10.1038/s41550-018-0688-5)
- Liu, B., Johansen, A., Lambrechts, M., Bizzarro, M., & Haugbølle, T. 2022, *Science Advances*, 8, eabm3045, doi: [10.1126/sciadv.abm3045](https://doi.org/10.1126/sciadv.abm3045)
- Liu, L., & Tian, F. 2018, *Earth and Planetary Physics*, 2, 22, doi: [10.26464/epp2018003](https://doi.org/10.26464/epp2018003)
- Lock, S. J., & Stewart, S. T. 2017, *Journal of Geophysical Research: Planets*, 122, 950, doi: [10.1002/2016JE005239](https://doi.org/10.1002/2016JE005239)
- Looveren, G. V., Saikia, S. B., Herbort, O., et al. 2025, *Astronomy & Astrophysics*, 694, A310, doi: [10.1051/0004-6361/202452998](https://doi.org/10.1051/0004-6361/202452998)
- Lopez, E. D., & Fortney, J. J. 2014, *The Astrophysical Journal*, 792, 1, doi: [10.1088/0004-637X/792/1/1](https://doi.org/10.1088/0004-637X/792/1/1)
- Lopez, E. D., Fortney, J. J., & Miller, N. 2012, *The Astrophysical Journal*, 761, 59, doi: [10.1088/0004-637X/761/1/59](https://doi.org/10.1088/0004-637X/761/1/59)
- Luger, R., & Barnes, R. 2015, *Astrobiology*, 15, 119, doi: [10.1089/ast.2014.1231](https://doi.org/10.1089/ast.2014.1231)
- Luque, R., & Pallé, E. 2022, *Science*, 377, 1211, doi: [10.1126/science.abl7164](https://doi.org/10.1126/science.abl7164)
- Luque, R., Coy, B. P., Xue, Q., et al. 2024, arXiv preprint arXiv:2412.03411
- Malamud, U., Podolak, M., Podolak, J. I., & Bodenheimer, P. H. 2024, *Icarus*, 421, 116217, doi: [10.1016/j.icarus.2024.116217](https://doi.org/10.1016/j.icarus.2024.116217)
- Mansfield, M. W., Xue, Q., Zhang, M., et al. 2024, No Thick Atmosphere on the Terrestrial Exoplanet Gl 486b, arXiv, doi: [10.48550/ARXIV.2408.15123](https://doi.org/10.48550/ARXIV.2408.15123)
- Marty, B., & Zimmermann, L. 1999, *Geochimica et Cosmochimica Acta*, 63, 3619, doi: [10.1016/S0016-7037\(99\)00169-6](https://doi.org/10.1016/S0016-7037(99)00169-6)
- Monaghan, C., Roy, P.-A., Benneke, B., et al. 2025, Low 4.5 μ m Dayside Emission Disfavors a Dark Bare-Rock scenario for the Hot Super-Earth TOI-431 b, arXiv, doi: [10.48550/arXiv.2503.09698](https://doi.org/10.48550/arXiv.2503.09698)
- Moore, K., David, B., Zhang, A. Y., & Cowan, N. B. 2024, *The Astrophysical Journal*, 972, 131, doi: [10.3847/1538-4357/ad6444](https://doi.org/10.3847/1538-4357/ad6444)
- Murray-Clay, R. A., Chiang, E. I., & Murray, N. 2009, *The Astrophysical Journal*, 693, 23, doi: [10.1088/0004-637X/693/1/23](https://doi.org/10.1088/0004-637X/693/1/23)
- Nakayama, A., Ikoma, M., & Terada, N. 2022, *The Astrophysical Journal*, 937, 72, doi: [10.3847/1538-4357/ac86ca](https://doi.org/10.3847/1538-4357/ac86ca)
- NASA Exoplanet Archive. 2019, Confirmed Planets Table, IPAC, doi: [10.26133/NEA1](https://doi.org/10.26133/NEA1)
- Owen, J. E. 2019, *Annual Review of Earth and Planetary Sciences*, 47, 67, doi: [10.1146/annurev-earth-053018-060246](https://doi.org/10.1146/annurev-earth-053018-060246)
- Owen, J. E., & Schlichting, H. E. 2024, *Monthly Notices of the Royal Astronomical Society*, 528, 1615, doi: [10.1093/mnras/stad3972](https://doi.org/10.1093/mnras/stad3972)
- Owen, J. E., & Wu, Y. 2016, *The Astrophysical Journal*, 817, 107, doi: [10.3847/0004-637X/817/2/107](https://doi.org/10.3847/0004-637X/817/2/107)
- pandas development team, T. 2020, pandas-dev/pandas: Pandas, latest, Zenodo, doi: [10.5281/zenodo.3509134](https://doi.org/10.5281/zenodo.3509134)
- Paragas, K., Knutson, H. A., Hu, R., et al. 2025, *The Astrophysical Journal*, 981, 130
- Parviainen, H., Luque, R., & Palle, E. 2023, *Monthly Notices of the Royal Astronomical Society*, 527, 5693, doi: [10.1093/mnras/stad3504](https://doi.org/10.1093/mnras/stad3504)
- Pass, E. K., Charbonneau, D., & Vanderburg, A. 2025, The Receding Cosmic Shoreline of Mid-to-Late M Dwarfs: Measurements of Active Lifetimes Worsen Challenges for Atmosphere Retention by Rocky Exoplanets, arXiv, doi: [10.48550/arXiv.2504.01182](https://doi.org/10.48550/arXiv.2504.01182)

- Peng, B., & Valencia, D. 2024, *The Astrophysical Journal*, 976, 202, doi: [10.3847/1538-4357/ad6f03](https://doi.org/10.3847/1538-4357/ad6f03)
- Penz, T., Micela, G., & Lammer, H. 2008, *Astronomy and Astrophysics*, 477, 309, doi: [10.1051/0004-6361:20078364](https://doi.org/10.1051/0004-6361:20078364)
- Piette, A. A. A., Gao, P., Brugman, K., et al. 2023, *The Astrophysical Journal*, 954, 29, doi: [10.3847/1538-4357/acdef2](https://doi.org/10.3847/1538-4357/acdef2)
- Preibisch, T., & Feigelson, E. D. 2005, *The Astrophysical Journal Supplement Series*, 160, 390, doi: [10.1086/432094](https://doi.org/10.1086/432094)
- Raymond, S. N., Quinn, T., & Lunine, J. I. 2004, *Icarus*, 168, 1, doi: [10.1016/j.icarus.2003.11.019](https://doi.org/10.1016/j.icarus.2003.11.019)
- Redfield, S., Batalha, N., Benneke, B., et al. 2024, Report of the Working Group on Strategic Exoplanet Initiatives with HST and JWST, arXiv, doi: [10.48550/arXiv.2404.02932](https://doi.org/10.48550/arXiv.2404.02932)
- Reynard, B., & Sotin, C. 2023, *Earth and Planetary Science Letters*, 612, 118172, doi: [10.1016/j.epsl.2023.118172](https://doi.org/10.1016/j.epsl.2023.118172)
- Ribas, I., Guinan, E. F., Gudel, M., & Audard, M. 2005, *The Astrophysical Journal*, 622, 680, doi: [10.1086/427977](https://doi.org/10.1086/427977)
- Ribas, I., Bolmont, E., Selsis, F., et al. 2016, *Astronomy & Astrophysics*, 596, A111, doi: [10.1051/0004-6361/201629576](https://doi.org/10.1051/0004-6361/201629576)
- Righter, K., & O'Brien, D. P. 2011, *Proceedings of the National Academy of Sciences*, 108, 19165, doi: [10.1073/pnas.1013480108](https://doi.org/10.1073/pnas.1013480108)
- Rogers, L. A. 2015, *The Astrophysical Journal*, 801, 41, doi: [10.1088/0004-637X/801/1/41](https://doi.org/10.1088/0004-637X/801/1/41)
- Rogers, L. A., & Seager, S. 2010, *The Astrophysical Journal*, 712, 974, doi: [10.1088/0004-637X/712/2/974](https://doi.org/10.1088/0004-637X/712/2/974)
- Rubie, D. C., Jacobson, S. A., Morbidelli, A., et al. 2015, *Icarus*, 248, 89, doi: [10.1016/j.icarus.2014.10.015](https://doi.org/10.1016/j.icarus.2014.10.015)
- Sakuraba, H., Kurokawa, H., Genda, H., & Ohta, K. 2021, *Scientific Reports*, 11, 20894, doi: [10.1038/s41598-021-99240-w](https://doi.org/10.1038/s41598-021-99240-w)
- Schaefer, L., Wordsworth, R. D., Berta-Thompson, Z., & Sasselov, D. 2016, *The Astrophysical Journal*, 829, 63, doi: [10.3847/0004-637X/829/2/63](https://doi.org/10.3847/0004-637X/829/2/63)
- Schlichting, H. E., & Mukhopadhyay, S. 2018, *Space Science Reviews*, 214, 34, doi: [10.1007/s11214-018-0471-z](https://doi.org/10.1007/s11214-018-0471-z)
- Seabold, S., & Perktold, J. 2010, in *9th Python in Science Conference*
- Selsis, F., Kasting, J. F., Levrard, B., et al. 2007, *Astronomy & Astrophysics*, 476, 1373, doi: [10.1051/0004-6361:20078091](https://doi.org/10.1051/0004-6361:20078091)
- Selsis, F., Leconte, J., Turbet, M., Chaverot, G., & Bolmont, E. 2023, *Nature*, 620, 287, doi: [10.1038/s41586-023-06258-3](https://doi.org/10.1038/s41586-023-06258-3)
- Sinclair, C. A., Wyatt, M. C., Morbidelli, A., & Nesvorný, D. 2020, *Monthly Notices of the Royal Astronomical Society*, 499, 5334, doi: [10.1093/mnras/staa3210](https://doi.org/10.1093/mnras/staa3210)
- Sossi, P. A. 2021, *Nature Astronomy*, 5, 535, doi: [10.1038/s41550-021-01353-9](https://doi.org/10.1038/s41550-021-01353-9)
- Stafne, E., & Becker, J. 2024, *Research Notes of the AAS*, 8, 176, doi: [10.3847/2515-5172/ad5f30](https://doi.org/10.3847/2515-5172/ad5f30)
- Swastik, C., Banyal, R. K., Narang, M., et al. 2023, *The Astronomical Journal*, 166, 91, doi: [10.3847/1538-3881/ace782](https://doi.org/10.3847/1538-3881/ace782)
- Tian, F. 2009, *The Astrophysical Journal*, 703, 905, doi: [10.1088/0004-637X/703/1/905](https://doi.org/10.1088/0004-637X/703/1/905)
- . 2015a, *Earth and Planetary Science Letters*, 432, 126, doi: [10.1016/j.epsl.2015.09.051](https://doi.org/10.1016/j.epsl.2015.09.051)
- . 2015b, *Annual Review of Earth and Planetary Sciences*, 43, 459, doi: [10.1146/annurev-earth-060313-054834](https://doi.org/10.1146/annurev-earth-060313-054834)
- Tian, F., & Ida, S. 2015, *Nature Geoscience*, 8, 177, doi: [10.1038/ngeo2372](https://doi.org/10.1038/ngeo2372)
- Tian, F., Kasting, J. F., Liu, H.-L., & Roble, R. G. 2008a, *Journal of Geophysical Research: Planets*, 113, doi: [10.1029/2007JE002946](https://doi.org/10.1029/2007JE002946)
- Tian, F., Kasting, J. F., & Solomon, S. C. 2009, *Geophysical Research Letters*, 36, 2008GL036513, doi: [10.1029/2008GL036513](https://doi.org/10.1029/2008GL036513)
- Tian, F., Solomon, S. C., Qian, L., Lei, J., & Roble, R. G. 2008b, *Journal of Geophysical Research (Planets)*, 113, E07005, doi: [10.1029/2007JE003043](https://doi.org/10.1029/2007JE003043)
- Tu, L., Johnstone, C. P., Güdel, M., & Lammer, H. 2015, *Astronomy & Astrophysics*, 577, L3, doi: [10.1051/0004-6361/201526146](https://doi.org/10.1051/0004-6361/201526146)
- Valdés, E., Demory, B.-O., Diamond-Lowe, H., et al. 2025, arXiv preprint arXiv:2503.19772
- Valencia, D., Sasselov, D. D., & O'Connell, R. J. 2007, *The Astrophysical Journal*, 665, 1413, doi: [10.1086/519554](https://doi.org/10.1086/519554)
- Vilhu, O. 1984, *Astronomy and Astrophysics*, 133, 117, <https://ui.adsabs.harvard.edu/abs/1984A&A...133..117V>
- Virtanen, P., Gommers, R., Oliphant, T. E., et al. 2020, *Nature Methods*, 17, 261, doi: [10.1038/s41592-019-0686-2](https://doi.org/10.1038/s41592-019-0686-2)
- Wachiraphan, P., Berta-Thompson, Z. K., Diamond-Lowe, H., et al. 2024, *The Thermal Emission Spectrum of the Nearby Rocky Exoplanet LTT 1445A b from JWST MIRI/LRS*, arXiv, doi: [10.48550/ARXIV.2410.10987](https://doi.org/10.48550/ARXIV.2410.10987)
- Wagner, W. 1988, *Advances in Space Research*, 8, 67, doi: [10.1016/0273-1177\(88\)90173-1](https://doi.org/10.1016/0273-1177(88)90173-1)
- Watson, A. J., Donahue, T. M., & Walker, J. C. 1981, *Icarus*, 48, 150, doi: [10.1016/0019-1035\(81\)90101-9](https://doi.org/10.1016/0019-1035(81)90101-9)
- Wood, B. E., Müller, H.-R., Redfield, S., et al. 2021, *The Astrophysical Journal*, 915, 37, doi: [10.3847/1538-4357/abfda5](https://doi.org/10.3847/1538-4357/abfda5)
- Woods, T. N., Prinz, D. K., Rottman, G. J., et al. 1996, *Journal of Geophysical Research: Atmospheres*, 101, 9541, doi: [10.1029/96JD00225](https://doi.org/10.1029/96JD00225)
- Wordsworth, R. 2015, *The Astrophysical Journal*, 806, 180

- Wordsworth, R., Kalugina, Y., Lokshantov, S., et al. 2017, *Geophysical Research Letters*, 44, 665, doi: [10.1002/2016GL071766](https://doi.org/10.1002/2016GL071766)
- Wordsworth, R., & Kreidberg, L. 2022, *Annual Review of Astronomy and Astrophysics*, 60, 159, doi: [10.1146/annurev-astro-052920-125632](https://doi.org/10.1146/annurev-astro-052920-125632)
- Wordsworth, R. D. 2016, *Earth and Planetary Science Letters*, 447, 103, doi: [10.1016/j.epsl.2016.04.002](https://doi.org/10.1016/j.epsl.2016.04.002)
- Wordsworth, R. D., Schaefer, L. K., & Fischer, R. A. 2018, *The Astronomical Journal*, 155, 195, doi: [10.3847/1538-3881/aab608](https://doi.org/10.3847/1538-3881/aab608)
- Wyatt, M. C., Kral, Q., & Sinclair, C. A. 2020, *Monthly Notices of the Royal Astronomical Society*, 491, 782, doi: [10.1093/mnras/stz3052](https://doi.org/10.1093/mnras/stz3052)
- Xu, S., & Bonsor, A. 2021, *Exogeology from Polluted White Dwarfs*, arXiv, doi: [10.48550/arXiv.2108.08384](https://doi.org/10.48550/arXiv.2108.08384)
- Xue, Q., Bean, J. L., Zhang, M., et al. 2024, *The Astrophysical Journal Letters*, 973, L8, doi: [10.3847/2041-8213/ad72e9](https://doi.org/10.3847/2041-8213/ad72e9)
- Yoshida, T., Terada, N., Ikoma, M., & Kuramoto, K. 2022, *The Astrophysical Journal*, 934, 137, doi: [10.3847/1538-4357/ac7be7](https://doi.org/10.3847/1538-4357/ac7be7)
- Yoshida, T., Terada, N., & Kuramoto, K. 2024, *Progress in Earth and Planetary Science*, 11, 59, doi: [10.1186/s40645-024-00666-3](https://doi.org/10.1186/s40645-024-00666-3)
- Zahnle, K. J., & Catling, D. C. 2017, *The Astrophysical Journal*, 843, 122, doi: [10.3847/1538-4357/aa7846](https://doi.org/10.3847/1538-4357/aa7846)
- Zeng, L., Jacobsen, S. B., Sasselov, D. D., et al. 2019, *Proceedings of the National Academy of Sciences*, 116, 9723, doi: [10.1073/pnas.1812905116](https://doi.org/10.1073/pnas.1812905116)
- Zhang, M., Cauley, P. W., Knutson, H. A., et al. 2022a, *The Astronomical Journal*, 164, 237, doi: [10.3847/1538-3881/ac9675](https://doi.org/10.3847/1538-3881/ac9675)
- Zhang, M., Dai, F., Bean, J. L., Knutson, H. A., & Rescigno, F. 2023, *The Astrophysical Journal*, 953, L25, doi: [10.3847/2041-8213/aced51](https://doi.org/10.3847/2041-8213/aced51)
- Zhang, M., Knutson, H. A., Wang, L., Dai, F., & Barragán, O. 2022b, *The Astronomical Journal*, 163, 67, doi: [10.3847/1538-3881/ac3fa7](https://doi.org/10.3847/1538-3881/ac3fa7)
- Zhang, M., Hu, R., Inglis, J., et al. 2024, *The Astrophysical Journal Letters*, 961, L44, doi: [10.3847/2041-8213/ad1a07](https://doi.org/10.3847/2041-8213/ad1a07)
- Zieba, S., Zilinskas, M., Kreidberg, L., et al. 2022, *Astronomy & Astrophysics*, 664, A79
- Zieba, S., Kreidberg, L., Ducrot, E., et al. 2023, *Nature*, 620, 746, doi: [10.1038/s41586-023-06232-z](https://doi.org/10.1038/s41586-023-06232-z)

APPENDIX

A. CARBON DISTRIBUTION DURING MAGMA OCEAN SOLIDIFICATION

We distribute volatile between the magma, single-species atmosphere, and mantle reservoirs during magma ocean solidification as follows.

For nitrogen-rich cases, owing to the extremely low solubility of N_2 in solids, the mass of nitrogen in the residual mantle can be neglected (Hier-Majumder & Hirschmann 2017).

For carbon-rich cases, we assume that as the magma cools and crystallizes, the atmosphere remains in equilibrium with the magma ocean surface according to the solubility law (Lichtenberg et al. 2021a). Additionally, we assume that the initial mass of the magma ocean is 2/3 of the planetary mass, and we only consider the carbon distributed between magma and atmosphere but neglect the partition into Fe-alloy core (Blanchard et al. 2022). The carbon mass distribution is calculated as a function of the changing magma mass during crystallization. As the magma mass decreases, carbon is redistributed between the atmosphere, magma ocean, and solid mantle.

VARIABLES AND CONSTANTS

The key variables used in our model include C_{atm} , C_{magma} , and C_{mantle} , which represent the carbon mass in the atmosphere, magma, and mantle, respectively, with the total carbon mass C_0 remaining constant. The magma ocean mass is denoted as M_{magma} , and the carbon concentration in the magma is given by $f = C_{\text{magma}}/M_{\text{magma}}$. The partition coefficient for mantle-magma exchange is represented by D_{mm} (assumed constant). The solubility law linking surface pressure to carbon concentration in magma is parameterized by the constants α and β , following Lichtenberg et al. (2021a), such that $P_{\text{surf}} = (f/\alpha)^\beta$. To simplify calculations, we define a factor $k_{Ps} = \frac{12}{\text{MMW}} \cdot \frac{4\pi R_p^2}{g}$, where R_p is the planetary radius, g is the gravitational acceleration, and the 12/MMW factor accounts for the mean molecular ratio of carbon to atmospheric species. MMW=44 for CO_2 and MMW=16 for CH_4 . This allows the atmospheric carbon mass to be expressed as $C_{\text{atm}} = k_{Ps} \cdot P_{\text{surf}}$.

GOVERNING EQUATIONS

1. Mass Conservation:

$$C_{\text{atm}} + C_{\text{magma}} + C_{\text{mantle}} = C_0 \quad (\text{A1})$$

2. Carbon in atmosphere Lichtenberg et al. (2021a):

$$C_{\text{atm}} = k_{Ps} \left(\frac{f}{\alpha} \right)^\beta \quad (\text{A2})$$

This equation reflects the equilibrium between the atmospheric carbon and the carbon dissolved in the magma ocean surface. For CO_2 , $\alpha = 1.937 \times 10^{-15} \text{Pa}^{-1}$; $\beta = 0.714$, and for CH_4 , $\alpha = 9.937 \times 10^{-14} \text{Pa}^{-1}$; $\beta = 1.000$ (Lichtenberg et al. 2021a)

3. Carbon in Magma:

$$C_{\text{magma}} = f M_{\text{magma}} \quad (\text{A3})$$

4. Mantle Carbon Change:

$$dC_{\text{mantle}} = -D_{\text{mm}} f dM_{\text{magma}} \quad (\text{A4})$$

This equation accounts for the partition of carbon from the magma into the solid mantle during solidification, with D_{mm} representing the partitioning behavior.

DERIVATION OF THE DIFFERENTIAL EQUATION

Starting from the mass conservation equation A1, differentiating both sides and rearranging:

$$dC_{\text{mantle}} = -dC_{\text{atm}} - dC_{\text{magma}} \quad (\text{A5})$$

Differentiating equation A3:

$$dC_{\text{magma}} = f \cdot dM_{\text{magma}} + dM_{\text{magma}} \cdot df \quad (\text{A6})$$

From equation A2, express C_{atm} and differentiate:

$$dC_{\text{atm}} = k_{Ps} \alpha^{-\beta} \beta f^{\beta-1} df \quad (\text{A7})$$

Define a constant for simplification $A = k_{Ps} \alpha^{-\beta} \beta$

Substitute equations A6 and A7 into equation A5:

$$f(D_{\text{mm}} + 1) dM_{\text{magma}} + (M_{\text{magma}} + A f^{\beta-1}) df = 0 \quad (\text{A8})$$

SOLVING ODE

Let's consider M_{magma} as a function of f :

$$\frac{dM_{\text{magma}}}{df} = -\frac{M_{\text{magma}}}{f(D_{\text{mm}} + 1)} - \frac{A f^{\beta-2}}{(D_{\text{mm}} + 1)} \quad (\text{A9})$$

The ODE has the standard linear form $\frac{dM_{\text{magma}}}{df} + P(f)M_{\text{magma}} = Q(f)$, where $P(f) = \frac{1}{f(D_{\text{mm}} + 1)}$ and $Q(f) = -\frac{A f^{\beta-2}}{D_{\text{mm}} + 1}$. The integrating factor $\mu(f)$ is:

$$\mu(f) = \exp\left(\int P(f) df\right) = \exp\left(\int \frac{1}{f(D_{\text{mm}} + 1)} df\right) = f^{\frac{1}{D_{\text{mm}} + 1}} \quad (\text{A10})$$

Multiply both sides by the integrating factor and simplify:

$$\frac{d}{df} \left(f^{\frac{1}{D_{\text{mm}} + 1}} M_{\text{magma}} \right) = -\frac{A f^{\beta-2 + \frac{1}{D_{\text{mm}} + 1}}}{D_{\text{mm}} + 1} \quad (\text{A11})$$

Integrate with respect to f and let $n = \beta - 2 + \frac{1}{D_{\text{mm}} + 1}$ for simplification:

$$f^{\frac{1}{D_{\text{mm}} + 1}} M_{\text{magma}} = -\frac{A}{(D_{\text{mm}} + 1)(n + 1)} f^{n+1} + \text{const} \quad (\text{A12})$$

where the integral constant (const) can be solved by the assumed initial condition.

INTEGRAL CONSTANT DETERMINED BY INITIAL CONDITION

We assume the initial magma mass is $M_{\text{magma},0} = 2/3 M_p$, and the carbon is only distributed between magma and the atmosphere. With the solubility law, we can write down the mass conservation equation as:

$$C_0 = C_{\text{atm},0} + C_{\text{magma},0} = k_{Ps} \left(\frac{f_0}{\alpha} \right)^\beta + f_0 M_{\text{magma},0} \quad (\text{A13})$$

The equation can be solved numerically with the given total carbon mass C_0 . And plug it back into equation A12, we can get the value of const.

Rearrange equation A12, the final expression of M_{magma} in terms of f is:

$$M_{\text{magma}} = \frac{A f^{\beta-1}}{(D_{\text{mm}} - 1) \left(\beta - 1 + \frac{1}{1 - D_{\text{mm}}} \right)} + \text{const} f^{-\frac{1}{1 - D_{\text{mm}}}} \quad (\text{A14})$$

Where:

- $A = \frac{12}{\text{MMW}} \cdot \frac{4\pi R_p^2}{g} \cdot \beta \alpha^{-\beta}$
- $\text{const} = f_0^{\frac{1}{D_{\text{mm}} + 1}} M_{\text{magma},0} + \frac{A}{(D_{\text{mm}} + 1)(n + 1)} f_0^{n+1}$

We have derived the differential equation considering how carbon partition into the solid mantle with the solidification of magma ocean $dC_{\text{mantle}} = -f D_{\text{mm}} dM_{\text{magma}}$ and solved it to find how M_{magma} evolves with f . Using this solution, we can determine the evolution of all other variables with a given M_{magma} .

When setting $M_{\text{magma}} = 0$, that is the phase after fully solidification of the primordial magma ocean. And we show the distribution of carbon in different reservoirs in Fig. A1.

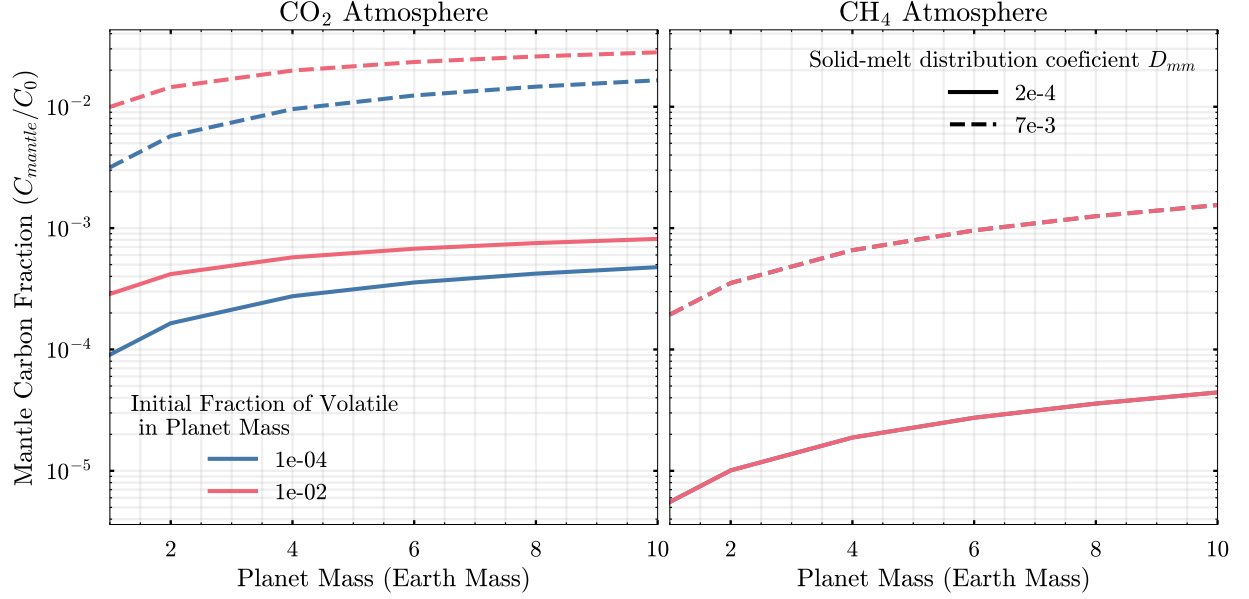


Figure A1. The fraction of carbon sequestered in the mantle relative to the total carbon mass after complete magma ocean solidification, shown as a function of planetary mass, for a pure-CO₂ atmosphere (left) and a pure-CH₄ atmosphere (right). The fraction increases with planetary mass due to the solubility law, which governs surface pressure, and the reduced atmospheric column mass at higher gravity with a given surface pressure. The blue line represents the lowest initial carbon case in our study, where the carbon-to-planetary mass ratio is $10^{-4} M_p$, while the pink line corresponds to the most carbon-rich case, $10^{-2} M_p$. A higher initial carbon concentration in the magma ocean results in more carbon being retained in the mantle post-solidification. Solid lines indicate a conservative solid-melt partition coefficient, while dashed lines represent a higher partition coefficient, following [Elkins-Tanton \(2008\)](#).

B. APPENDIX TABLE

Table B1. Atmospheric Retention Targets Ranked by Priority Metric for CO₂-Dominated Atmospheres

Planet	Priority Metric			R_p (R_\oplus)	M_p (M_\oplus)	v_{esc} (km/s)	ρ ¹⁰ (ρ_\oplus^*)	M_* (M_\odot)	T_{eq} (K)	K-mag	$(R_p/R_s)^2$ (ppm)	ESM ¹¹	TSM ¹²
	[CO ₂]	[CH ₄]	[N ₂]										
K2-91 b	-0.02	-1.07	-0.16	1.22	2.05 [†]	14.5 [†]	1 [†]	0.38	761	10.6	1217	3.3	6 [†]
TOI-1416 b	-0.05	-1.36	-0.17	1.62	3.48	16.4	0.65	0.80	1515	7.7	351	9.6	82
LHS 1678 d	-0.09	-0.71	-0.87	0.98	0.94 [†]	11.0 [†]	1 [†]	0.34	483	8.3	747	1.4	13 [†]
K2-415 b	-0.11	-0.79	-0.77	1.01	1.06 [†]	11.4 [†]	1 [†]	0.16	412	9.9	2243	1.2	14 [†]
TOI-1444 b	-0.11	-1.69	-0.44	1.42	3.58	17.8	1.00	0.95	2130	9.1	204	4.5	5
LTT 3780 b	-0.15	-1.30	-0.38	1.32	2.46	15.2	0.90	0.38	902	8.2	1022	13.1	18
GJ 1132 b*	-0.15	-1.03	-0.27	1.19	1.84	13.9	0.98	0.19	583	8.3	2441	9.7	30
TOI-6086 b	-0.15	-1.05	-0.30	1.18	1.81 [†]	13.9 [†]	1 [†]	0.25	633	10.0	1745	4.2	11 [†]
Kepler-446 b	-0.17	-1.01	-0.41	1.15	1.64 [†]	13.4 [†]	1 [†]	0.19	558	12.8	2316	0.9	4 [†]
TOI-1685 b*	-0.19	-1.42	-0.47	1.47	3.03	16.1	0.79	0.45	1090	8.8	873	11.9	12
TOI-431 b	-0.19	-1.67	-0.40	1.28	3.07	17.3	1.20	0.78	1862	6.7	258	15.6	16
TOI-1860 b	-0.19	-1.39	-0.24	1.31	2.66 [†]	16.0 [†]	1 [†]	0.99	1885	6.8	163	8.0	12 [†]
TRAPPIST-1 b*	-0.23	-1.04	-0.72	1.12	1.37	12.4	0.94	0.09	397	10.3	7367	3.8	29
Wolf 327 b	-0.27	-1.52	-0.53	1.24	2.53	16.0	1.13	0.41	1087	8.4	784	12.5	13
LP 791-18 b	-0.28	-1.28	-0.33	1.21	2.00 [†]	14.4 [†]	1 [†]	0.14	616	10.6	3727	6.8	15 [†]
TOI-5720 b	-0.33	-1.17	-0.86	1.09	1.36 [†]	12.5 [†]	1 [†]	0.38	706	9.3	681	2.9	8 [†]
LHS 3844 b*	-0.34	-1.54	-0.62	1.30	2.61 [†]	15.8 [†]	1 [†]	0.15	804	9.2	3995	28.9	35 [†]
GJ 3473 b	-0.35	-1.21	-0.56	1.26	1.86	13.6	0.83	0.36	772	8.8	1014	6.7	14
LHS 1678 c	-0.36	-0.96	-1.20	0.94	0.81 [†]	10.4 [†]	1 [†]	0.34	533	8.3	688	1.9	15 [†]
TOI-1450 A b	-0.36	-1.11	-1.07	1.13	1.26	11.8	0.84	0.48	722	7.6	460	4.4	14
LP 791-18 d	-0.48	-1.10	-1.29	1.03	0.90	10.4	0.83	0.14	432	10.6	2702	1.4	15
LHS 475 b	-0.54	-1.21	-1.37	0.97	0.92 [†]	10.9 [†]	1 [†]	0.27	594	7.7	977	5.4	27 [†]
TRAPPIST-1 d	-0.56	-1.14	-1.61	0.79	0.39	7.8	0.90	0.09	286	10.3	3673	0.3	26
TOI-544 b	-0.61	-1.46	-0.78	2.02	2.89	13.4	0.29	0.63	999	7.8	882	12.9	176
GJ 806 b	-0.66	-1.54	-0.90	1.33	1.90	13.4	0.72	0.41	939	6.5	867	23.9	44
TOI-178 b	-0.68	-1.46	-0.99	1.15	1.50	12.8	0.92	0.65	1040	8.7	263	2.7	6
TOI-6008 b	-0.84	-1.50	-1.46	1.03	1.11 [†]	11.6 [†]	1 [†]	0.23	706	9.5	1523	6.4	19 [†]
TOI-1807 b	-0.86	-1.81	-0.69	1.50	2.44	14.3	0.62	0.80	1694	7.6	338	11.8	19
TOI-1442 b	-0.99	-1.88	-1.19	1.17	1.76 [†]	13.7 [†]	1 [†]	0.29	1072	10.1	1197	9.4	13 [†]
TOI-540 b	-1.09	-1.69	-1.95	0.90	0.70 [†]	9.9 [†]	1 [†]	0.16	611	8.9	1909	6.8	38 [†]
SPECULOOS-3 b	-1.10	-1.81	-1.95	0.98	0.93 [†]	10.9 [†]	1 [†]	0.10	552	10.5	5303	7.7	35 [†]
L 98-59 b	-1.10	-1.61	-2.05	0.85	0.47	8.3	0.84	0.31	620	7.1	624	5.0	41
GJ 1252 b*	-1.24	-2.00	-1.93	1.19	1.32	11.8	0.74	0.38	1086	7.9	782	16.3	32
TOI-500 b	-1.26	-2.03	-1.69	1.17	1.42	12.3	0.85	0.74	1615	7.7	249	8.5	16
TOI-561 b	-1.45	-2.36	-1.55	1.40	2.02	13.5	0.66	0.81	2303	8.4	231	7.9	14
K2-183 b	-1.52	-2.27	-1.79	1.10	1.41 [†]	12.6 [†]	1 [†]	0.94	2452	11.0	134	1.5	3 [†]
GJ 367 b*	-1.75	-2.38	-2.60	0.70	0.63	10.6	1.96	0.46	1364	5.8	196	16.4	31
TOI-4527.01	-1.82	-2.43	-2.79	0.91	0.72 [†]	10.0 [†]	1 [†]	0.48	1359	7.0	294	12.9	31 [†]
GJ 238 b	-1.85	-2.35	-2.75	0.57	0.14 [†]	5.6 [†]	1 [†]	0.42	758	7.0	145	2.0	26
LHS 1678 b	-1.87	-2.39	-2.82	0.69	0.27 [†]	7.1 [†]	1 [†]	0.34	866	8.3	364	3.9	28 [†]

¹⁰ the density scaled to that of a planet with Earth-like composition¹¹ Emission spectroscopy metric from [Kempton et al. \(2018\)](#)¹² Transmission spectroscopy metric from [Kempton et al. \(2018\)](#)

K2-223 b	-1.87	-2.43	-2.72	0.89	0.67 [†]	9.7 [†]	1 [†]	1.06	2271	9.8	67	1.0	4 [†]
K2-157 b	-1.91	-2.53	-2.59	1.00	1.01 [†]	11.2 [†]	1 [†]	0.94	2601	11.0	109	1.3	3 [†]
K2-137 b	-3.11	-3.60	-4.04	0.64	0.22 [†]	6.5 [†]	1 [†]	0.46	1471	10.9	409	3.5	18 [†]

Table B1. Planets located below the cosmic shorelines for $f_{\text{initial}} = 10^{-4}$ are marked with an asterisk (*). The scores for each atmospheric composition represent the difference in the base-10 logarithm of instellation between the planet and the cosmic shorelines for a 1 wt% volatile mass fraction at a given planetary mass. More negative values are more atmosphere-favorable. [†]These planets lack a measured mass value and we assume an Earth-like composition for these calculations. *These planets have been suggested to have no thick atmosphere based on thermal emission observations (Xue et al. 2024; Luque et al. 2024; Greene et al. 2023; Kreidberg et al. 2019; Crossfield et al. 2022; Zhang et al. 2024). We do not take the individual constrained stellar age into account, and the score is obtained by assuming an stellar age distribution from Berger et al. (2020).

	Assumptions	
CO ₂ (Thermal)	Tian et al. (2009), Tian (2009)	a. Neutral & Ion species included b. Jeans escape (hydrodynamic thermosphere) c. Heating: Collisions, chemical reactions, photoelectrons, radiative line heating d. Cooling: Recombination, molecular, Ly- α , and atomic oxygen 63 μ m emission 1. Stellar bolometric luminosity: Baraffe et al. (2015) (no uncertainties included) 2. X-ray flux: Jackson et al. (2012) or Selsis et al. (2007) 3. EUV-to-X-ray ratio and uncertainties: King & Wheatley (2020) 4. Loss rate obtained using three different interpolation approaches (see Fig. C4)
CO ₂ (Non-Thermal)	Chin et al. (2024)	a. 3D Block-Adaptive-Tree Solar Wind Roe-type Upwind Scheme (BATS-R-US) b. Multispecies magnetohydrodynamic (MS-MHD) model c. Ion species: H ⁺ , O ⁺ , O ₂ ⁺ , CO ₂ ⁺ and ionospheric photochemistry d. Unmagnetized planets assumed 1. Stellar bolometric luminosity: Baraffe et al. (2015) (no uncertainties included) 2. X-ray flux: Jackson et al. (2012) or Selsis et al. (2007) 3. Stellar mass loss rate scaled to X-ray: Wood et al. (2021) (no uncertainties included) 4. Loss rate scaled to orbital distance and stellar mass loss rate: Dong et al. (2018) (no uncertainties included)
H ₂ O (Thermal)	Johnstone (2020)	a. Neutral & Ion species included b. Transonic hydrodynamic c. Heating: Collisions, ~500 chemical reactions, photoelectrons, radiative line heating d. Cooling: Recombination, molecular, Ly- α , and atomic oxygen 63 μ m emission 1. Stellar bolometric luminosity: Baraffe et al. (2015) (no uncertainties included) 2. X-ray flux: Jackson et al. (2012) or Selsis et al. (2007) 3. EUV-to-X-ray ratio and uncertainties: King & Wheatley (2020)
N ₂ /O ₂ (N22) (Thermal)	Nakayama et al. (2022)	a. Neutral & Ion species included b. Jeans escape (hydrodynamic thermosphere) c. Heating: Collisions, ~500 chemical reactions, photoelectrons, radiative line heating d. Cooling: Recombination, molecular, atomic line cooling of N, C, and O 1. Stellar bolometric luminosity: Baraffe et al. (2015) (no uncertainties included) 2. X-ray flux: Jackson et al. (2012) or Selsis et al. (2007) 3. EUV-to-X-ray ratio and uncertainties: King & Wheatley (2020)
N ₂ /O ₂ (C24) (Thermal)	Chatterjee & Pierrehumbert (2024)	a. Neutral & Ion species + Ambipolar motion b. Analytic approximations to transonic hydrodynamic and hydrostatic escape b. Heating: Parameterized c. Cooling: Recombination, atomic line cooling of N and O d. Introduces a new regime of global ion outflow controlled by a collisional-radiative thermostat 1. Stellar bolometric luminosity: Baraffe et al. (2015) (no uncertainties included) 2. X-ray flux: Jackson et al. (2012) or Selsis et al. (2007) 3. EUV-to-X-ray ratio and uncertainties: King & Wheatley (2020) 4. Includes uncertainty in the energy-limited loss regime (see Table 1)
CH ₄	Energy-Limited Estimate	a. All uncertainties included in escape efficiency factor ϵ ($0.05 < \epsilon < 0.5$) 1. Stellar bolometric luminosity: Baraffe et al. (2015) (no uncertainties included) 2. X-ray flux: Jackson et al. (2012) or Selsis et al. (2007) 3. EUV-to-X-ray ratio and uncertainties: King & Wheatley (2020)

Table B1. Summary of model components for different atmospheric compositions. This includes key assumptions regarding species considered, heating and cooling mechanisms, and stellar input parameters.

C. APPENDIX FIGURES

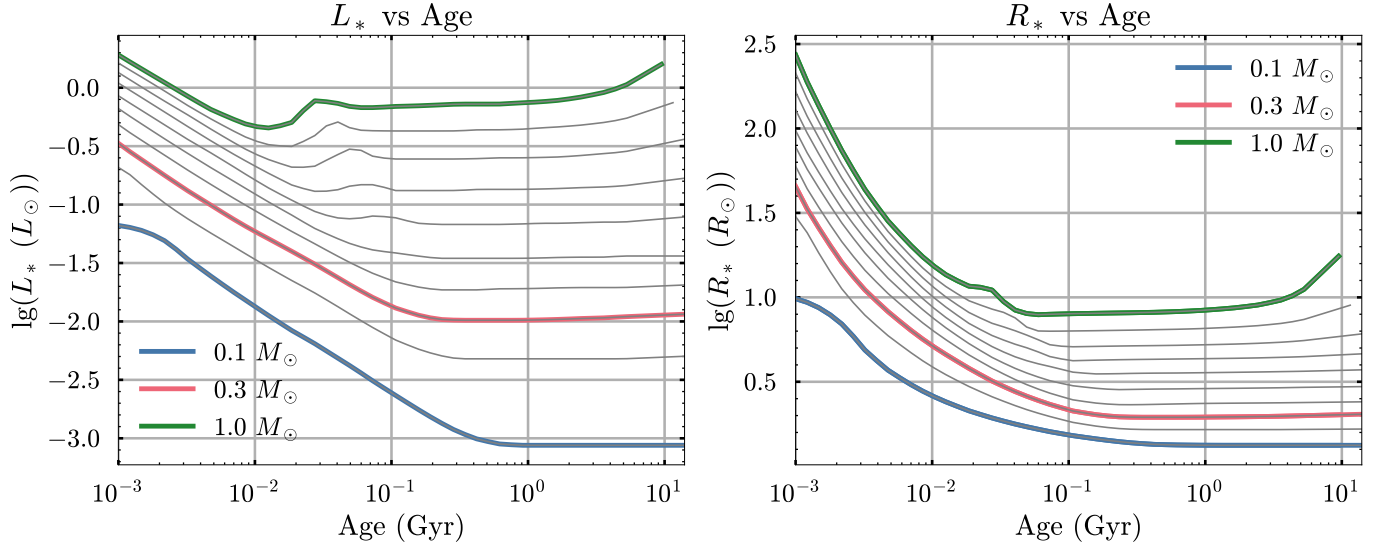


Figure C1. Stellar luminosity (L_{bol}) normalized to the Sun's luminosity at the present-day (L_\odot), and stellar radius (R_*) normalized to the Sun's radius (R_\odot) versus time from the model of Baraffe et al. (2015) for star masses ranging from $0.1 - 1.0 M_\odot$.

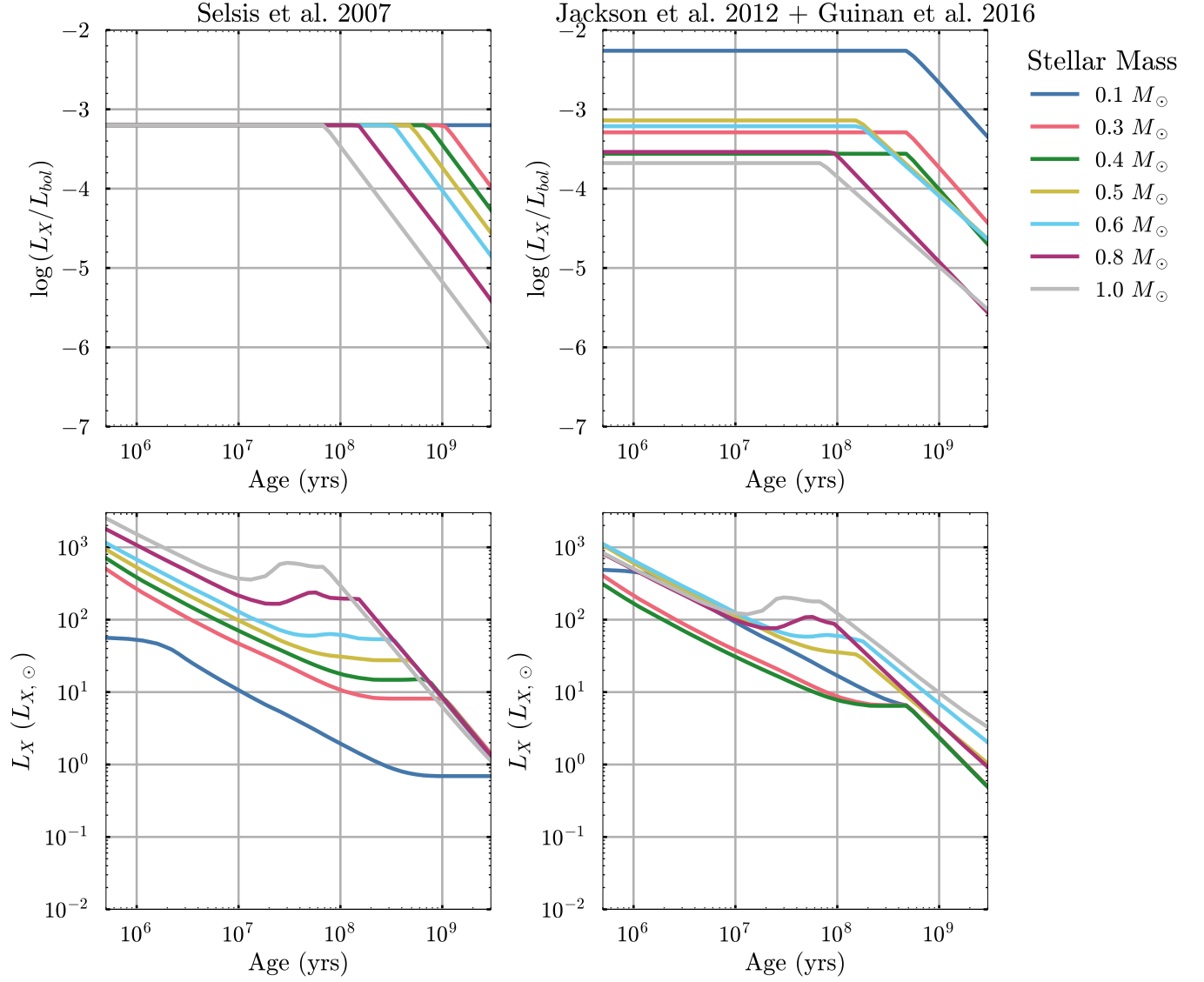


Figure C2. Upper panels: The ratio of X-ray luminosity to bolometric luminosity evolves over time for stellar masses from $0.1 M_\odot$ to $1 M_\odot$. The left panel presents the parameterization from (Selsis et al. 2007), while the right panel shows the results obtained by combining data from (Jackson et al. 2012) and (Guinan et al. 2016). Lower panels: The X-ray luminosity scaled to solar X-ray flux evolves over time. In the lower right panel, the lines for $M_* < 0.5 M_\odot$ overlap because Guinan et al. (2016) presents a unified X-ray evolution for M0–M5 stars after saturation phase. Note that $L_{X,\odot}/L_{bol,\odot} = 10^{-6.1}$.

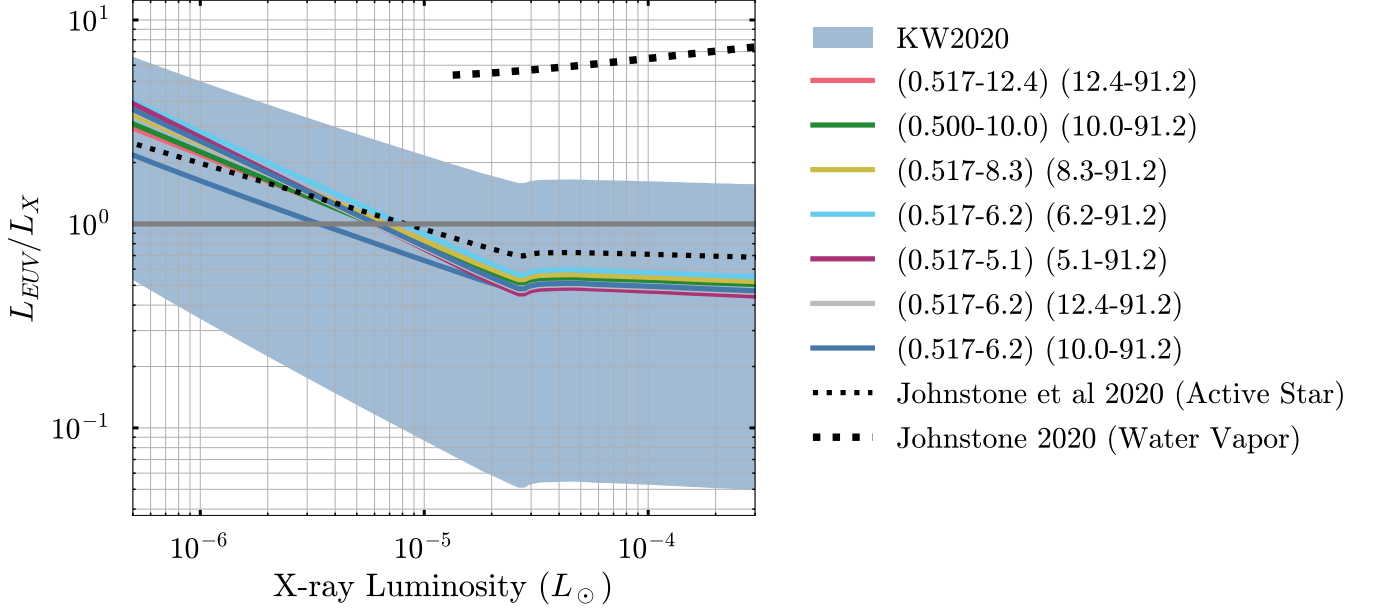


Figure C3. The ratio of EUV luminosity to X-ray luminosity is shown as a function of X-ray flux at Stellar surface. The X-ray flux is calculated for a 0.5 solar-mass star evolving from 1 Myr to 1 Gyr. The blue line and shaded region represent the results from King & Wheatley (2020) including uncertainties. Additional colorful lines, labeled with wavelength ranges in Å, are obtained from Table 4 of King et al. (2018), where the left bracket indicates the X-ray range and the right bracket indicates the EUV range. The dotted black line is derived from Johnstone et al. (2021).

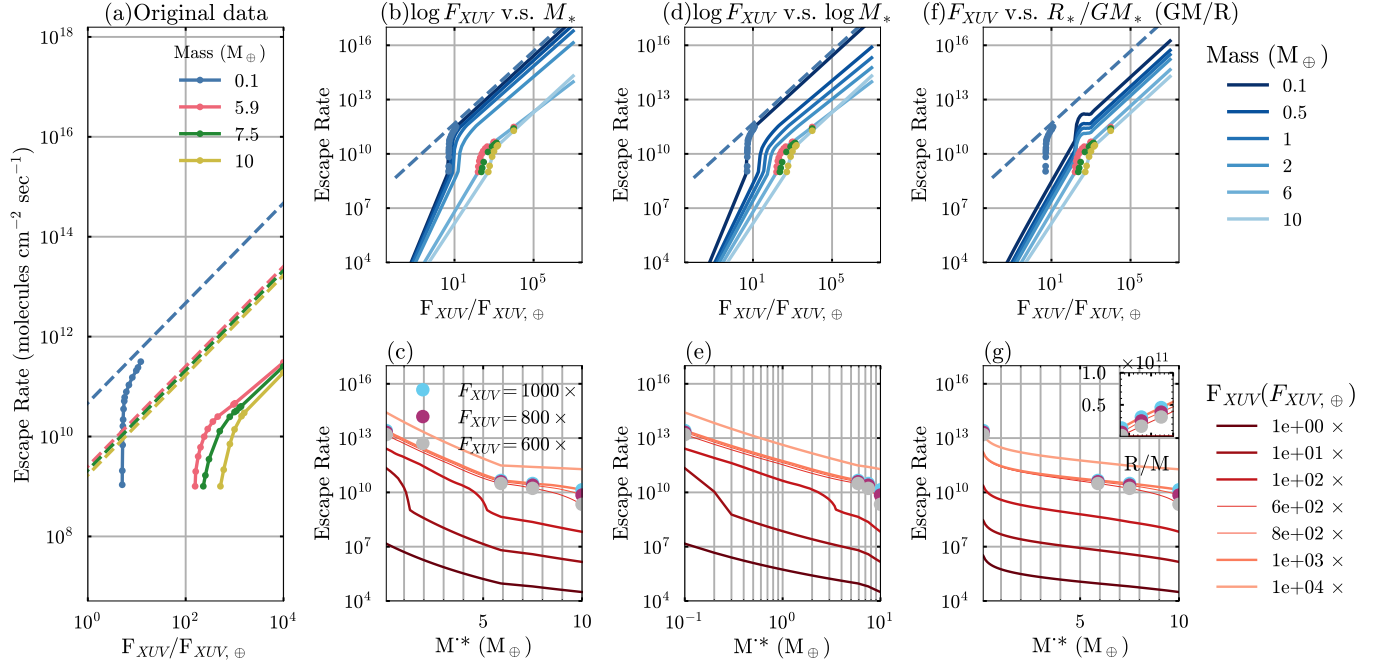


Figure C4. CO₂ escape rates are sensitive to interpolation approaches. Leftmost panel: Atmospheric escape rate as a function of XUV flux, scaled to Earth's present-day value. The dots and connected lines represent output from Tian (2009) and Tian et al. (2009). The rightmost points for super-Earths are extrapolated by Tian (2009). The dashed line shows the energy-limited escape rate assuming an efficiency of 0.1. We interpolate their model output and our results for near-Earth-sized planets are sensitive to the interpolate approach used. (b)-(g) show this sensitivity. In (b)&(c), we interpolate $\log F_{XUV}$ with planetary mass M_p . (d)&(e) interpolates $\log F_{XUV}$ with the logarithm of planetary mass ($\log M_p$). (f)&(g) excludes Mars data and assumes the escape rate scales with gravitational potential energy (GM_p/R_p), interpolating between F_{XUV} and $R_p/(GM_p)$. The upper panels illustrate how the escape rate varies with XUV flux for different planetary masses, while the lower panels show how the escape rate changes with planetary mass for various XUV flux levels. The dots represent benchmark output obtained from the leftmost panel, which are used for interpolation. Overall, the linear-planetary-mass provides higher escape rate estimates for near-Earth-sized planets compared to the other methods.

Carbon loss rates for planets with CO₂-dominated atmospheres orbiting a Solar-like star at $t = 100$ Myr

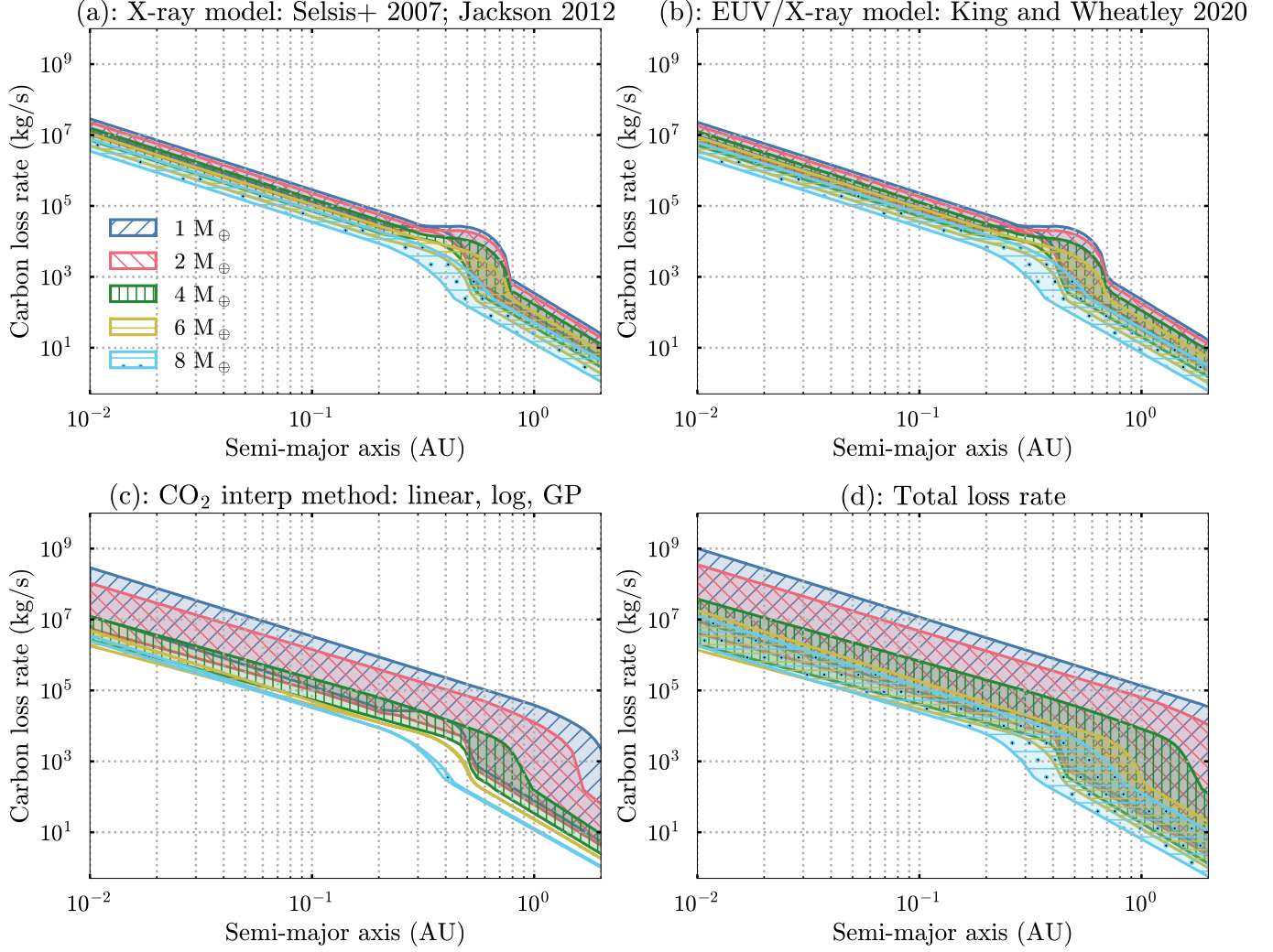


Figure C5. Carbon loss rate as a function of semi-major axis for planets with CO₂-dominated atmospheres orbiting a Solar-like star at $t = 1$ Myr. The shaded region represents the range between the maximum and minimum values under certain assumptions. The uncertainties are broken down as follows: (a): Using the center values of γ for EUV extrapolation and a interpolation of CO₂ escape rates to M_p (linear), the uncertainty comes solely from the choice of X-ray model. (b): Adopting the J12+G16 X-ray model and linear escape rate interpolation, the uncertainty arises only from the EUV extrapolation. (c): Using the J12+G16 X-ray model and center EUV extrapolation values, the uncertainty stems only from escape rate interpolation. (d): Incorporating all uncertainties. The uncertainties from the X-ray model and EUV extrapolation are of the same order of magnitude. The uncertainty from the interpolation method of CO₂ escape rates is more significant for near-Earth-sized planets but negligible for super-Earths. The total uncertainty results in the loss rates for an 8 Earth-radius planet overlapping with those of a 1 Earth-radius planet.

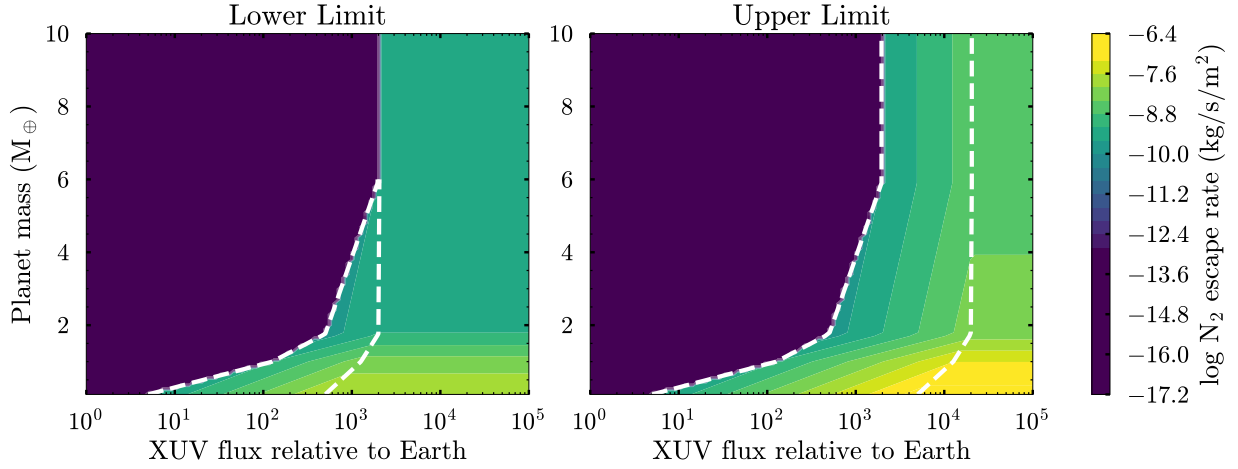
N₂ Escape Rate: CP2024 Model

Figure C6. The loss rate per surface area for an N₂/O₂ atmosphere is shown as a function of XUV flux and planetary mass, interpolated/extrapolated from [Chatterjee & Pierrehumbert \(2024\)](#). The dark purple region indicates where hydrostatic escape occurs, with the escape rate fixed at 10^{-13} kg/s/m². The white dashed lines show bounds to the energy-limited regime.

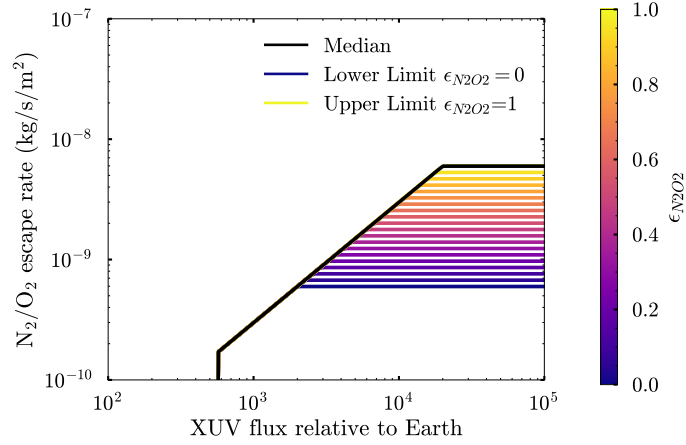


Figure C7. The N₂/O₂ loss rate as a function of XUV flux. In our Monte Carlo simulations, we randomly sample the $\epsilon_{N_2O_2}$ from a uniform distribution between 0 and 1. The variations in escape rates resulting from this sampling are illustrated by the colorful lines.

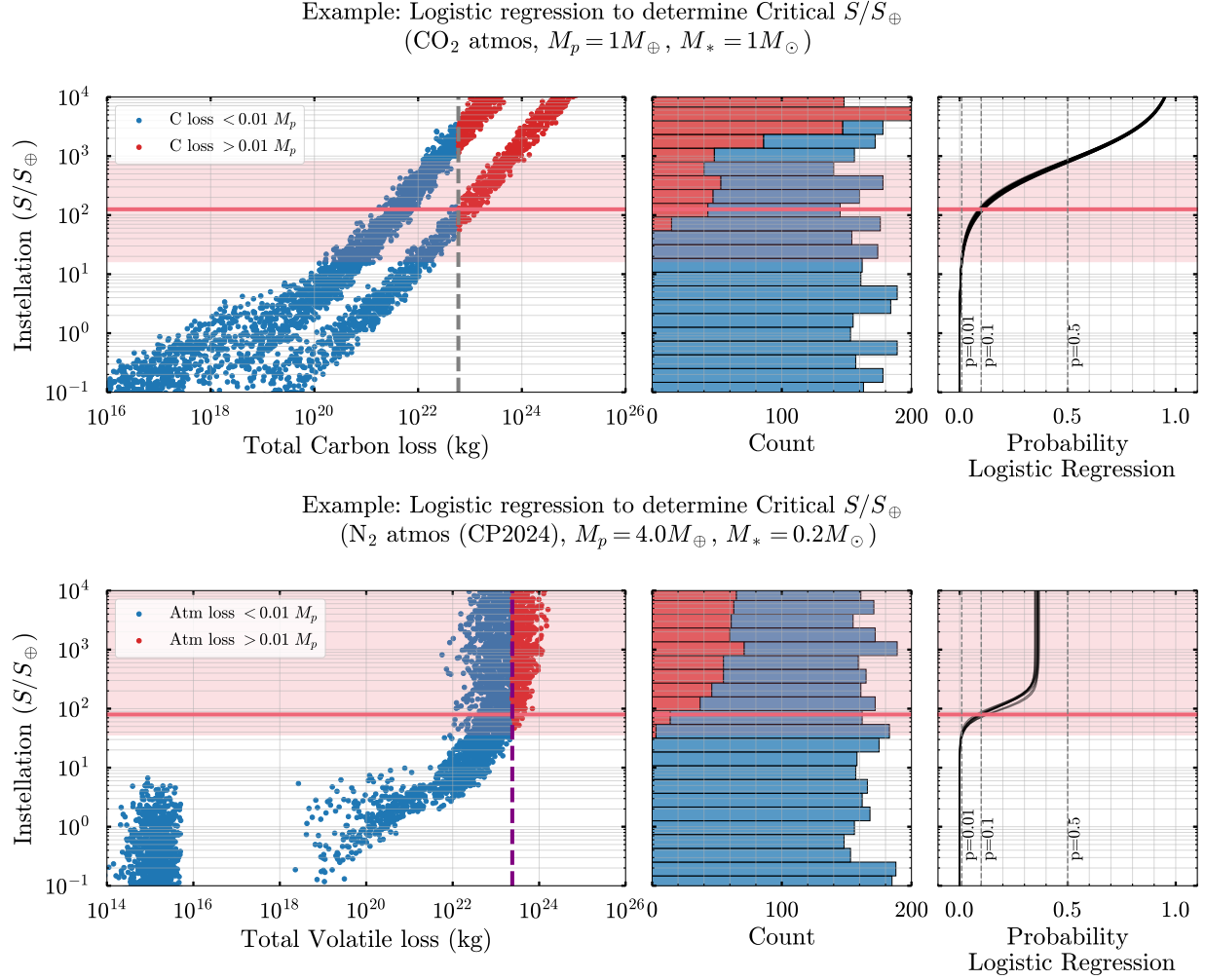


Figure C8. Example Monte Carlo simulation results for an Earth-mass planet with a CO_2 atmosphere orbiting a $1M_{\odot}$ star (Upper) and a 4 Earth-mass planet with a N_2 -dominated atmosphere orbiting a $0.2M_{\odot}$ star (Lower). Left: Bolometric instellation, scaled to earth's value (S/S_{\oplus}), plotted against the total carbon mass lost. Blue dots indicate Monte Carlo outcomes in which the planet retains its atmosphere (with a initial carbon mass of $0.01M_{\oplus}$), while orange dots indicate outcomes in which the atmosphere is stripped. The middle green line marks the critical instellation at $p_0 = 0.9$, meaning there is a 50% probability of atmospheric retention at that flux level. The shaded region spans from $p_0 = 0.99$ (lower boundary) to $p_0 = 0.5$ (upper boundary), illustrating instellation thresholds for 99% and 50% retention probability, respectively. To obtain a robust estimate of the critical instellation S^* at a given p_0 , we draw 5,000-point bootstrap samples from our 10,000-point Monte Carlo dataset (in 10 iterations), refit the logistic model each time, and then average the resulting S^* values. Right: Histograms of the instellation values for planets that retain atmosphere (blue) versus those that lose it (orange). For our implementation of the CP2024 N_2 -escape, in the volatile rich limit the probability of atmospheric loss does not reach one due to the plateau in escape rates for the highest XUV fluxes. To capture this behavior, we apply a three-parameter logistic fitting. In contrast, for CO_2 and other atmospheres where the escape rate continues to increase with XUV flux, the loss probability approaches one at infinite high XUV flux, so it is reduced to a 2 parameters fitting.

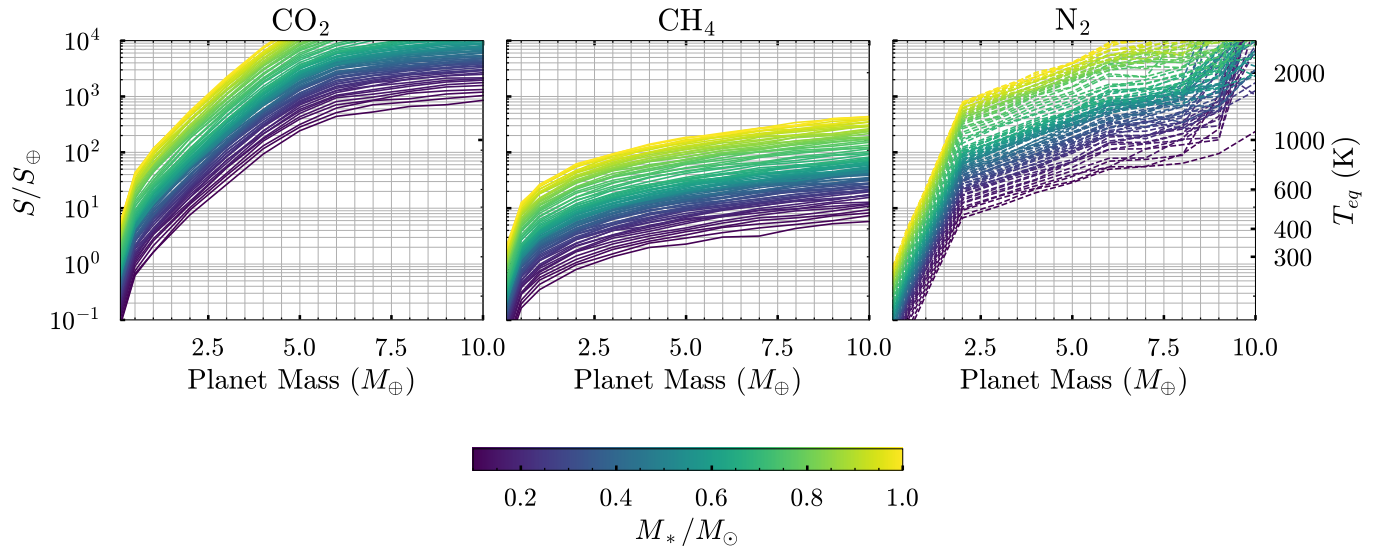


Figure C9. Cosmic shorelines as functions of planetary mass and instellation scaled to Earth's value (S/S_\oplus). Each line corresponds to results computed for stellar masses within a range of $0.01 M_\odot$. For example, the lowest (darkest) line represents stellar masses between 0.10 and $0.11 M_\odot$. The priority scores listed in Table 3 and Table B1 are derived from these shoreline calculations.

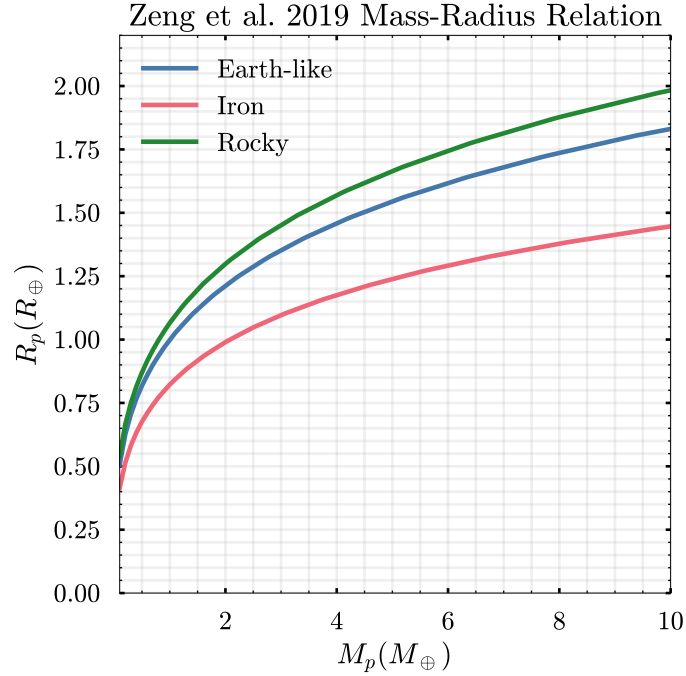


Figure C10. The mass-radius relationship for different planetary compositions: pure iron (100% Fe), Earth-like rocky (32.5% Fe + 67.5% MgSiO_3), and pure rock (100% MgSiO_3).

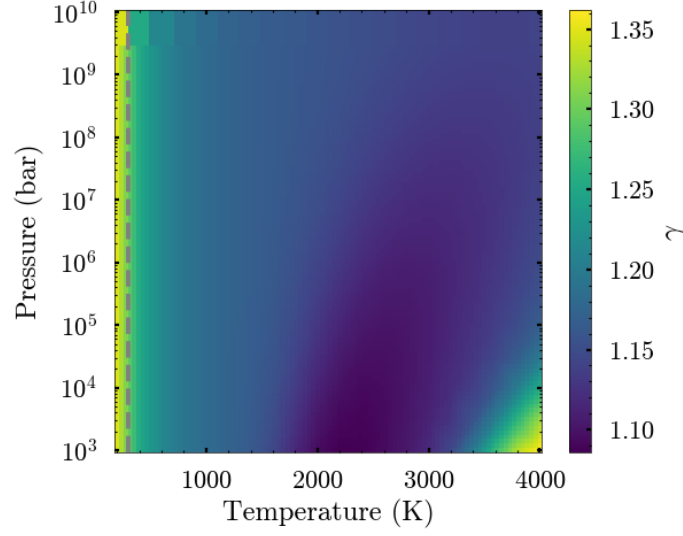


Figure C11. The heat capacity ratio (γ) for CO_2 as a function of temperature and pressure, obtained using NASA's Chemical Equilibrium with Applications (CEA) code (<https://cearun.grc.nasa.gov/>) (Gordon & McBride 1994), considering ionized species as possible products.

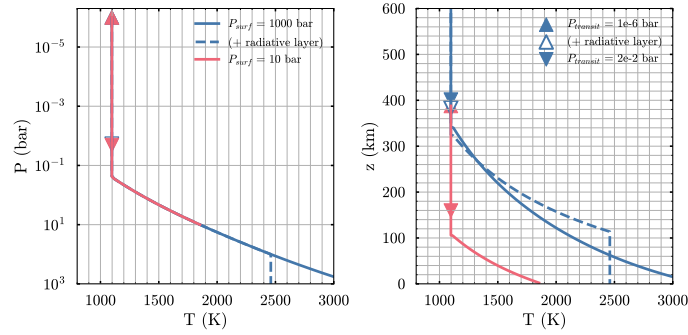


Figure C12. Left Panel: Temperature-Pressure profiles for atmospheres with surface pressures of 10 bar (pink) and 100 bar (blue). The solid lines correspond to the two-layer model (Scenario (a) in Fig. 5), where the atmosphere consists of a convective lower layer and an isothermal upper layer beyond the radiative-convective boundary (RCB). The dashed lines represent the three-layer model (Scenario (b) in Fig. 5), where an additional radiative layer forms near the surface. Right Panel: Altitude-temperature profiles for the same cases shown in the left panel. Triangular markers indicate the pressure level probed by the transit method, with filled symbols representing the two-layer model (Scenario (a)) and open symbols representing the three-layer model (Scenario (b)).

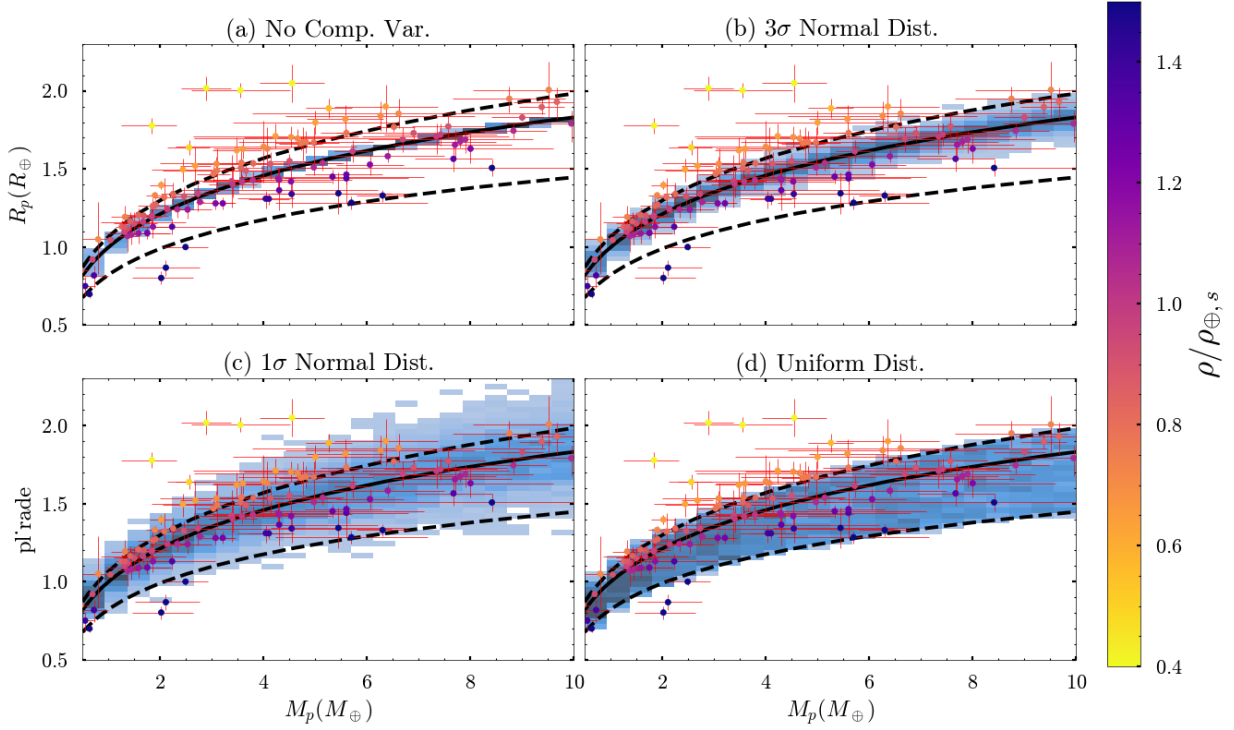


Figure C13. Mass-Radius Relationship for Solid-Body Planets Under Three Composition Assumptions: Given a planetary mass (M_p), the radius is assigned based on different composition assumptions: (a) a fixed Earth-like composition ($R_{\text{earth-like}}(M_p)$), (b) a normal distribution centered at $R_{\text{earth-like}}(M_p)$ with a standard deviation equal to one-third of the difference between $R_{\text{earth-like}}(M_p)$ and $R_{\text{silicate}}(M_p)$, (c) a normal distribution centered at $R_{\text{earth-like}}(M_p)$ with a standard deviation equal to the difference between $R_{\text{earth-like}}(M_p)$ and $R_{\text{silicate}}(M_p)$, and (d) a uniform distribution spanning the range between $R_{\text{silicate}}(M_p)$ (pure MgSiO_3) and $R_{\text{iron}}(M_p)$ (pure Fe). The shaded blue region represents a 2D histogram of our Monte Carlo samples, with darker colors indicating higher number density. The dots are observed rocky planet candidates from the NASA Exoplanet Archive, with error bars representing measurement uncertainties. The colors represent the measured density relative to Earth's composition.

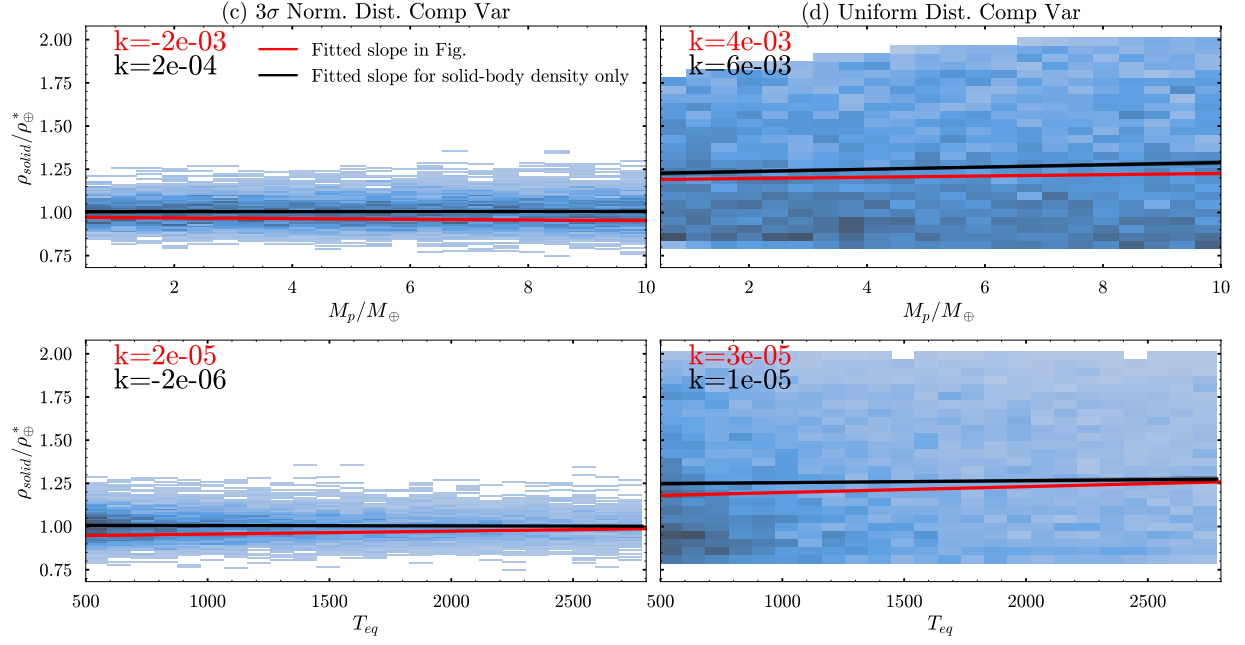


Figure C14. Trend of the Scaled Density of the Solid Body Only: The upper row shows 2D histograms of the scaled density of the solid body ($\rho_{solid}/\rho_{\oplus}^*$) as a function of planetary mass (M_p), while the lower row shows its relationship with equilibrium temperature (T_{eq}). The left column (c) assumes that solid density variations follow a normal distribution, with a standard deviation equal to 1/3 of the difference between $R_{\text{earth-like}}(M_p)$ and $R_{\text{silicate}}(M_p)$. The right column (d) corresponds to a uniform distribution spanning the range between $R_{\text{silicate}}(M_p)$ (pure MgSiO_3) and $R_{\text{iron}}(M_p)$ (pure Fe). The black lines and black text indicate the results of linear regression for the solid-body scaled density, while the red ones represent the linear regression of the total density derived from the transit radius (see Fig. 7). In (c), the slope of the solid-body density trend is an order of magnitude lower than that of the final total density, suggesting an insignificant contribution from variations in the solid composition. However, in (d), the solid-body density trend significantly influences the overall density slope, even changes the sign for slope of $\rho_{solid}/\rho_{\oplus}^* - M_p$. We also tested uniformly sampling density instead of radius, but the trend caused by the solid portion alone persists.